Volume II

Pore-Scale Controls on Permeability, Fluid Flow, and Methane Hydrate Distribution in Fine-Grained Sediments

by

Hugh Callahan Daigle

5. Effects of multiphase methane supply on hydrate accumulation and fracture generation[1]

5.1. Introduction

Significant fracture-hosted methane hydrates have been encountered at Keathley Canyon Block 151 in the northern Gulf of Mexico (Cook et al., 2008), at Hydrate Ridge offshore Oregon (Tréhu et al., 2006b), and in the Krishna-Godavari Basin offshore India (Collett et al., 2007). In Chapter 4 we showed that hydraulic fractures can form in marine hydrate systems with sufficiently rapid methane supply and low initial sediment permeability; if methane supply is too slow or permeability too high relative to water flux, fracture-hosted hydrates, if present, most likely formed by hydrate heave or in preexisting fractures. The model assumes a constant flux of methane-charged water. However, flux in hydrate systems is often variable (e.g., Tryon et al., 2002), and field evidence indicates that methane may exist in some cases as free gas within the regional methane hydrate stability zone (RHSZ) (e.g., Wood and Ruppel, 2000; Tréhu et al., 2004). We adapt the model of Chapter 4 to investigate how variable flux and multiphase flow affect hydrate saturation and fracture generation.

The RHSZ is the depth interval in which structure I methane hydrate is stable at seawater salinity (3.35% NaCl by mass) and hydrostatic pressure. Free gas may occur within the RHSZ if three-phase equilibrium conditions are met. Two processes that may allow this are increased fluid pressure driven by gas buoyancy (e.g., Flemings et al.,

2003) and triple point temperature depression caused by excess porewater salinity (Zatsepina and Buffett, 1998). We consider the latter case as excess salinity appears to be associated with gas occurrence in the RHSZ at Hydrate Ridge (Liu and Flemings, 2006) and in the Mackenzie Delta (Wright et al., 2005).

We modify the model from Chapter 4 to include multiphase flow with a constant basal pressure. This boundary condition reflects a large source reservoir analogous to a water-drive hydrocarbon system and is a more reasonable assumption than constant flux for many settings. We apply this model to Hydrate Ridge, a system with no water-phase overpressure (Dugan, 2003) and Blake Ridge, a system with water-phase overpressure of several MPa (Flemings et al., 2003). Our results illustrate how the phase of methane supplied to the RHSZ affects hydrate and fracture distribution.

5.2. Hydrate Formation and Fracture Generation

We simulate 1-D, multiphase flow with fixed geothermal gradient (dT/dz [K m^{-1}]), seafloor depth (d_{sf} [m]) and seafloor temperature (T_{sf} [m]). We solve mass balances for methane, salt, and water. Hydrate forms when the methane concentration exceeds the local solubility. We compute solubility using the method of Bhatnagar et al. (2007) and update for changes in salinity using the method of Duan et al. (1992). Fluxes are computed from Darcy's law. Water viscosity is assumed constant, and gas viscosity is computed from the Lennard-Jones potential (Bird et al., 2007). Relative permeabilities are calculated using Corey's model (Bear, 1972) assuming residual water and gas saturations of 10% and 2%, respectively (e.g., Liu and Flemings, 2007). As hydrate

forms, we reduce permeability by assuming that hydrate forms a uniform coating on the pore walls (e.g., Kleinberg et al., 2003b).

The pressures of the water and gas phases (P_w, P_g [Pa]) are linked by the capillary pressure P_c [Pa] such that $P_g = P_w + P_c$. P_c is computed as

$$P_c = J\sigma_{gw}\sqrt{\frac{\varphi}{k(1 - S_h)}}$$

(Equation 5.1)

where φ is porosity [m^3 m^{-3}], k is permeability [m^2], S_h is hydrate saturation [m^3 m^{-3}], σ_{gw} is the gas-water interfacial tension (0.072 J m^{-1}; Henry et al., 1999) and J is a dimensionless function that describes changes in P_c as gas displaces water (Bear, 1972; Liu and Flemings, 2007). Equation 5.1 assumes that hydrate forms a uniform coating on grains. Initial conditions are zero methane concentration and salt concentration equal to seawater everywhere. Dissolved methane concentration at the base of the domain (twice the thickness of the RHSZ) is set equal to the solubility at the base of the RHSZ (BRHSZ). At the base of the domain, we specify a constant water-phase overpressure (pressure in excess of hydrostatic) P_w^* and compute P_g from Equation 5.1.

Hydraulic fractures form when the total excess pore pressure exceeds the vertical hydrostatic effective stress (σ_{vh}' [Pa]). We define the normalized overpressure as $\lambda_T^* = P_T^*/\sigma_{vh}'$, where P_T^* is the sum of the water- and gas-phase overpressures, and assume fractures form when $\lambda_T^* = 1$. We stop the simulation once fractures form. We assume that the sediment has no tensile strength or cohesion, and that hydrate does not affect sediment strength or local stress conditions. Since fine-grained marine sediments typically have small cohesion and tensile strength (Behrmann, 1991) and hydrate tends to

increase sediment strength (e.g., Yun et al., 2007), the true time to fracture may be somewhat longer than we predict since P_T^* will have to overcome additional sediment strength. For shallow hydrate systems with low S_h, we expect these effects to be negligible.

5.3. Results

Our model for Hydrate Ridge assumes $d_{sf} = 800$ m, $T_{sf} = 277$ K, $dT/dz = 0.053$ K m^{-1} (Tréhu, 2006). φ and k are based on bulk density logs and laboratory measurements of permeability (Lee and Collett, 2006; Tan et al., 2006). We compute P_c using the J-function of Liu and Flemings [2007], and assume $P_w^* = 0$ (Dugan, 2003). The salinity at the BRHSZ increases to the triple point after 250 years; after this, free gas migrates upwards into the RHSZ. After 1.9×10^3 years, enough hydrate forms at 38 mbsf ($S_h = 0.85$) to increase P_T^* to the point where fractures form (Figure 5.1). Since more salt is required to reach the triple point as temperature and pressure decrease, S_h increases upwards within the RHSZ. This is consistent with trends of S_h inferred from porewater chlorinity (Shipboard Scientific Party, 2003) and acoustic logs (Lee and Collett, 2006) showing S_h increasing from ~0 near the BRHSZ (~140 mbsf) to ~0.15 at 60–80 mbsf at Sites 1244, 1245, and 1250. Our computed S_h are much larger than this. This may be due in part to our J-function, which defines the P_c response as gas enters the pore space; the true P_c response for these sediments is unconstrained. The hydrate growth habit exerts additional control on permeability reduction and S_h. Pore-filling hydrate reduces permeability more rapidly than pore-coating hydrate (Liu and Flemings, 2007), allowing fractures to form at shorter time and lower S_h. Assuming pore-filling hydrate at Hydrate
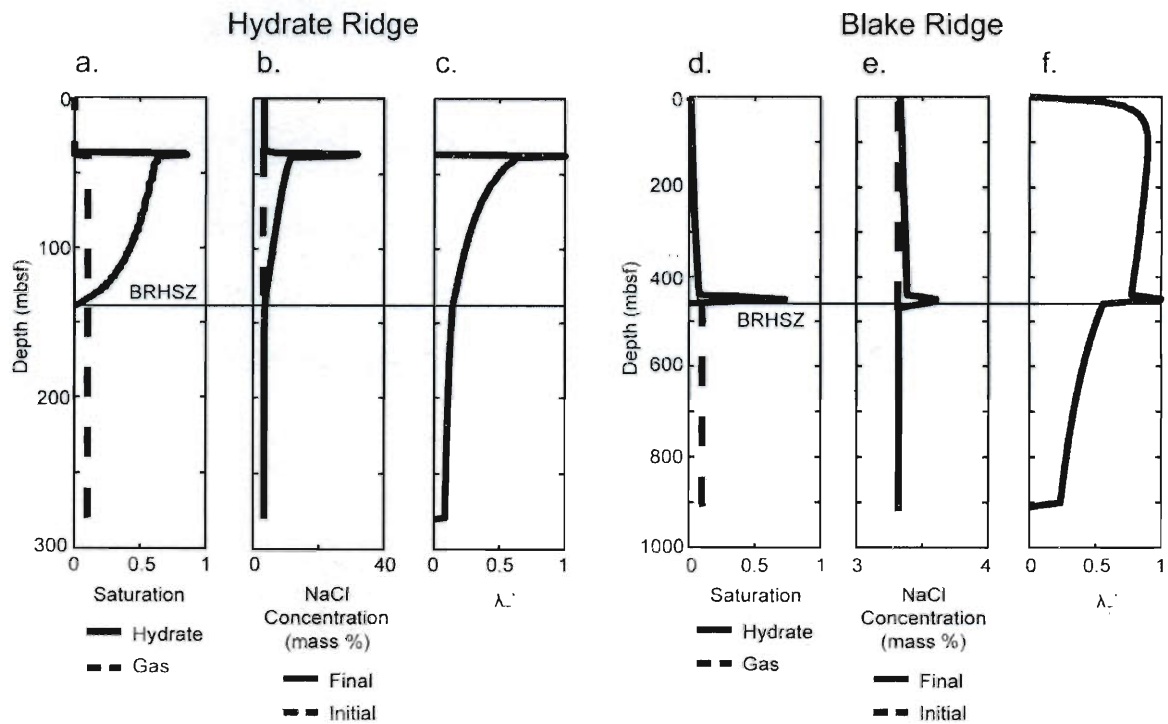
Figure 5.1 Model results. Entire model domain (twice RHSZ thickness) is plotted. (a) S_h and S_g at Hydrate Ridge after 1.9×10^3 years. Gas has migrated ~100 m upwards through the RHSZ. S_h increases upwards since salinity must be higher shallower in the RHSZ to reach three-phase equilibrium. (b) Salinity at Hydrate Ridge. Salinity has increased to ~30% at 38 mbsf. (c) λ_T^* at Hydrate Ridge. Values increase upwards to 38 mbsf, where fractures initiate. (d) S_h and S_g at Blake Ridge after 1.6×10^4 years. Gas is unable to move into the RHSZ because excess salt is removed by water flux. Hydrate forms most rapidly at the BRHSZ where the dissolved methane concentration gradient is greatest. (e) Salinity at Blake Ridge. Salinity increases slightly near the BRHSZ due to methane formation. Most salt is flushed upwards in the water flux. (f) λ_T^* at Blake Ridge. Fractures initiate at the BRHSZ where the most hydrate has accumulated. $\lambda_T^* \approx 0.6$ just below the BRHSZ, indicating elevated gas pressure at this point.
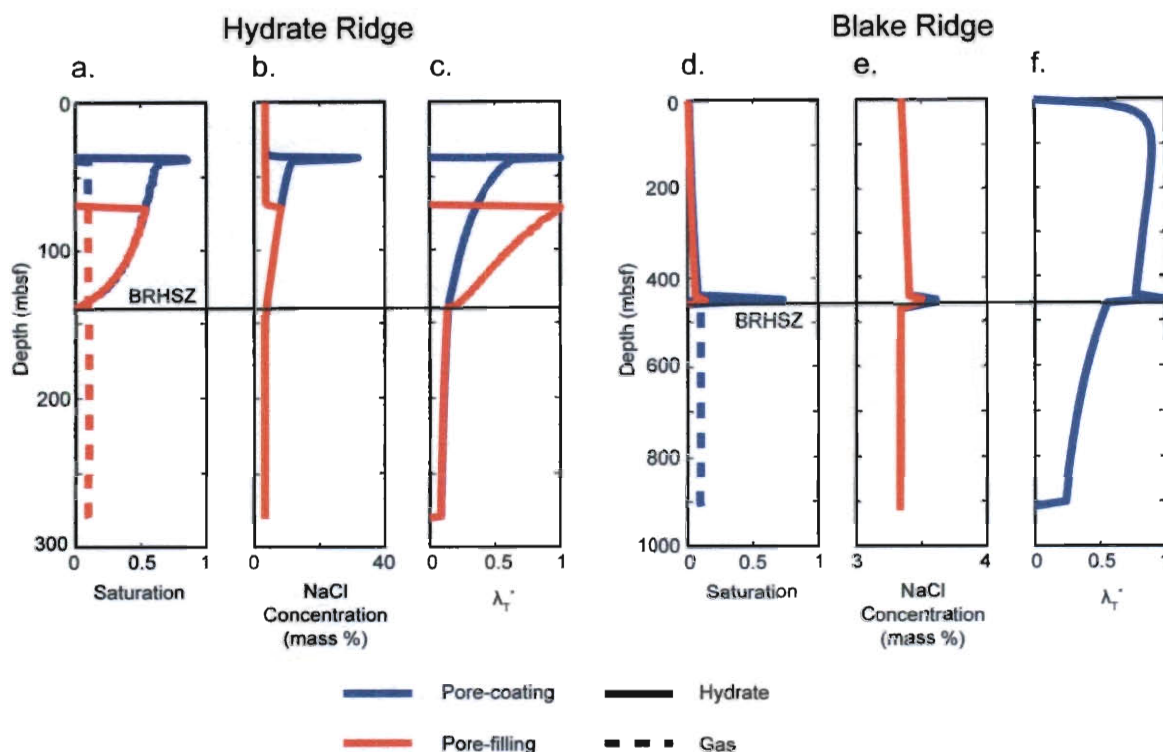
Figure 5.2 Comparison of model results using pore-coating and pore-filling hydrate growth habits. (a) S_h and S_g at Hydrate Ridge. Pore-filling hydrate (red) reduces permeability more rapidly than pore-coating hydrate (blue), so the fracture criterion can be achieved at lower S_h in the case of pore-filling hydrate. The time to reach the fracture criterion is shortened from 1.9×10^3 to 1.0×10^3 years with pore-filling hydrate. S_h follows the same trend in both cases since the growth habit does not affect the S_h and salinity required for three-phase equilibrium. (b) Salinity at Hydrate Ridge follows the same trend with depth for both growth habits since mass balance for salt is independent of growth habit. (c) λ^*_T is driven higher by pore-filling hydrate (red) than by pore-coating hydrate (blue), and the fracture criterion is achieved lower in the RHSZ. (d) S_h and S_g at Blake Ridge. The overall trends of the saturations are not altered by the hydrate growth habit, but fracturing occurs at lower S_h in the pore-filling case. (e) Salinity at Blake Ridge is slightly higher in the pore-coating case because of the higher S_h. However, salt is still removed in the porewater flux regardless of the hydrate growth habit, so the overall salinity trend is not altered. (f) λ^*_T follows the same trend in both cases since S_h is low.

Ridge produces fractures lower in the RHSZ after 10^3 years with maximum $S_h = 0.6$ (Figure 5.2), but this does not alter trends of S_h and salinity with depth.

Our model for Blake Ridge assumes $d_{sf} = 2781$ m, $T_{sf} = 276.4$ K, $dT/dz = 0.04$ K m^{-1} (Shipboard Scientific Party, 1996). φ is based on the bulk density log from ODP Leg 164 Site 997 (Lee, 2000). k and a J-function are estimated from pore throat measurements made by mercury injection capillary pressure (Henry et al., 1999). We assume $P_w^* = 4$ MPa at the base of the model domain from pressure core data (Flemings et al., 2003). After 1.6×10^4 years, $S_h = 0.72$ at the BRHSZ (~455 mbsf), and P_T^* at this point exceeds σ_{vh}' (Figure 5.1). However, because of the water flux driven by the P_w^*, the salinity within the RHSZ never increases to the point required for three-phase equilibrium. Thus methane is supplied to the RHSZ as a dissolved phase in the porewater. At the time when fracturing occurs, hydrate has formed in almost the entire RHSZ and $S_h = 0.02$–0.08 below 30 mbsf, except at the BRHSZ where $S_h = 0.72$. The trend of S_h decreasing upwards from a maximum at the BRHSZ is consistent with a system where methane is supplied only as a dissolved phase in the porewater (e.g., Rempel and Buffett, 1997), and matches the S_h values and trend with depth inferred from acoustic logs at Blake Ridge (Lee, 2000).

5.4. Discussion

The differences between Hydrate Ridge and Blake Ridge illustrate how S_h and fracture behavior are determined by the phase of methane supply (Figure 5.3). Hydrate Ridge is a gas-dominated system. Since there is no water flux (i.e., $P_w^* = 0$), hydrate may only form if methane is supplied by gas flux. Fractures form at the top of the gas column
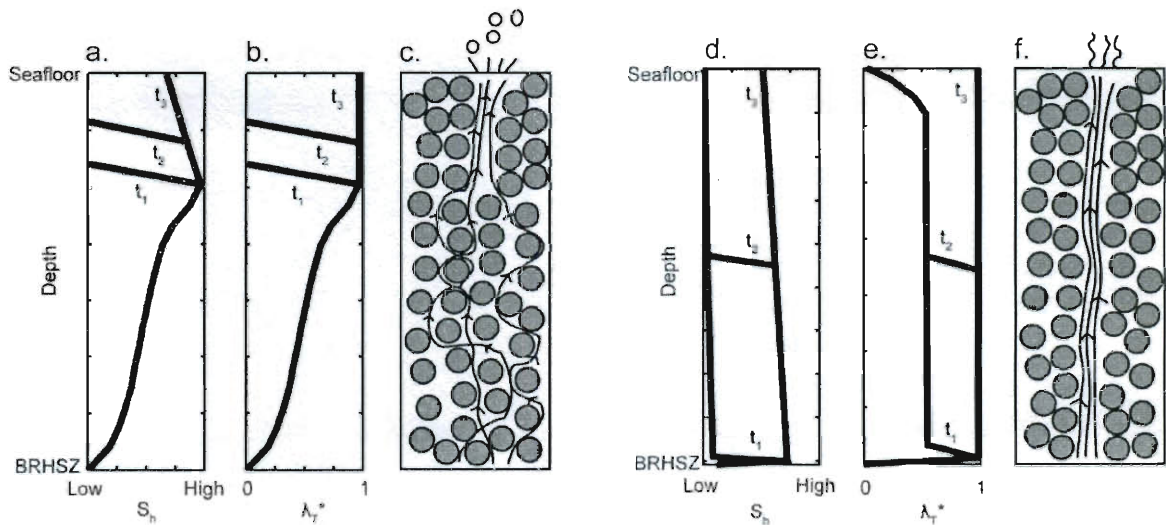
Figure 5.3 (a) In a gas-dominated system, fractures initiate at the top of the gas column at time t_1. Fracturing continues upwards as hydrate accumulates in existing fractures and increases P_c (t_2) until fractures reach the seafloor (t_3). Above the fracture nucleation point, S_h decreases since the effective stress decreases, requiring less hydrate to drive pore pressures to the point of failure. (b) Evolution of λ_T^*. λ_T^* reaches 1 at t_1, and fractures propagate upwards as λ_T^* reaches 1 shallower in the system (t_2) until fractures reach the seafloor (t_3). (c) Conceptual model of gas migration pathways in a gas-dominated system. Gas moves through the pore space up to the point where fractures initiate, and through fractures above that point. Free gas vents to the seafloor, potentially forming pockmarks and releasing gas bubbles. (d) In a water-dominated system, gas is unable to enter the RHSZ. Fractures initiate at the BRHSZ when hydrate and free gas accumulation drives λ_T^* sufficiently high (t_1). As hydrate accumulates higher in the RHSZ, fractures can propagate upwards (t_2) until they reach the seafloor (t_3). (e) Evolution of λ_T^*. λ_T^* reaches 1 at the BRHSZ (t_1), and as hydrate forms shallower in the RHSZ, fractures propagate upwards (t_2) until they reach the seafloor (t_3). (f) Conceptual model of water migration pathways in a water-dominated system. When fractures reach the seafloor, water moves preferentially through the fractures and reaches the seafloor in focused zones of high flux, creating seeps and chemosynthetic communities at the seafloor. Lower flux occurs through the pore system.

where hydrate formation has caused a sufficient increase in P_c. Fractures will propagate

upwards to the seafloor as λ_T^* approaches 1 shallower in the RHSZ; this eventually will

allow gas to vent to the seafloor. The result is a mixture of fracture-hosted and

disseminated hydrate, since disseminated hydrate forms before fractures. This hydrate

distribution is consistent with observations from image logs and cores at Hydrate Ridge

(Shipboard Scientific Party, 2003; Weinberger and Brown, 2006). Blake Ridge is a

water-dominated system. The water flux, driven by P_w^*, removes excess salt generated by

hydrate formation, so while gas can exist below the RHSZ, methane may only be

transported into the RHSZ by flux of methane-charged porewater. Fractures form at the

BRHSZ and may propagate upwards as λ_T^* approaches 1. This will result in focused

water flux where fractures intersect the seafloor.

Our results have additional implications for the hydrate systems at Hydrate Ridge

and Blake Ridge. Hydrate Ridge is interpreted as a hydrate system in which methane is

supplied from below the RHSZ (Claypool et al., 2006) at flow rates up to 300–1000 mm

yr^{-1} at active seeps (Torres et al., 2002); the shallowest sediments are Pleistocene in age

(Chevallier et al., 2006), and the present configuration of the RHSZ is believed to have

evolved following the last glacial maximum (Bangs et al., 2005). We predict that

fractures begin forming ~1600 years after free gas enters the RHSZ, and that gas flux into

the BRHSZ is ~350 mm yr^{-1} at the time of fracture initiation. While we do not constrain

the time required for fractures and free gas to reach the seafloor, fracturing and fracture

propagation should be relatively rapid (Valkó and Economides, 1995). Thus our results

are consistent with age constraints, flow rates, and methane supply pathways observed at

Hydrate Ridge, and support interpretations of Hydrate Ridge as a young, active hydrate province dominated by flux of methane gas from a deep reservoir.

We are able to match the observed hydrate distribution at Blake Ridge after 1.6×10^4 years, but our predicted water flux and lack of gas in the RHSZ do not match observations. We predict a water flux of 67 mm yr^{-1} at the time of fracturing based on k, S_h, and P_w^*, in contrast with 0.2 mm yr^{-1} inferred from porewater chlorinity (Egeberg and Dickens, 1999); and free gas has been interpreted in the RHSZ from seismic data (Gorman et al., 2002). There is evidence that water and gas at Blake Ridge may flow in focused zones along unconformity surfaces, resulting in fluctuating temperatures and pressures at the BRHSZ (Hornbach et al., 2008). The gas column we predict below the RHSZ is consistent with observations from log and seismic data (Guerin et al., 1999; Lee, 2000), and pressure core data indicate that the gas is at or near the pressure required for fracturing (Flemings et al., 2003). Hornbach et al. (2004) report that critically-pressured gas columns are common beneath hydrate deposits, and we propose that they are characteristic features of water-dominated systems. The discrepancy between observations and our results suggests that hydrate accumulation at Blake Ridge is driven by episodic, focused flow, and that migration of gas through the RHSZ is controlled mainly by pressure fluctuations.

Significant flux through hydrate systems may influence the temperature due to advective heat transport. To evaluate the validity of our assumption of constant geothermal gradient, we compute the Nusselt number Nu for each site. Nu is the ratio of total heat flow to heat flow due to conduction alone (Ingebritsen et al., 2006):

$$Nu = \frac{c_f \rho_f q_f T + K_m \dfrac{dT}{dz}}{K_m \dfrac{dT}{dz}} ,$$ (Equation 5.2)

where c_f is the fluid heat capacity [J kg^{-1} K^{-1}], ρ_f is fluid density [kg m^{-3}] and q_f is Darcy velocity [m s^{-1}], T is average temperature in the RHSZ [°C], and K_m is the bulk sediment thermal conductivity ($\sim$1.0 W m^{-1} K^{-1}; e.g., Tréhu, 2006). At Hydrate Ridge, using our computed gas flux we obtain $Nu = 1.0$. At Blake Ridge, using our computed water flux we obtain $Nu = 3.7$. There will thus be a small component of advective heat transport at Blake Ridge, but very little at Hydrate Ridge. Additional perturbations to the temperature field could be caused by latent heat of hydrate formation (e.g., Garg et al., 2008); hydrate formation releases heat, which increases the local temperature. Increased temperature requires lower salinity and thus lower S_h to reach three-phase equilibrium, so at Hydrate Ridge gas could propagate higher into the RHSZ, forming fractures closer to the seafloor. In reality the excess heat generated by hydrate formation could be removed efficiently by lateral conductive/advective heat transfer, which we do not include in our 1-D model.

5.5. Conclusions

We simulate multi-phase fluid flow at Hydrate Ridge, a gas-dominated system, and Blake Ridge, a water-dominated system. At Hydrate Ridge, free gas enters the RHSZ as hydrate forms; the gas migrates upwards by fracturing the sediment, and eventually vents to the seafloor. This results in increasing S_h upwards in the RHSZ, hydrate distributed in the pore space and in fractures, and free gas throughout the RHSZ. At Blake Ridge, free gas is unable to enter the RHSZ because water flux removes excess salt

before it reaches three-phase equilibrium. Hydrate forms throughout the RHSZ, with the highest S_h at the BRHSZ. Free gas may initiate fractures only at the BRHSZ. The critically-pressured column of gas that develops beneath the RHSZ is characteristic of water-dominated systems and affects sediment column stability. Our results here provide an important delineation of the differences between water-dominated and gas-dominated systems in terms of observable characteristics and shallow geohazard assessment.

6. Capillary controls on methane hydrate distribution and fracturing in advective systems[1]

6.1. Introduction

Methane hydrates are crystalline compounds of methane and water that are stable at the low temperatures and high pressures typical of continental margins and permafrost environments. Hydrates have been a topic of active research for the past several decades due to their potential role as climate change agents (Dickens et al., 1997; Archer and Buffett, 2005), submarine geohazards (Kvenvolden, 1993; Dillon et al., 1998), and energy resources (Collett, 1992; Boswell, 2009). Understanding the factors that control hydrate accumulation and distribution is an integral part of these research areas. At borehole- to basin-scales, hydrate systems can be described in similar terms as conventional hydrocarbon systems, with distribution and accumulation influenced by methane source and supply pathways (Tréhu et al., 2006; Boswell et al., 2010). However, at the pore scale, sediment physical properties exert a strong influence on hydrate formation and distribution (Clennell et al., 1999). Many investigations have focused on the nature of these influences theoretically (e.g., Clennell et al., 1999; Henry et al., 1999; Turner et al., 2005; Sun and Mohanty, 2006; Anderson et al., 2009; Jain and Juanes, 2009; Kvamme et al., 2009) and in the laboratory (e.g., Handa and Stupin, 1992; Uchida et al., 1999; Tohidi et al., 2001; Uchida et al., 2002; Anderson et al., 2003a; Anderson et

al., 2003b; Uchida et al., 2004; Hyodo et al., 2005; Lee et al., 2007; Yun et al., 2007; Lee et al., 2008; Masui et al., 2008).

Sediment physical properties can influence hydrate distribution by influencing fluid flow pathways, which affects methane supply, and by changing the local conditions for hydrate stability. Permeable layers can act as preferential conduits for flow of methane gas and methane-charged pore water (e.g., Weinberger and Brown, 2006), making these layers preferential sites for hydrate formation. This effect has been invoked to explain preferential hydrate occurrence in sand layers on scales of 10-100 m (e.g., Boswell et al., 2010; Dai et al., in press). At the pore scale, fine-grained sediments can inhibit hydrate formation through capillary-induced freezing point depression (e.g., Clennell et al., 1999); this effect is known as the Gibbs-Thomson effect. We focus on the Gibbs-Thomson effect because it has recently been invoked to explain cm-scale partitioning of hydrates in coarse-grained turbidite layers (Torres et al., 2008; Malinverno, 2010), and thus influences pore pressure distribution and fracturing. This represents an important modeling step to move beyond the steady-state stability assumptions that have been made in previous models (e.g., Rempel and Buffett, 1997; Xu and Ruppel, 1999; Davie and Buffett, 2001; Nimblett and Ruppel, 2003; Bhatnagar et al., 2007).

We extend the model of Chapter 4 to include solubility changes in fine-grained sediments caused by the Gibbs-Thomson effect. This new model simulates 1-D flow of a constant fluid flux through a layered porous medium with alternating coarse- and fine-grained layers. We neglect sedimentation and compaction and assume that constant fluid flux is a valid assumption over short time scales. We include poromechanical coupling to

allow hydraulic fracturing if pore pressure exceeds the minimum horizontal stress and assume that the sediments are cohesionless and have zero tensile strength (Behrmann, 1991; Day, 1992). Pore pressure increase is computed from Darcy's law as hydrate occludes the sediment pore space using our assumption of constant flux. We apply this model to two locations where hydrates have been observed preferentially filling thin, coarser-grained layers: Hydrate Ridge offshore Oregon (Ocean Drilling Program (ODP) Leg 204 Site 1250), and northern Cascadia offshore Vancouver Island (Integrated Ocean Drilling Program (IODP) Expedition 311 Site U1325) (Figure 6.1). We show that after 10,000 years, thin coarse-grained layers at Hydrate Ridge fill with hydrate and increased pore pressure causes fractures to form through the intervening fine-grained layers. This hydrate distribution matches the heuristic model proposed for hydrate accumulation at Hydrate Ridge (Weinberger et al., 2005; Weinberger and Brown, 2006) and the time scale is consistent with sediment ages (Chevallier et al., 2006). At northern Cascadia, we predict that 2×10^5 years are required to match the hydrate saturation in the coarse-grained layers, and that the intervening fine-grained layers do not fracture. The lack of fractures is consistent with observations from image logs, but the time scale is too long given constraints on sediment ages (Riedel et al., 2006). Hydrate accumulation at this site is likely enhanced by in situ production of biogenic methane in the fine-grained layers (Malinverno, 2010). We use our methodology to determine the maximum thickness of hydrate-free fine-grained layers layers between coarse-grained layers; the set of sediment physical properties and methane supply rates necessary to produce hydrate-filled coarse-grained layers connected by fractured fine-grained layers; and the conditions required for sediments to experience capillary-induced shutdown of hydrate formation as hydrate
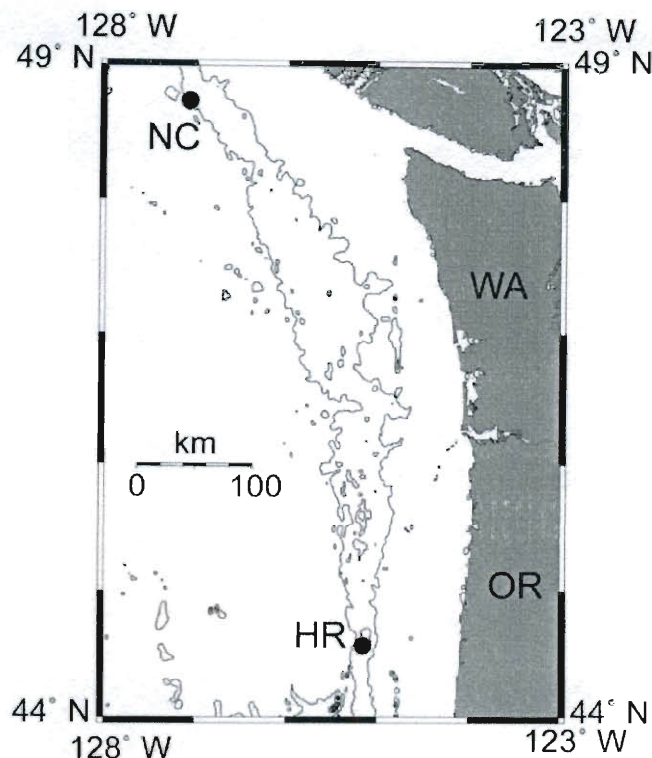
Figure 6.1 Location map showing Hydrate Ridge (HR) and northern Cascadia (NC) on the Cascadia Margin offshore Washington (WA) and Oregon (OR), USA, and Vancouver Island, Canada. Bathymetric contour interval is 1000 m.

constricts pores and drives solubility upwards. Our results outline the conditions required to develop hydrate-filled coarse-grained layers interbedded with hydrate-free fine-grained layers, and to develop throughgoing fractures through the fine-grained layers.

6.2. Background

6.2.1 Lithologically partitioned hydrate

Methane hydrate has been observed to accumulate preferentially in coarser-grained intervals at several locations worldwide. At sites on Blake Ridge, investigated

during ODP Leg 164, hydrate abundance was found to increase with increasing sediment grain size (Ginsburg et al., 2000; Kraemer et al., 2000). This was interpreted to be the result of capillary effects (Kraemer et al., 2000). At sites on Hydrate Ridge, investigated during ODP Leg 204, hydrate was observed preferentially filling thin (<0.5 cm) sand layers (Weinberger et al., 2005) connected by fractured fine-grained layers (Weinberger and Brown, 2006). The observed hydrate distribution may be the result of preferential methane gas migration through more permeable layers (Weinberger and Brown, 2006) or hydraulic fracturing of lower-permeability layers driven by excess pore fluid pressure resulting from hydrate formation (Chapter 4). At sites offshore Vancouver Island investigated by IODP Expedition 311, hydrate was found preferentially in thin (5 cm), coarse-grained layers of a turbidite sequence (Malinverno et al., 2008; Torres et al., 2008; Malinverno, 2010). The observed distribution has been attributed to capillary effects on solubility (Torres et al., 2008; Malinverno, 2010).

In all these cases, the preferential accumulation of hydrate in coarser-grained layers has been ascribed to physical properties of the sediment affecting either methane supply pathways or hydrate formation kinetics. An additional control on hydrate distribution is the availability of water, which limits the rate of hydrate formation (e.g., Svandal et al., 2006); for instance, if some hydrate forms in the pore space of a low-permeability sediment, the replenishment of pore water may be slow, thus limiting the rate of hydrate growth (e.g., Liu and Flemings, 2006; Liu and Flemings, 2007). Marine sediments are expected to be fully saturated with water initially with an essentially unlimited reservoir of pore fluid, so any effects due to limited water supply will be highly

localized, and are not expected to be significant on geologic time scales or at the borehole to basin scale.

Sediment lithology can also affect hydrate distribution by focusing fluid flow and methane supply. Preferential fluid pathways such as high-permeability layers (e.g., Weinberger and Brown, 2006; Crutchley et al., 2010) and fractures (Chapter 4) have been investigated by previous authors. These pathways affect the hydrate distribution by focusing methane in the dissolved or free gas phase, resulting in more rapid hydrate accumulation where the methane supply is focused. Flow focusing becomes especially important when two or three spatial dimensions are considered (e.g., Crutchley et al., 2010), but to obtain first-order observations we simulate flow in a well constrained, 1-dimensional domain. We focus on the capillary effect on solubility as its implications are not fully understood. Capillary effects are driven by lithology, which varies at local and regional scales, so capillary effects may exert significant and complex controls on hydrate distribution.

6.2.2 Gibbs-Thomson effect

When a liquid undergoes a phase change to the solid state in a small (micro- to nanometer-scale) pore, the resulting solid particle has a high surface area to volume ratio, and the solid-liquid interfacial energy becomes an important contribution to the total Gibbs free energy of the system. In porous media, the activity of the remaining liquid in the pore decreases because of adsorption of liquid molecules onto the pore walls (Handa and Stupin, 1992; Clennell et al., 1999). The decreased liquid activity and increased Gibbs free energy increases the solubility of the solid phase in the liquid and depresses

the freezing point of the solid. This is known as the Gibbs-Thomson effect (Thomson, 1871; Porter and Easterling, 1992), and has been observed in laboratory experiments involving dissociation of methane hydrate (e.g., Handa and Stupin, 1992; Berge et al., 1999; Uchida et al., 1999; Winters et al., 1999; Tohidi et al., 2001; Uchida et al., 2002; Anderson et al., 2003a; Anderson et al., 2003b; Uchida et al., 2004; Anderson et al., 2009). The freezing point depression ΔT_f [K] can by computed by (Anderson et al., 2009)

$$\Delta T_f = -T_{f,b} \frac{F \gamma_{sl}}{r \rho_s \Delta H_{sl}},$$ (Equation 6.1)

where $T_{f,b}$ is the freezing point in free liquid [K], F is a geometric factor that depends on interfacial curvature, γ_{sl} is the interfacial energy between the solid and liquid phases [J m^{-2}], r is the pore radius [m], ρ_s is the bulk density of the solid phase [kg m^{-3}], and ΔH_{sl} is the latent heat of fusion of the solid phase [J mol^{-1}]. The geometric factor F is related to the curvature of the solid-liquid interface by

$$F = r \left(\frac{1}{r_1} + \frac{1}{r_2} \right),$$ (Equation 6.2)

where r_1 and r_2 are orthogonal radii of curvature [m]. In spherical and cylindrical pores, $r_1 = r_2 = r$ so $F = 2$ (Anderson et al., 2009). In methane hydrate systems, the depression in freezing point results in an increase in methane solubility at constant temperature and pressure (Davie and Buffett, 2001).
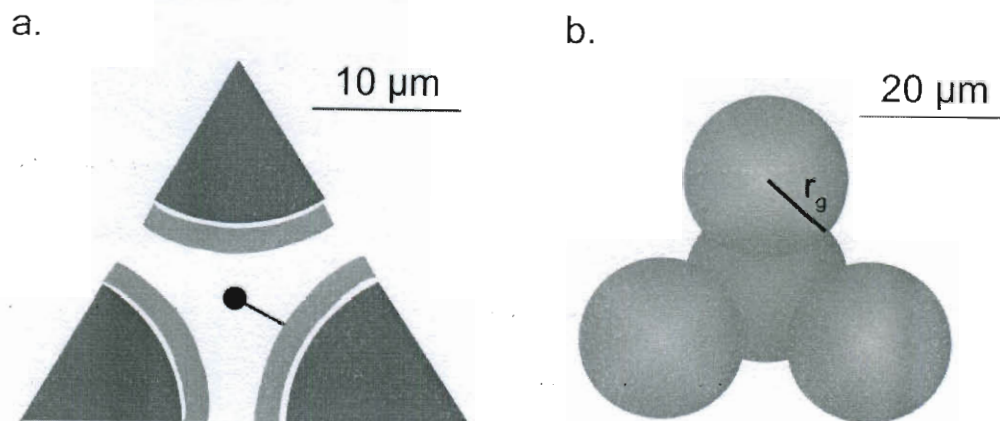
Figure 6.2 Schematic illustrations of pore system considered in our model to show system dimensions. (a) Cross-section through a plane defined by the centers of three adjacent grains showing hydrate growth habit and pore size. Hydrate is assumed to grow as a uniform coating around the grains with a thin film of water between hydrate and grain. The pore radius is shown by the black line normal to the surface of the hydrate. Hydrate growth occurs inward towards the center of the pore. (b) Illustration of pore surrounded by four spherical grains. The grains have radius r_g.

Since Equation 6.1 is valid for hydrate as a non-wetting phase, we consider hydrate growth in a manner similar to Anderson et al. (2009) where hydrate forms immediately adjacent to sediment grains but is separated from the grains by a thin film of water that does not contribute to the permeability of the system (Figure 6.2a). Hydrate growth proceeds inward toward the center of the pore. Anderson et al. (2009) report hysteresis in freezing point depression during formation-dissociation cycles, with the magnitude of depression being greater during formation than during dissociation. They attribute this hysteresis to the combined effects of differing curvatures of interfacial surfaces during formation and dissociation (e.g., Brun et al., 1977; Faivre et al., 1999) and "pore-blocking" in which capillary entry pressure in narrow pore throats must be overcome during hydrate crystal growth but not during dissociation (e.g., Mason, 1981). Pore blocking is a process analogous to capillary blockage in two-phase flow of gas and

water (e.g., Revil et al., 1998, Shosa and Cathles, 2001). For simplicity we assume that there is no hysteresis in our model, so the Gibbs-Thomson effect should have the same effect on hydrate dissociation as on hydrate formation. We employ this assumption as we focus on hydrate formation. Additionally, since we assume that water is the only fluid phase and that the porous medium is fully saturated with water initially, we do not consider capillary entry effects.

6.2.3 Advective versus diffusive systems

Systems in which methane is transported into the regional hydrate stability zone (RHSZ) by pore fluid advection are termed advective systems. These stand in contrast to systems in which methane is transported by chemical diffusion, which are termed diffusive systems. Formation of large methane hydrate deposits by diffusion alone is unlikely due to the long time scales required (Xu and Ruppel, 1999). Hydrate deposits therefore require a combination of advective flux of methane and in situ biogenic production of methane to form in reasonable lengths of time (e.g., Nimblett and Ruppel, 2003; Bhatnagar et al., 2007). At small length scales, such as the thin, hydrate-bearing layers at Hydrate Ridge and northern Cascadia, however, diffusion may be an important mode of methane transport. Malinverno (2010) recreated the observed hydrate distribution at northern Cascadia by assuming diffusive transport of biogenic methane out of fine-grained layers and into coarse-grained layers where the lower methane solubility allowed hydrate to form more easily than in the fine-grained layers; on the order of 100 years were required to match observed hydrate saturations. In advective systems where methane flux may be high, we explore the influence of the Gibbs-Thomson effect relative

to effects related to rates of methane supply in layered, advective systems where methane is dominantly supplied from below the RHSZ.

6.3. Model implementation and assumptions

6.3.1 Model domain

We simulate one-dimensional flow of pore water with dissolved methane upwards through a porous medium (Figure 6.3). We prescribe seafloor depth and temperature d_{sf} [m] and T_{sf} [K], and a constant geothermal gradient dT/dz [K m^{-1}]. These parameters define the thickness of the RHSZ along with assumptions of hydrostatic conditions at the seafloor and seawater salinity (3.35% by mass) through the RHSZ. We do not consider perturbations to the geothermal gradient due to the presence of hydrate, which has a thermal conductivity approximately equal to that of water but small compared to that of quartz (Waite et al., 2009); we assume that the geothermal gradient can be assumed constant unless S_h is high. The model domain is a 1-20 m-thick subsection of the RHSZ. We assign porosity φ and grain radius r_g [m] in the model domain. We assume that the porous medium can be represented by a packing of uniform spheres and compute permeability k [m^2] using the formula of Bryant et al. (1993a) where $k = 0.00272r_g^2$. This formula provides an initial permeability for our porous medium based on the median grain radius, and may not capture the full complexity of pore networks in natural samples (e.g., Johnson et al., 1986; Katz and Thompson, 1986; Revil and Cathles, 1999; Revil and Florsch, 2010). This assumption results in non-spherical pores. We assume that the pore radius in Equation 6.1 can be represented by the radius of an inscribed sphere in the pore, an assumption made by other investigations of spherical packs (e.g., Prodanović and
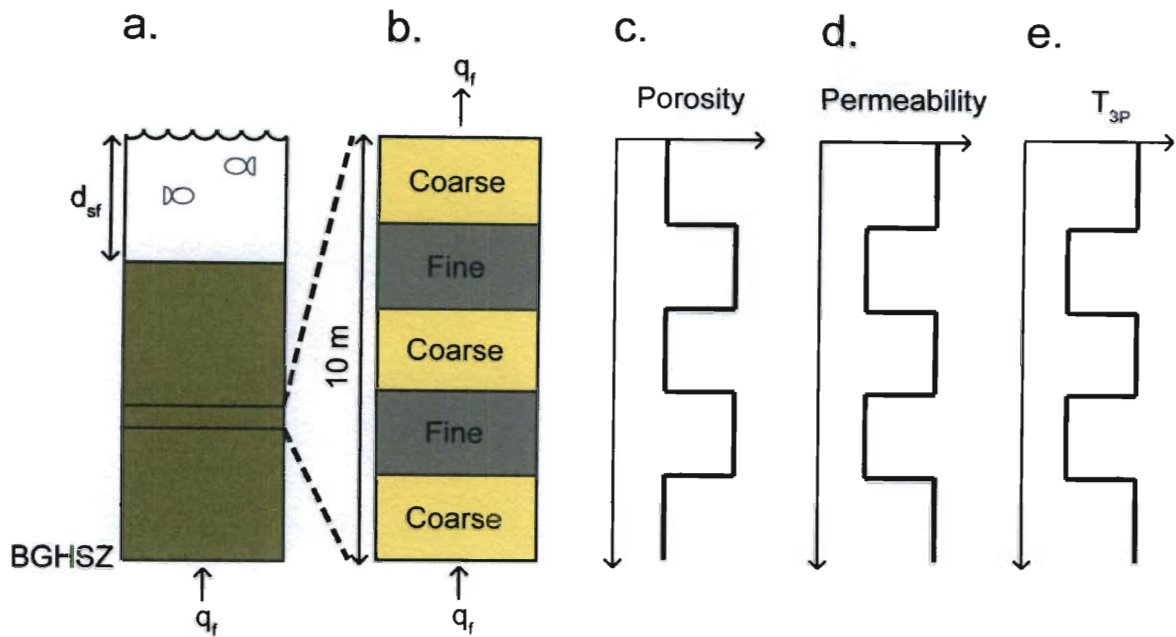
Figure 6.3 Illustration of model domain. (a) We first define a seafloor depth, seafloor temperature, and geothermal gradient, which in turn define the depth to the base of the gas hydrate stability zone (BGHSZ). (b) Fluid flows at a constant rate q_f into the base of the system. We select a smaller section of the RHSZ for modeling, and define thicknesses of coarse-grained and fine-grained layers. We assign porosity (c) and initial permeability (d) in each layer. The grain size in each layer determines the change in the methane triple point temperature (ΔT_{3P}) from the Gibbs-Thomson effect (Equation 6.1), which we subtract from the free water triple point temperature to obtain the initial triple point temperature (T_{3P}) curve (e).

Bryant, 2006; Behseresht, 2008). Fluid flow is assigned a constant value, and the pore pressure in excess of hydrostatic is computed from Darcy's law and the permeability values. We assume that constant fluid flow is a reasonable approximation for short length and time scales. This assumption follows other steady-state models of hydrate accumulation (e.g., Rempel and Buffett, 1997; Xu and Ruppel, 1999; Bhatnagar et al., 2007). Pulses of higher fluid flux may occur over short time scales in natural systems, particularly on convergent margins (e.g., Tryon et al., 2002; Brown et al., 2005). We do not consider fluid flux pulses in our model, and thus our constant flux assumption

represents a time average. Over geologic time scales, this assumption would need to be revised to account for compaction and variable flux.

6.3.2 Methane solubility, hydrate formation, and permeability reduction

For simplicity, we assume that the pores in the system are bounded by tetrahedra composed of four grains (Figure 6.2b). The radius of the pore in such a system is given by $(\sqrt{2}-1)r_g$. We compute the triple point temperature for dissolved methane-methane hydrate-methane gas equilibrium T_{3P} [K] at in situ temperature and pressure using the method of Duan et al. (1992). We then compute the change in T_{3P} due to the Gibbs-Thomson effect using Equation 6.1 with $F = 2$, $\gamma_{sl} = 0.027$ J m^{-2} (Clennell et al., 1999), $\rho_s = 925$ kg m^{-3}, and $\Delta H = 5.45\times10^4$ J mol^{-1} (Waite et al., 2009). Using the Gibbs-Thomson-corrected T_{3P}, we compute methane solubility in the RHSZ using the method of Bhatnagar et al. (2007).

Hydrate formation is computed by solving a mass balance for methane, assuming that methane is only present as hydrate or dissolved in the pore water:

$$\frac{\partial}{\partial t}\left[\varphi(1 - S_h)\rho_w c_m^l + \varphi S_h c_m^h \rho_h\right] - \frac{\partial}{\partial z}\left[\bar{\mathbf{q}}_f \middle| c_m^l \rho_w\right] = \frac{\partial}{\partial z}\left[\varphi(1 - S_h)D_z \rho_w \frac{\partial c_m^l}{\partial z}\right],$$

(Equation 6.3)

where S_h is hydrate saturation, ρ_w and ρ_h are the bulk densities of water and hydrate [kg m^{-3}], c_m^l and c_m^h are the mass fractions of methane in water and hydrate [kg kg^{-1}], $\bar{\mathbf{q}}_f$ is the rate of fluid flow [m s^{-1}], and D_z is the coefficient of hydrodynamic dispersion [m^2 s$^-$

[1]. We assume $\rho_w = 1024$ kg m^{-3}, $\rho_h = 925$ kg m^{-3} (Waite et al., 2009), and $c_m^h = 0.134$ kg

kg^{-1}. D_z is equal to $\dfrac{a_L |\vec{\mathbf{q}}_f|}{\varphi} + D_m$, where a_L is the longitudinal dispersivity [m] and D_m is

the coefficient of diffusion for methane in water [m^2 s^{-1}] (Ingebritsen et al., 2006). We

assume $D_m = 10^{-9}$ m^2 s^{-1} (Davie and Buffett, 2001). For flow at the meter scale, $a_L \approx 0.01$

m (Xu and Eckstein, 1995). Assuming $\varphi = 0.50$ and $|\vec{\mathbf{q}}_f| = 430$ mm yr^{-1}, which is the

highest flux we consider, $D_z = 1.3 \times 10^{-9}$ m^2 s^{-1}. Therefore we approximate D_z with D_m. We

solve Equation 6.3 using an explicit, forward-in-time, centered-in-space (FTCS) finite-

difference scheme with the initial condition $c_m^l = 0$ and $S_h = 0$ throughout the domain,

and the boundary conditions that c_m^l is 0 at the seafloor and is the value for solubility in

free water at the base of the domain.

As hydrate forms in the porous medium, the pore system is occluded, reducing the

permeability. We assume the hydrate forms a uniform coating around the sediment grains

analogous to an isopachous cement (Figure 6.2a). Following the cementation model of

Bryant et al. (1993b) we compute the reduced permeability k' [m^2] as

$$k' = k\left(1 - S_h\right)^4.$$ (Equation 6.4)

This permeability model results in more rapid permeability reduction with hydrate

saturation than the cylindrical pore-coating model that has been used in other

investigations (e.g., *Kleinberg* et al., 2003; Nimblett and Ruppel, 2003; Liu and

Flemings, 2007; Crutchley et al., 2010), but a less rapid reduction than the cylindrical
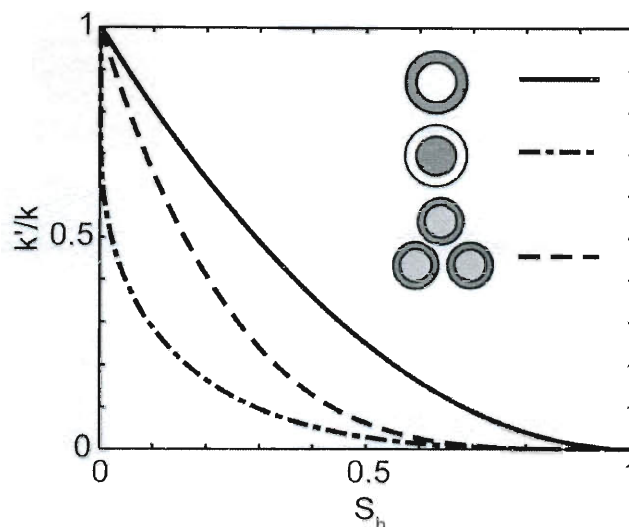
<u>Figure 6.4</u> Permeability reduction k'/k with increased hydrate saturation S_h for three different pore models. Solid line: cylindrical pores with hydrate coating the pore walls uniformly (Equation B10 of Kleinberg et al. (2003)). Dashed-dotted line, cylindrical pores with hydrate forming in the middle of the pores (Equation B14 of Kleinberg et al. (2003)). Dashed line: hydrate forming an isopachous cement on spherical grains (Equation 6.4). We use this isopachous cement model as the representation of the pore space because it is more realistic than parallel, cylindrical capillary tubes. The permeability reduction at a given S_h for this model is greater than for the cylindrical wall-coating model but less than for the cylindrical pore-filling model.

pore-filling model (Figure 6.4) (Kleinberg et al., 2003); we adopt the isopachous cement model as it is a more realistic representation of the sediment pore system than cylinders. As hydrate forms and pore space is occluded, our assumption of constant fluid flux results in an increase in pore fluid pressure, which we compute from Darcy's law using the reduced permeability (Equation 6.4). In addition to the reduction in permeability, the pore radius is also reduced as a result of hydrate formation by a factor of $(1 - S_h)^{1/3}$, such that the reduced pore radius is $(\sqrt{2} - 1)(1 - S_h)^{1/3} r_g$. We continually update T_{3P} and methane solubility for changes in pore fluid pressure and pore radius.

6.3.3 Fracture generation

We include poroelastic coupling to investigate whether the Gibbs-Thomson effect can produce a hydrate distribution characterized by hydrate filling the pore space in coarser-grained intervals and hydrate-filled fractures in finer-grained intervals. Hydraulic fracturing can be approximated as an elastic phenomenon. For a noncohesive sediment with zero tensile strength (Behrmann, 1991; Day, 1992), hydraulic fracturing will occur when the pore pressure exceeds the minimum principal stress (Valkó and Economides, 1995). In passive margins and shallow sediments of active margins, the maximum principal stress is typically vertical and the minimum principal stress horizontal. We compute σ_{vh}' [Pa], the vertical effective stress under hydrostatic conditions, at each depth by integrating the buoyant unit weight from the seafloor to that depth. The pore pressure in excess of hydrostatic P^* [Pa] is then computed from Darcy's law using the reduced permeability (Equation 6.4). Assuming linear elasticity, the horizontal effective stress under hydrostatic conditions σ_{hh}' [Pa] is related to σ_{vh}' by

$$\sigma_{hh}' = \frac{v}{1-v}\sigma_{vh}',$$

(Equation 6.5)

where v is Poisson's ratio. For fractures to form, P^* must overcome σ_{hh}'. The overpressure ratio λ^* is the ratio of P^* to σ_{vh}':

$$\lambda^* = \frac{P^*}{\sigma_{vh}'} = \frac{v}{1-v}\frac{P^*}{\sigma_{hh}'}.$$

(Equation 6.6)

By combining Equations 6.5 and 6.6, when $P^* = \sigma_{hh}'$, fracturing occurs; thus the fracture

criterion is that $\lambda^* \geq \dfrac{v}{1-v}$. We assume $v = 0.4$, which is a typical value for loosely

consolidated sediments (e.g., Karig and Hou, 1992; Reynolds, 1997). This results in a

fracture criterion of $\lambda^* \geq 0.67$.

Once fractures form, we compute the equivalent fracture permeability by

$$k = \frac{a^3}{12l},$$
(Equation 6.7)

where a is the fracture aperture [m] and l is the inter-fracture spacing of the fracture

system [m] (Snow, 1968); we assume that the fracture system that forms has $a = 1$ mm

and $l = 1$ m (e.g., Weinberger and Brown, 2006; Cook et al., 2008). Because the fracture

width is large compared to the size of pores, the methane solubility in the fractures is

reduced to the value in free water (i.e. no capillary effects). If hydrate forms in the

fractures, the fracture aperture is decreased by a factor of $1\text{-}S_h$, and the expression for

reduced permeability in the fracture system is

$$k' = k(1 - S_h)^3.$$
(Equation 6.8)

Our assumption of cohesionless sediment with zero tensile strength may introduce

small errors into the results. Tensile strength of soft sediments may range from 0 to 0.05

MPa, and cohesion is typically less than 0.5 MPa (Behrmann, 1991; Day, 1992).

Including these effects would result in higher pore pressure necessary for fractures to

form. However, at depths of a few hundred meters below seafloor, the vertical effective stress is several MPa, so the effects of cohesion and tensile strength are relatively small. Methane hydrate has the additional effect of strengthening sediment (e.g., Hyodo et al., 2005; Yun et al., 2007; Masui et al., 2008) because of the high mechanical strength of hydrate itself. This effect is most important at higher hydrate saturations ($S_h > 0.40$) (Yun et al., 2007) and certain hydrate habits (e.g. cementing at grain contacts). In general, by neglecting tensile strength and cohesion the time scales we compute are minimum endmembers.

6.4. Results

6.4.1 Hydrate Ridge

Our Hydrate Ridge model is based on ODP Leg 204 Site 1250, located near the crest of southern Hydrate Ridge. We assume $d_{sf} = 800$ m, $T_{sf} = 277$ K, and $dT/dz = 0.053$ K m^{-1} (Tréhu, 2006). The model domain consists of a 5 m-thick section with its base at 100 mbsf, composed of alternating layers of 1.5 m-thick fine-grained layers and 0.25 m-thick coarse-grained layers. This is representative of a zone with lithologically partitioned hydrate identified on image logs from Hole 1250B (Weinberger and Brown, 2006). To determine coarse-grained and fine-grained porosities, we used the gamma ray log from Site 1250 to differentiate coarse- and fine-grained layers using a cutoff value of 60 GAPI (coarse < 60 GAPI < fine). We then determined porosities by taking the average values of the bulk density log over the coarse-grained and fine-grained zones and computing porosity assuming a grain density of 2700 kg m^{-3}. This yielded $\varphi = 0.55$ in coarse-grained layers and $\varphi = 0.52$ in fine-grained layers. Grain sizes were determined from median

grain size and silt content at Site 1250 (Gràcia et al., 2006); this yielded a coarse grain diameter of 30 μm and a fine grain diameter of 0.5 μm. The corresponding initial permeabilities using $k = 0.000272r_g^2$ (Bryant et al., 1993a) were $6x10^{-13}$ m^2 in coarse-grained layers and $2x10^{-16}$ m^2 in fine-grained layers, which agree with laboratory measurements of permeability by Tan et al. (2006). We assume a flow rate of 430 mm yr^{-1}, which is in the range 300-1000 mm yr^{-1} inferred near the crest of Hydrate Ridge from porewater chloride concentration profiles (Torres et al., 2002).

After 2000 years, $S_h \approx 0.90$ in both coarse-grained layers, and no hydrate has accumulated in the intervening fine-grained layers (Figure 6.5a). As a result of hydrate forming in the coarse-grained layers and occluding the pore space, methane solubility in the coarse-grained layers increases by ~0.015 g kg^{-1} (Figure 6.5b). The lowermost fine-grained layer develops throughgoing fractures; λ^* equals the fracture criterion from the base of the domain to the top of this fine-grained layer, and fractures begin forming in the next fine-grained layer at 98.25 mbsf, bypassing the intervening coarse-grained layer (Figure 6.5c). Solubility in the fractured fine-grained layer drops to the value in free water (Figure 6.5b); the increase in solubility in the unfractured fine-grained layer is a result of the increase in pore fluid pressure as hydrate occludes pores in the overlying coarse-grained layer, reducing the coarse-grained layer permeability. After 10,000 years, the middle fine-grained layer (96.75-98.25 mbsf) develops throughgoing fractures (Figure 6.5c). Solubility in the coarse-grained layers increases an additional 0.01 g kg^{-1} due to further formation of hydrate (Figure 6.5b).
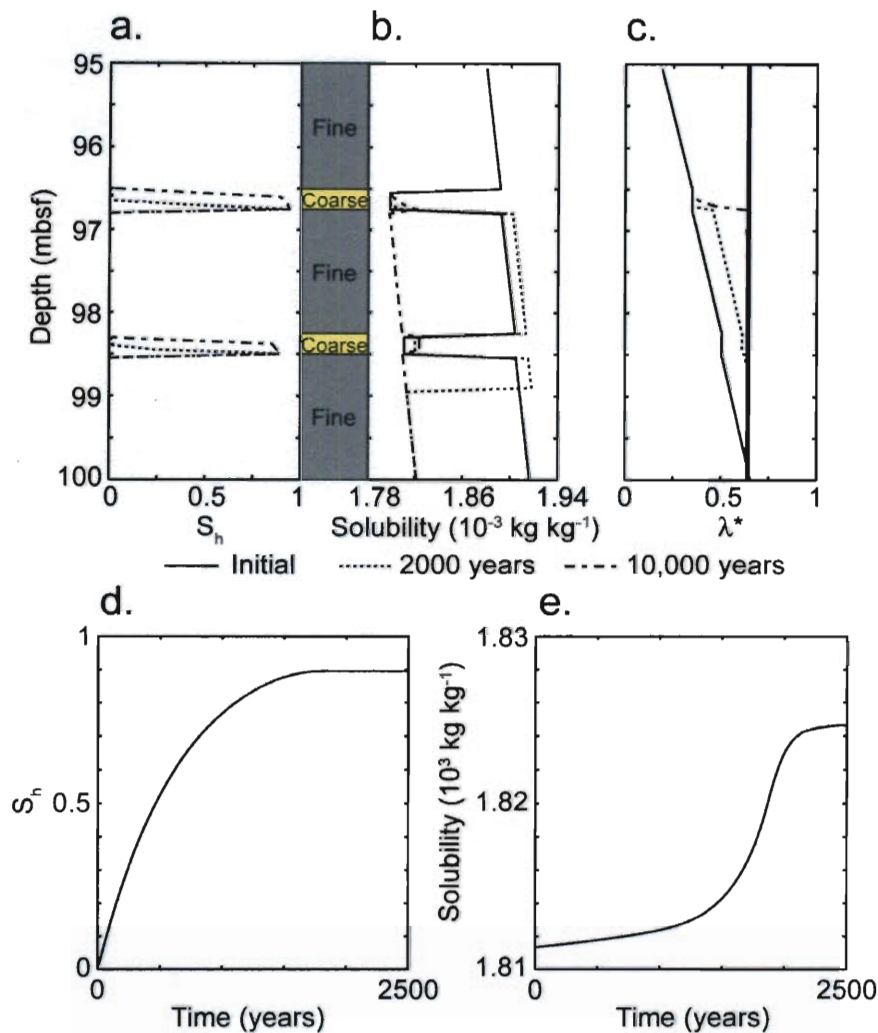
Figure 6.5 Model results for Hydrate Ridge. (a) Hydrate saturation. Both coarse-grained layers fill with hydrate to $S_h \approx 0.90$ after 2000 years, with little increase in S_h between 2000 and 10,000 years. This is attributable to fractures opening in the fine-grained layers after 2000 years and hydrate forming in the fracture system, reducing the amount of dissolved methane that reaches the coarse-grained layers. (b) Methane solubility in the pore fluid. Initially the solubility in the fine-grained layers is greater than that in the coarse-grained layers. After 2000 years, hydrate has formed in the coarse-grained layers and the solubility has increased slightly; the solubility in the fine-grained layers has increased slightly as well due to the increase in pore fluid pressure as hydrate occludes the pore space in the coarse-grained layers. Fractures have developed over the lowest 1 m of the lower fine-grained layer, and the solubility values reflect this as they have decreased to the value for free water. After 10,000 years, solubility in the coarse-grained layer s has increased slightly again as some additional hydrate has formed; fractures have developed in the fine-grained layers up to the base of the upper coarse-grained layer, and the solubility in this interval has dropped accordingly. (c) Overpressure ratio. The critical value is marked by the solid line at $\lambda^* = 0.67$. After 2000 years, the lowest 1 m of the system has reached the fracture criterion; after 10,000 years, the fine-grained layers up to the base of the upper coarse-grained layer have reached the fracture criterion, but the lower coarse-grained layer remains slightly below the fracture criterion. (d) Hydrate saturation versus time in the lower coarse-grained layer. S_h increases rapidly for ~1800 years, when fractures form and reduce the amount of methane reaching the coarse-grained layer. After this point, S_h increases very slowly. (e) Change in solubility versus time in the lower coarse-grained layer. The solubility increase that results from hydrate clogging the pores is small until $S_h \approx 0.80$, but solubility increases rapidly after this point as the pore space is occluded more quickly.

Hydrate accumulates first at the base of the lower coarse-grained layer. The accumulation rate decreases with time and S_h is nearly constant after 1800 years (Figure 6.5d). This is due to fractures opening in the fine-grained layer below the lowermost coarse-grained layer. Prior to fracture formation, hydrate cannot form in the fine-grained layer because the solubility is too high, so the pore fluid flows through the fine-grained layer without any decrease in dissolved methane concentration and enters the base of the coarse-grained layer with sufficient dissolved methane for hydrate to precipitate in the coarse-grained layer. However, methane solubility in fractures is lower than in the coarse-grained layers, so hydrate will form in the fractures, and the pore fluid entering the base of the coarse-grained layer will no longer have enough dissolved methane to allow hydrate formation in the coarse-grained layer. Solubility in the lower coarse-grained layer increases slowly at first (Figure 6.5e), but the rate increases rapidly when $S_h > 0.80$. This is due to the fact that the pore throats are constricted most rapidly at high S_h, driving solubility upwards because of the Gibbs-Thomson effect.

6.4.2 Northern Cascadia

Our northern Cascadia model is based on IODP Expedition 311 Site U1325, which is located in a depositional basin ~11 km landward from the deformation front. We assume $d_{sf} = 2195$ m, $T_{sf} = 276$ K, and $dT/dz = 0.06$ K m^{-1} (Riedel et al., 2006). The model domain consists of a 7.6 m-thick section with its base at 200 mbsf, composed of alternating 2.5 m-thick fine-grained layers and 0.05 m-thick coarse-grained layers. This is representative of the conditions in the turbidite sequence containing lithologically-bound hydrates (Malinverno, 2010). We assumed coarse-grained and fine-grained porosities of
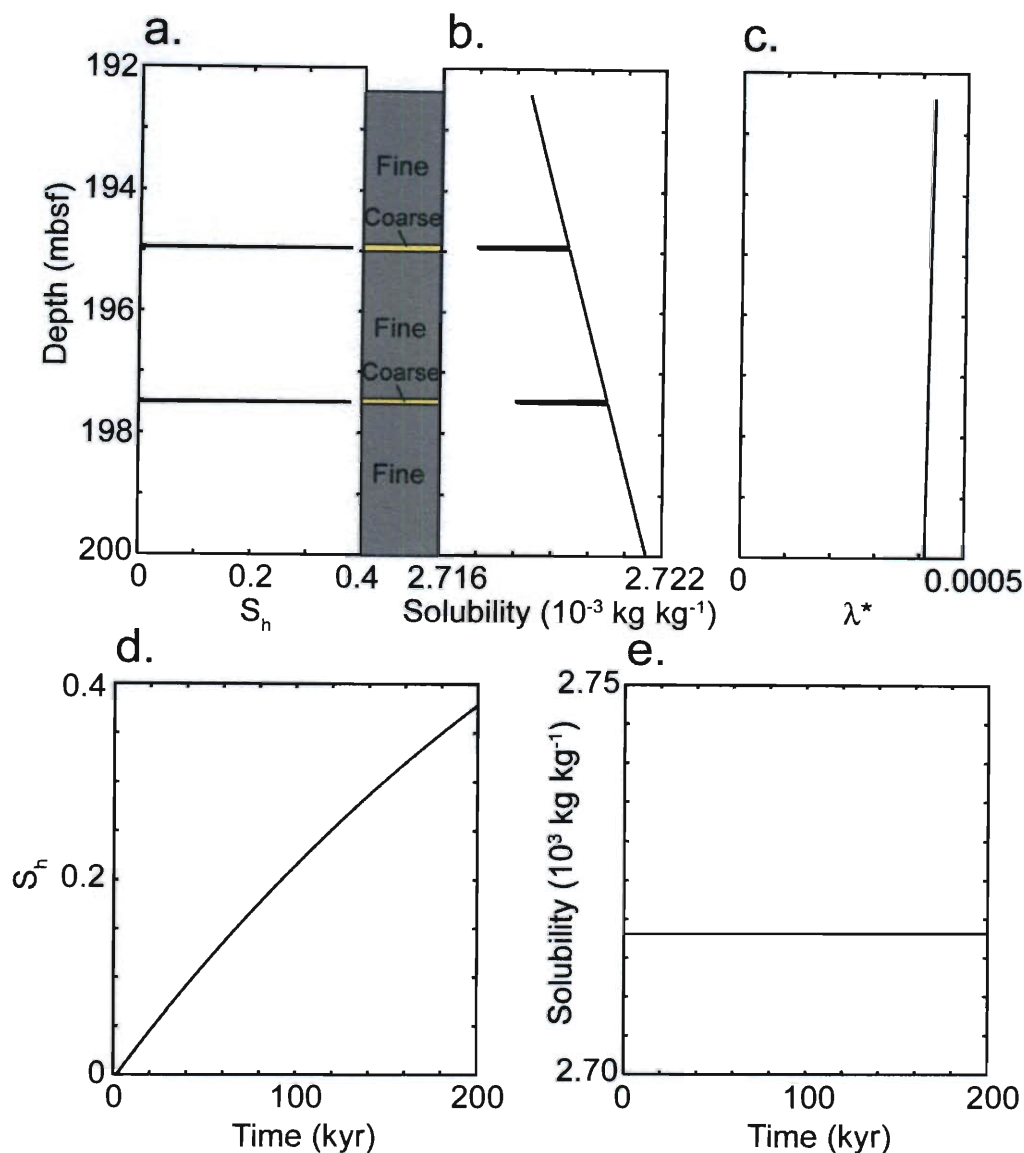
149

Figure 6.6 Model results for northern Cascadia after 2×10^5 years. (a) Hydrate saturation. S_h reaches nearly 0.40 in both coarse-grained layers, which matches observations (Malinverno et al., 2008). No hydrate forms in the intervening fine-grained layers. (b) Methane solubility in the pore fluid. There is almost no change in solubility from the initial conditions. This is due to the relatively large pore sizes at this site; not even filling the pore space to $S_h = 0.40$ reduces the pore size sufficiently to cause an appreciable change in solubility. (c) Overpressure ratio. The high permeability and low flow rate at this site result in very low λ^*. After 2×10^5 years, the system is not close to failure. (d) Hydrate saturation versus time in the lower coarse-grained layer. S_h increases nearly linearly with time; this rate is controlled by the low pore fluid flow rate since methane is only supplied by pore fluid flux. (e) Solubility in the lower coarse-grained layer versus time. The solubility value remains nearly constant because of the large pore size.

0.35 and 0.60, and coarse and fine grain diameters of 80 μm and 16 μm (Torres et al., 2008). The corresponding coarse-grained and fine-grained permeabilities from $k = 0.000272r_g^2$ (Bryant et al., 1993a) were $4x10^{-12}$ m^2 and $2x10^{-13}$ m^2. Vertical fluid flow rates in this area have been estimated at between 0.17 mm yr^{-1} (Malinverno et al., 2008) and 1 mm yr^{-1} (Bekins and Dreiss, 1992; Wang et al., 1993); we consider the upper limit to obtain a minimum estimate of time.

After $2x10^5$ years, $S_h \approx 0.40$ in the coarse-grained layers (Figure 6.6), which matches the range $S_h = 0.20\text{-}0.60$ obtained from log data in the coarse-grained layers (Malinvero et al., 2008). Unlike Hydrate Ridge, λ^* remains very small (Figure 6.6c), and the fine-grained layers in northern Cascadia do not develop fractures. This is due to the combination of high permeability and low flow rate (e.g., Chapter 4). Hydrate accumulates steadily in the lowermost coarse-grained layer (Figure 6.6d) but causes almost no solubility increase (Figure 6.6e). This is due to the large pore size. Even with $S_h = 0.40$, the pore space remains large enough that the triple point depression is very small (~0.01% in the fine-grained layers), so the change in solubility is negligible.

6.5. Discussion

6.5.1 Maximum thickness for hydrate occurrence in fine-grained layers

In our model, methane hydrate forms from dissolved methane when the amount of methane dissolved in the pore fluid exceeds the solubility value; hydrate forms until the dissolved methane concentration is reduced to the solubility value. As a result, the pore fluid flowing through a coarse-grained layer will exit the top of the layer with a dissolved methane concentration equal to the solubility at the top of that layer. No hydrate should

form in the pores of the fine-grained layer immediately overlying the coarse-grained layer because the fine-grained layer has smaller pores and therefore higher methane solubility than the coarse-grained layer due to the Gibbs-Thomson effect. The dissolved methane concentration will therefore be constant through the fine-grained layer and equal the solubility at the top of the coarse-grained layer. However, methane solubility decreases upwards in the MHSZ because of the in situ temperature and pressure gradients. For sufficiently thick fine-grained layers, the solubility value may decrease enough over the thickness of the fine-grained layer to equal the dissolved methane concentration in the pore fluid. In this case, hydrate will form in the pores of the fine-grained layer in addition to the coarse-grained layer. The maximum thickness of a hydrate-free fine-grained layer is determined by the solubility gradient and the contrast in grain size between coarse and fine grains; larger grain size contrasts or smaller solubility gradients will allow thicker hydrate-free fine-grained layers.

In northern Cascadia, the solubility difference between the fine-grained and coarse-grained layers is 2.5×10^{-6} kg kg^{-1}, and the solubility gradient over the model domain is roughly 4.2×10^{-7} kg kg^{-1} m^{-1} (Figure 6.6b). Assuming the solubility can be approximated as a linear function of depth over small depth intervals, the maximum hydrate-free fine-grained layer thickness is 6.0 m ($= 2.5 \times 10^{-6}$ kg kg^{-1}/4.2×10^{-7} kg kg^{-1} m^{-1}). At Hydrate Ridge, the initial solubility difference between the fine-grained and the coarse-grained layers is 9.4×10^{-5} kg kg^{-1}, and the solubility gradient over the model domain is roughly 1.1×10^{-5} kg kg^{-1} m^{-1} (Figure 6.5b). The corresponding maximum fine-grained layer thickness is 8.5 m ($= 9.4 \times 10^{-5}$ kg kg^{-1}/1.1×10^{-5} kg kg^{-1} m^{-1}). These values represent maximum fine-grained layer thicknesses that will result in hydrate-free fine-

grained layers interbedded with hydrate-bearing coarse-grained layers. In both cases, the observed fine-grained layer thicknesses are less than the computed maximum, so hydrate is expected to be confined to coarse-grained layers, which is consistent with observations (Weinberger et al., 2005; Torres et al., 2008). In spite of the difference in grain-size contrast between Hydrate Ridge (30 µm to 0.5 µm) and northern Cascadia (80 µm to 16 µm), the larger solubility gradient at Hydrate Ridge restricts the fine-grained layer thickness, so the maximum hydrate-free fine-grained layer thickness at both sites is similar. The difference in solubility gradients between the sites is due mainly to the difference in seafloor depth. Although both sites have similar geothermal gradients, water pressure in the RHSZ is lower at Hydrate Ridge since the water depth is lower than at northern Cascadia, and the methane solubility gradient with temperature is larger at lower pressures (Duan et al., 1992). The fine-grained layer thickness limit is valid only for hydrate forming in pores. If fractures form in fine-grained layers, hydrate will be able to form in the fractures since we assume the fractures are large enough that the Gibbs-Thomson effect is negligible.

6.5.2 Conditions to create fractured fine-grained layers

Our results show that the fine-grained layers at Hydrate Ridge develop throughgoing fractures that act as conduits for fluid flow between coarse-grained layers, but that this does not occur at northern Cascadia. This is related to the permeability contrast between coarse and fine grains; the contrast is on the order of 1000 at Hydrate Ridge but only 10 at northern Cascadia. The conditions required to form fractures through fine-grained layers can be illustrated by considering a simple layered system

composed of n coarse-grained and n fine-grained layers each with equal thickness b.

From Equation 6.6, fractures will develop in any layer when

$$P^* \geq \lambda_c^* \sigma_{vh}',$$

(Equation 6.9)

where λ_c^* is the critical overpressure ratio given by $\dfrac{v}{1-v}$. P^* is given by

$$P^* = nb\left(\frac{dP^*}{dz}\bigg|_{coarse} + \frac{dP^*}{dz}\bigg|_{fine}\right).$$

(Equation 6.10)

If flux is constant across the system and hydrate exists only in the coarse-grained layers, Equation 6.10 can be expressed as

$$P^* = nb|\bar{q}_f|\mu_w\left(\frac{1}{k_c(1-S_h)^4} + \frac{1}{k_f}\right),$$

(Equation 6.11)

where k_c and k_f are the permeabilities of coarse-grained and fine-grained layers, and μ_w is the dynamic viscosity of seawater (8.87×10^{-4} Pa s at 25°C). Because $\rho_h \approx \rho_w$, the vertical effective stress can be approximated as

$$\sigma_{vh}' = nbg\left(\rho_g\left((1-\varphi_c) + (1-\varphi_f)\right) + \rho_w\left(\varphi_c + \varphi_f\right)\right),$$

(Equation 6.12)

where φ_c and φ_f are the porosities of coarse-grained and fine-grained layers, and ρ_g is the sediment grain density [kg m^{-3}]. Combining Equations 6.9, 6.11, and 6.12 gives the criterion for fracturing through the fine-grained layers:

$$|\vec{q}_f| \mu_w \left(\frac{1}{k_c(1-S_h)^4} + \frac{1}{k_f} \right) \geq \lambda_c^* g \left[\rho_g \left((1-\varphi_c) + (1-\varphi_f) \right) + \rho_w (\varphi_c + \varphi_f) \right].$$ (Equation 6.13)

Assuming $\varphi_c + \varphi_f \approx 1$, which is valid in shallow sediments where $\varphi_c \approx \varphi_f \approx 0.5$, Equation 6.13 reduces to

$$\frac{1}{k_c(1-S_h)^4} + \frac{1}{k_f} \geq \frac{\lambda_c^* g (\rho_g + \rho_w)}{|\vec{q}_f| \mu_w}.$$ (Equation 6.14)

Equation 6.14 illustrates that, for a given coarse-grained layer permeability and hydrate saturation, the maximum fine-grained layer permeability at which throughgoing fractures will form increases with increasing flow rate.

The difference in fracturing behavior between Hydrate Ridge and northern Cascadia can be illustrated by Equation 6.14 (Figure 6.7); we assume $\rho_g = 2700$ kg m^{-3} and $\lambda_c^* = 0.67$, which corresponds to $v = 0.4$. The diagonal line in Figure 6.7 represents values for which the two sides of Equation 6.14 are equal. The area above this line represents situations that permit fracturing through fine-grained layers, and the area below this line represents values where fracturing is not possible. At Hydrate Ridge, the flow rate is 430 mm yr^{-1}, $k_c = 6 \times 10^{-13}$ m^2, $k_f = 2 \times 10^{-16}$ m^2, and $S_h = 0.90$ in the coarse-
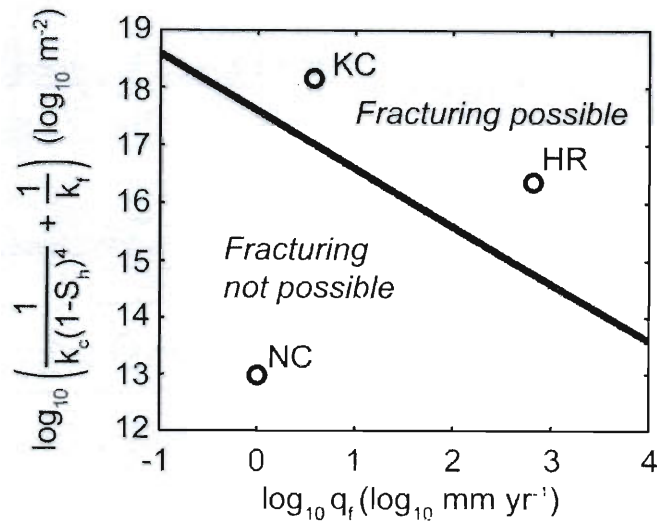
Figure 6.7 Plot of rate of fluid flow versus the left-hand side of Equation 6.14 assuming $\rho_g = 2700$ kg m^{-3} and $\lambda_c^* = 0.67$. Points that plot in the area below this line correspond to environments where pore pressure buildup is insufficient to induce fracturing; points that plot above the line correspond to environments where fracturing is possible. Hydrate Ridge (HR) plots in the region of possible fracturing, while northern Cascadia (NC) plots in the region of no fracturing. Keathley Canyon Block 151 (KC), a site where fracture generation is interpreted to be occurring at the present day, plots in the region of possible fracturing.

grained layers based on our simulation. These values place Hydrate Ridge in the area where fracturing is possible in the fine-grained layers (Figure 6.7). For northern Cascadia, assuming the upper flow rate limit of 1 mm yr^{-1} (Malinverno et al., 2008), $k_c = 4 \times 10^{-12}$ m^2, $k_f = 2 \times 10^{-13}$ m^2, and $S_h = 0.40$ in the coarse-grained layers (Torres et al., 2008) results in the site plotting where fracturing is not possible (Figure 6.7). The lack of fracturing at northern Cascadia is due to a combination of high permeability and low flow rate. With the observed permeability values, the flow rate would need to be in excess of 1000 mm yr^{-1} for fractures to form through the fine-grained layers. These two sites are examples of how interactions between fluid migration and sediment physical properties

affect hydrate formation patterns and create the potential for subsequent fracturing that focuses fluid transport through low permeability layers.

To illustrate the validity of the criterion expressed by Equation 6.14, we examine Keathley Canyon Block 151 (KC151), a site in the northern Gulf of Mexico where fracture-hosted hydrate has been observed in a fine-grained interval (Hutchinson et al., 2008; Cook et al., 2008). Fluid advection rates at KC151 are estimated at 4-28 mm yr^{-1} (Dugan, 2008) and the sediments in the fractured interval (220-300 mbsf) are uniform with permeability of 10^{-18} m^2 (Chapter 2). On the basis of fluid flow rates and permeability measurements, fracture generation is interpreted to be active at this site (Chapter 4). Assuming $k_c = k_f = 10^{-18}$ m^2 and a flow rate of 4 mm yr^{-1}, KC151 plots in the region where fracturing is possible (Figure 6.7), which illustrates that the predictions from Equation 6.14 match observed behavior at a site with well-constrained physical properties.

6.5.3 Capillary-driven solubility increase and cessation of hydrate formation

In our model, methane solubility in the coarse-grained layers increases as hydrate formation decreases the pore radius. Eventually, enough hydrate will form that the methane solubility (the maximum amount of methane that the water can maintain in the dissolved phase) increases beyond the methane concentration dissolved in the pore fluid. At this point, hydrate formation will cease. Before reaching this point, however, the overpressure ratio may increase enough to fracture through the intervening fine-grained layers. Whether fracturing occurs prior to capillary-driven cessation of hydrate formation

is a function of the relative rates of excess pore pressure buildup and methane solubility increase.

The conditions for fracturing prior to cessation of hydrate formation can be expressed as (see Appendix F)

$$\frac{\lambda_c^{\cdot} g\left(\rho_g + \rho_w\right)}{2\left|\vec{\mathbf{q}}_f\right|\mu_w} < \left(\frac{1}{k_c} + \frac{1}{k_f}\right)\left(\frac{\left(x_{m,c}^l - x_{m,0}^l\right)}{\dfrac{\partial x_m^l}{\partial S_h}} + \frac{1}{2}\right)$$

(Equation 6.15)

where $x_{m,0}^l$ and $x_{m,c}^l$ are the initial solubility and critical solubility to stop hydrate formation (i.e., the dissolved methane concentration in the pore fluid), and $\partial x_m^l / \partial S_h$ is the change in methane solubility with hydrate saturation due to the Gibbs-Thomson effect. Equation 6.15 is expressed in terms of flow rate, fracture criterion, permeability, and solubility, which is influenced by pressure, temperature, and pore size. To assess hydrate formation behavior at any site, it is necessary to determine $x_{m,c}^l - x_{m,0}^l$ and $\partial x_m^l / \partial S_h$. We consider the behavior of the lowermost coarse-grained layer for northern Cascadia and Hydrate Ridge. Since the lower boundary condition on dissolved methane concentration is equal to the solubility in a coarse-grained layer situated just below the base of the domain, capillary-driven shutdown will occur in the lowermost coarse-grained layer when the solubility increases to this value. At Hydrate Ridge, the difference between the incoming methane concentration and solubility in the lowermost coarse-grained layer is 1.33×10^{-5} kg kg^{-1}; at northern Cascadia, this quantity is 1.05×10^{-6} kg kg^{-1}. $\partial x_m^l / \partial S_h$ can
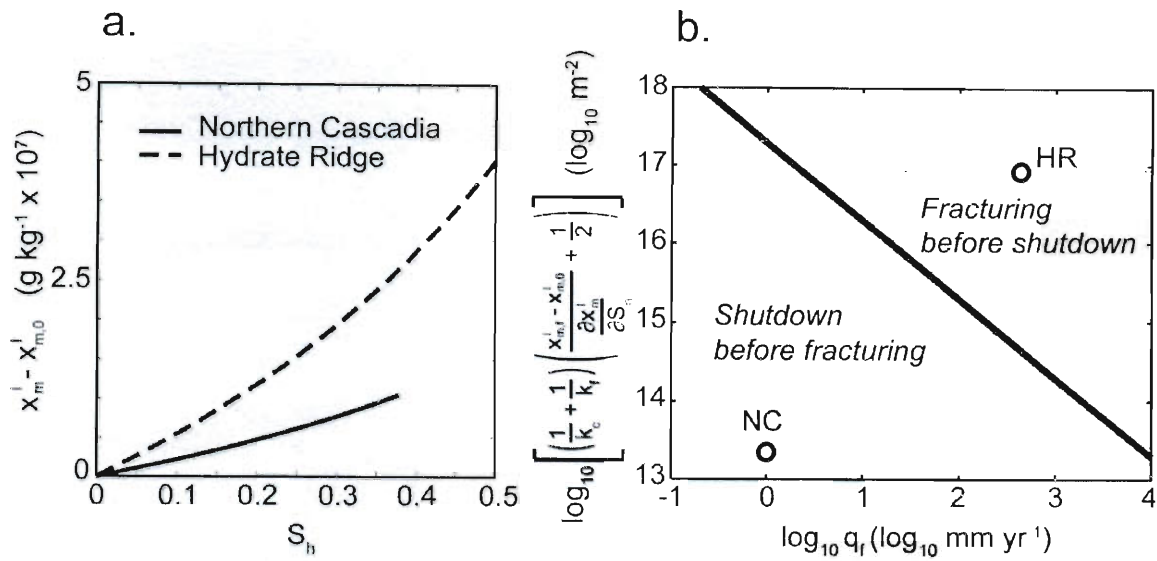
Figure 6.8 (a) Increase in methane solubility versus hydrate saturation for Hydrate Ridge and northern Cascadia. Methane solubility is referenced to the initial solubility when S_h = 0. Northern Cascadia experiences a smaller change in solubility at a given hydrate saturation because this site has coarser-grained sediments and correspondingly larger pores than Hydrate Ridge. (b) Flow rate versus the right-hand side of Equation 6.15 assuming ρ_g = 2700 kg m^{-3} and $\lambda_c{}^*$ = 0.67. Note that flow rate is inversely proportional to the left-hand side of Equation 6.15. Diagonal line represents values for which the two sides of Equation 6.15 are equal. Points that plot in the region below this line will experience shutdown of hydrate formation due to solubility increase before fractures form; points that plot in the region above this line will experience fracturing prior to shutdown. Northern Cascadia (NC) plots in the region of shutdown, while Hydrate Ridge (HR) plots in the region of fracturing. Fracturing will be favored over shutdown of hydrate formation at high flow rates or in fine-grained sediments where permeability is low and the change in solubility with hydrate saturation is high.

be approximated as a constant value by fitting a line to the solubility and hydrate

saturation data (Figure 6.8a); at Hydrate Ridge, this value is 8.2×10^{-7} kg kg^{-1}, and at

northern Cascadia this value is 2.8×10^{-7} kg kg^{-1}. The difference in this value between the

two sites is related to the finer-grained sediments at Hydrate Ridge, since a given increase

in the fraction of the pore occupied by hydrate reduces the pore size more than in coarser-

grained sediments. We use these values to plot the two sites on a graph of flow rate

versus the quantity on the right-hand side of Equation 6.15 (Figure 6.8b). Note that flow

rate is inversely proportional to the left-hand side of Equation 6.15. The diagonal line on

the plot represents values for which the left- and right-hand sides of Equation 6.15 are

equal, and divides the plot into areas of capillary-driven shutdown and fracturing. For

points above the line, the right-hand side of Equation 6.15 is greater, so fracturing will

occur. For points below the line, the left-hand side of Equation 6.15 is greater, so hydrate

formation will shut down. Hydrate Ridge plots in the fracture area as expected since

fracturing was observed during simulation. Northern Cascadia plots in the capillary-

driven shutdown area. We showed that the flow rate at this site is too low to produce

fractured fine-grained layers, and here we illustrate that hydrate formation will eventually

cease as hydrate accumulates in the coarse-grained layers and drives solubility up to the

local dissolved methane concentration.

6.5.4 Development of observed features

At Hydrate Ridge, we predict that coarse-grained layers will be connected by

fractured fine-grained layers after ~10,000 years, with $S_h \approx 0.90$ in the coarse-grained

layers. The time required to develop these features is consistent with interpretations of the

current MHSZ configuration having evolved after the last glacial maximum (Bangs et al.,

2005). The hydrate saturations we compute, however, are considerably higher than the

values of 0.10-0.15 inferred from acoustic logs (Lee and Collett, 2006) and porewater

chlorinity data (Shipboard Scientific Party, 2003). However, thin, hydrate-filled layers

present problems in log analysis (e.g., Cook, 2010), and it is possible that thin coarse-

grained layers may have been missed in these analyses due to sampling bias or tool

resolution. For instance, the 25 cm-thick coarse-grained layers we model would not be resolved in the dipole sonic logs from Hydrate Ridge, which have a nominal vertical resolution of ~1 m (Schlumberger Limited, 2004). The log response would be an average of the layers within the 1 m resolution, so thin layers would give the same response as thicker layers with lower hydrate saturation and result in an underestimation of hydrate volume present. Another factor influencing our S_h estimates is our assumption of steady-state fluid flow. The hydrate saturation required to decrease permeability to the point where hydraulic fractures form decreases as the rate of fluid flow increases. Thus, a transient episode of rapid fluid flux could potentially cause hydraulic fracturing at relatively low S_h. Measurements of fluid flow and 4-D seismic analysis have shown that fluid migration pathways and fluxes are highly variable on time scales from days to years at Hydrate Ridge (Tryon et al., 2002; Bangs et al., 2009) and northern Cascadia (Riedel, 2007). Our overestimation of S_h at Hydrate Ridge therefore may suggest that transient fluid flow pulses are important in determining hydrate and fracture distribution, and that the observed features may have developed rapidly during one or several such episodes.

At northern Cascadia, our model required 2×10^5 years of fluid flux to match the observed hydrate saturation in the coarse-grained layers, and no fractures are predicted to form, which matches observations from image logs. The sediments at this site are generally older than 3×10^5 years, with the exception of the shallowest 50 m (Riedel et al., 2006), so time scale is not unreasonable. However, it is probably unreasonable to assume steady state conditions for 2×10^5 years, especially considering the location in an active convergent margin. The main factor controlling the time required for hydrate accumulation is the rate of fluid flow. Since we assume that the only source of methane is

in the pore water flux, hydrate growth is limited by the rate of advective methane supply. Malinverno (2010) modeled hydrate saturations that matched observed values after a few hundred years by including in situ biogenic methane production in the fine-grained layers. In situ production is inferred throughout the RHSZ at Site U1325 based on the trend of total organic carbon content decreasing steeply with depth (Riedel et al., 2006) and enriched $\delta^{13}C$ values of residual dissolved inorganic carbon (Torres and Kastner, 2009). This must represent an important source of methane at this site. The low rates of vertical fluid flow can easily be accommodated by porous medium flow due to the high permeability of the fine-grained layers relative to that at Hydrate Ridge.

6.6. Conclusions

We considered changes in three-phase equilibrium temperature and solubility due to the Gibbs-Thomson effect in a 1-D model of hydrate formation from methane supplied by pore fluid advection. We applied this model to Hydrate Ridge and northern Cascadia, two field sites where hydrate has been observed preferentially in thin, coarser-grained layers in the sedimentary column. In both cases, increased solubility in the fine-grained layers is sufficient to inhibit hydrate formation in the fine-grained layers, resulting in hydrate formation only in the coarse-grained layers. However, 2×10^5 years are required at northern Cascadia to generate the observed hydrate saturations due to low fluid advection rates. We conclude that hydrate formation at this site is enhanced by in situ production of biogenic methane in the fine-grained layers, which is then transported into the coarse-grained layers by diffusive flux as modeled by Malinverno (2010). At Hydrate Ridge, advective methane transport is rapid enough to fill the coarse-grained layers almost

completely with hydrate after 10,000 years, a reasonable time scale given constraints on sediment age (Chevallier et al., 2006) and the age of the current configuration of the hydrate stability zone (Bangs et al., 2005). Our predicted hydrate saturations are significantly higher than saturations inferred from log and porewater chlorinity data, but this may be due to the spatial resolution of tools or transient fluid pulses that allow fractures to form at lower S_h. Development of fractures in the fine-grained layers limits hydrate formation in the coarse-grained layers by allowing hydrate to form in the fractures, thus removing dissolved methane from the water exiting the fractured fine-grained layers. Fractures develop through the fine-grained layers at Hydrate Ridge, but no fractures develop at northern Cascadia; this difference in behavior is driven by contrasts in permeability and flow rate between the two sites.

Permeability, grain size, layer thickness, and solubility gradient influence the behavior of layered systems through time, and control the final distribution of hydrate. Hydrate-free fine-grained layers are only possible if the fine-grained layers are thinner than a maximum thickness dictated by the solubility contrast with the coarse-grained layers and the solubility gradient through the fine-grained layers. Fractures will develop through the fine-grained layers if the flow rate is high enough or the permeability of the fine-grained layer is low enough. Capillary-driven shutdown of hydrate formation may occur if enough hydrate forms in the coarse-grained layer to occlude the pore throats and increase the solubility beyond the concentration supplied in the pore fluid; this process will occur primarily in sediments with high permeability and low flow rate in which fractures do not form first. These examples illustrate the complicated feedbacks among sediment physical properties, environmental conditions, and hydrate formation, showing

how phenomena at small length and time scales like the Gibbs-Thomson effect and transient fluid fluxes are critical factors in creating observed hydrate saturation and distribution. Our work helps advance our understanding of these feedbacks and our general understanding of factors that control hydrate accumulation and distribution.

7. General Conclusions and Future Work

<u>7.1 Conclusions</u>

In this thesis I have presented results that demonstrate the influence that pore-scale properties and processes have on macroscale behavior in fine-grained sediments. I have focused specifically on NMR permeability and methane hydrate systems, but the conclusions may be applied outside these areas to fine-grained sediments in general. Here I summarize my conclusions in three categories.

7.1.1 Permeability and NMR response

Existing methods of determining permeability from NMR data are extended to fine-grained sediments by applying a correction factor that accounts for the high surface area and paramagnetic ion abundance that is typical of clays. This correction factor can be computed from quantities that are easily measured in the laboratory, and allows for improved permeability estimation over 4 orders of magnitude. The algorithm for computing the correction factor is developed by assuming that permeability can be described accurately by the Kozeny model, and by considering how grain size and shape influence specific surface and tortuosity, the key parameters in the Kozeny equation. Additionally, the NMR response to clays with high concentrations of paramagnetic ions on their surfaces can be corrected using the magnetic susceptibility. The development of this correction factor highlights yields the important conclusion that the pore system of fine-grained sediments can be described by the Kozeny model to permeabilities as low as 10^{-18} m^2.

Invoking Kozeny's model to describe the pore system of fine-grained sediments has implications beyond NMR permeability calculations. Kozeny theory states that the permeability of a porous medium is a function of the pore surface area exposed to flow, and the shape and tortuosity of flow paths. My NMR work shows one example of an instance in which an assumption of pore geometry, in this case that the deflection of flow paths around platy grains can be computed by assuming a particular grain shape, can be used to make predictions about permeability behavior. In a similar way, Kozeny theory could be invoked to explain changes in transport properties that occur during primary consolidation of mudstones, and how heterogeneities in grain size and shape affect transport properties in fine-grained sediments. This represents a powerful technique in research related to transport properties of mudstones and low-permeability rocks.

7.1.2 Methane hydrate distribution

Microstructural properties affect methane hydrate distribution by influencing pore pressure buildup and methane equilibrium conditions. The pore pressure effects are related to the effect of permeability on fluid flux and methane availability within the regional hydrate stability zone (RHSZ). In Chapter 4, I showed that the feasibility of hydraulic fracturing due to pore system occlusion in constant-flux settings depends on sediment permeability and fluid flux. If permeability is low and/or flux is high, less hydrate is required to occlude the pore space to the point where hydraulic fractures will form. Thus the permeability directly affects how much hydrate will form in the pore space prior to hydraulic fracturing. A similar conclusion can be reached from the multiphase flow results presented in Chapter 5, although in the multiphase flow model I

considered fracturing by capillary pressure of the gas phase. Fracturing occurs when hydrate constricts the pores to the point at which the capillary pressure of the gas phase exceeds the overburden stress. Sediments with high initial permeability and thus larger initial pore sizes will require greater amounts of hydrate to form to constrict the pores sufficiently to meet the fracture criterion. Thus, as in the constant flux model from Chapter 4, high-permeability sediments will generally support higher hydrate saturations within the sediment pore space. In both models, hydrate is predicted to form primarily in fractures in low-permeability sediments since the fracture criterion may be reached at low hydrate saturation.

In Chapter 6 I showed how the Gibbs-Thomson effect leads to depression of the three-phase equilibrium temperature of methane in small pores, resulting in an increase in methane solubility in sediments with small pores. This causes hydrate to nucleate preferentially in coarse-grained sediments since the pore fluid can hold less methane in solution. In layered sediments featuring alternating beds of fine- and coarse-grained sediment, it is possible for hydrate to form exclusively in the coarse-grained layers if the fine-grained layers are thinner than a maximum thickness that is a function of the pore-size contrast between the coarse- and fine-grained layers as well as the spatial gradient of the solubility curve. Settings with a large contrast in pore size between fine- and coarse-grained layers will generally be able to support thicker hydrate-free, fine-grained layers.

My work thus shows how pore structure affects hydrate distribution by influencing methane supply pathways and changing local thermodynamic conditions. These results depend to some extent on the assumptions made in modeling hydrate growth in the pore system, since pore system geometry and hydrate growth habit dictate

the relationships among hydrate saturation, permeability, capillary pressure, and three-phase equilibrium temperature. However, as I showed in Chapters 5 and 6, these assumptions affect the particular hydrate saturation that corresponds to a particular reduction in permeability or increase in capillary pressure, but not the overall results. Thus, these results are not dependent on a particular assumption of pore geometry in the way that the NMR results are.

7.1.3 Fracturing behavior in hydrate systems

The initial sediment pore size or permeability along with the flux of methane into the sediment determine fracturing behavior. From Chapter 4, sediments with low initial permeability and/or high water flux will fracture after shorter times and lower hydrate saturation. In homogeneous sediments, fractures nucleate at the base of the RHSZ, but low-permeability layers can cause fractures to nucleate in the middle of the RSHZ if the layers are sufficiently thick and have a sufficient permeability contrast with the surrounding sediment. In the case of multiphase methane supply (methane gas and dissolved methane) as in Chapter 5, the relative fluxes of gas and methane-charged water determine where fractures nucleate. Water-dominated systems will behave like those in Chapter 4, with fractures nucleating at the base of the RHSZ, while gas-dominated systems will experience fracture nucleation high within the RHSZ at the top of the gas column that has invaded the RHSZ. In all these cases, the microstructural properties of the sediment determine how much hydrate is required to reach the fracture criterion.

In Chapter 6, I show that hydrate nucleation in coarse-grained layers may cause fracturing through intervening fine-grained layers if the contrast in pore size between the

fine- and coarse-grained layers is sufficiently large. However, in this model as hydrate forms, the pore space is constricted, depressing the three-phase equilibrium temperature and possibly inhibiting further hydrate nucleation. Therefore, fracturing in the fine-grained layers may only occur if hydrate nucleation does not shut down in the coarse-grained layers before the fracture criterion is met. In this case, the initial pore size determines not only how much hydrate is required to reach the fracture criterion, but also whether fracturing will occur prior to cessation of hydrate formation. This is a good example of an interaction between transport and thermodynamic properties that depends largely on microstructural sediment properties and affects macroscale behavior.

My work on fracturing behavior in methane hydrate systems thus illustrates how pore-scale processes in fine-grained sediments can largely determine the macroscale behavior of these systems. These results can be extended to other problems involving chemical transport in porous media, such as cement precipitation, overpressure generation due to diagenetic reactions, carbon sequestration, and hydrocarbon migration.

7.2 Future work

7.2.1 NMR permeability

While the work presented in Chapter 3 serves to explain the mechanisms responsible for the correlation between A and gamma ray observed in Chapter 2, the result still includes the empirical constants α and β. These variables clearly vary in some systematic way related to mineralogy and pore shape, but characterizing this variation was beyond the scope of my work. To characterize the variation properly, a future study would need to determine how ρ_2 varies with magnetic susceptibility for a variety of

carefully controlled mineralogies. The pore shape factor v is not expected to vary significantly, but this hypothesis would need to be tested as well by comparing results with different grain sizes and shapes. This future work would help illuminate the fundamental processes responsible for the variation in α and β, and would allow the results of Chapter 3 to be generalized to a wider range of rock types.

7.2.2 Microstructural evolution

In Chapter 3 I showed that tortuosity could be related to grain size and surface area, and that predictions about pore system structure could be made by considering a simple representative model of flow paths around grains. This method considers the sediment matrix as a static system with no change in pore geometry over time. However, sediments in basins are generally buried and subjected to increasing vertical effective stresses, resulting in consolidation and loss of pore volume. This leads to a decrease in permeability with increasing vertical effective stress. Following the theory of March (1932), platy clay grains in the sediment matrix will rotate during primary consolidation so that their long axes become perpendicular to the maximum principal stress. This will impart a preferred clay-grain fabric to the sediment, which can be related to tortuosity and permeability using assumptions of grain geometry similar to those presented in Chapter 3. Future work needs to be done to determine if the assumptions made in Chapter 3 regarding grain geometry and tortuosity can accurately characterize pore system evolution during primary consolidation of mudstones. This work could be conducted by measuring permeability of consolidated laboratory mixtures of clays with known grain size and shape and comparing the results with model predictions. Ultimately this work

would advance our understanding of the pore system of mudstones, and how transport properties evolve in natural settings.

7.2.3 Fracture propagation in unconsolidated sediments

A key assumption in the models of Chapters 4 and 5 is that fractures propagate very rapidly once they form. Rapid fracture propagation (tens of meters over time scales of seconds to minutes) is supported by theoretical calculations (Valkó and Economides, 1995). However, in my models, this requires that the entire sediment column above the fracture nucleation point be at the fracture criterion, so that fracturing will continue once it is initiated. Accurate modeling of this phenomenon requires more sophistication than can be captured in a finite-difference scheme. Further work with finite element models (e.g., Jain and Juanes, 2009) or boundary element models (e.g., Lovely et al., 2009) could easily include fracture propagation in an elastic medium, and provide constraints on the time and conditions required for fracture propagation as well as the local stresses that arise in the sediments surrounding the fracture.

7.2.4 Advanced modeling

Chapters 4, 5, and 6 are all based on one-dimensional models. Such dimensional restriction is often a reasonable approximation, as in the case where fluid flow is dominantly vertical and horizontal gradients in physical properties are negligible. However, this is generally not the case. By neglecting lateral heat, fluid, and solute transport in our models, we can easily capture generalized behavior, but do not capture full field-scale behavior. For instance, the model in Chapter 5 assumes that once excess

salt is produced by hydrate formation, it remains in place. If we were to consider more than one dimension, the excess salt produced locally would create a concentration gradient, which would drive diffusive flux of salt away from the site of hydrate formation, in turn affecting the equilibrium conditions required for gas to be present. Liu and Flemings (2007) show in their two-dimensional model that any salt that is lost to diffusive flux will be replenished by additional hydrate formation, thus maintaining three-phase equilibrium conditions. However, this situation requires that salt be produced as rapidly as it is diffused away, which depends on the rate of methane supply to form hydrate. This example serves to show the drawbacks of one-dimensional simulations and the potential complications that arise when more than one dimension is considered.

More sophisticated models of hydrate formation and fracture generation, then, should increase the number of spatial dimensions. This in turn will introduce additional complications not present in one-dimensional models, but will give a more accurate representation of natural settings. Additional dimensions will also allow for greater flexibility in introducing sedimentation, changing fluxes over time, and allowing sediment physical properties to vary. This will be of particular value for understanding field sites that may have undergone significant deformation and dynamics in the past, such as Blake Ridge and NGHP Site 10. As the ultimate goal of modeling work is to understand how processes work in natural settings, making the model more realistic will only serve to improve model results.

Bibliography

Anderson, R., Llamedo, M., Tohidi, B., Burgass, R.W., 2003a. Experimental measurement of methane and carbon dioxide clathrate hydrate equilibria in mesoporous silica. *Journal of Physical Chemistry B*, 107(15), 3507-3514, doi:10.1021/jp0263370.

Anderson, R., Llamedo, M., Tohidi, B., Burgass, R.W., 2003b. Characteristics of clathrate hydrate equilibria in mesopores and interpretation of experimental data. *Journal of Physical Chemistry B*, 107(15), 3506-3509, doi:10.1021/jp0263368.

Anderson, R., Tohidi, B., Webber, J.B.W., 2009. Gas hydrate growth and dissociation in narrow pore networks: Capillary inhibition and hysteresis phenomena. In: D. Long, et al. (Editors), *Sediment-Hosted Gas Hydrates: New Insights on Natural and Synthetic Systems*, *Geological Society of London Special Publications Series*, 319. The Geological Society, London, pp. 145-159.

Alvarado, R.J., Damgaard, A., Hansen, P., Raven, M., Heidler, R., Hoshun, R., Kovats, J., Morriss, C., Rose, D., Wendt, W., 2003. Nuclear magnetic resonance logging while drilling. *Oilfield Review*, 15(2), 40-51.

Archer, D., Buffett, B., 2005. Time-dependent response of the global ocean clathrate reservoir to climatic and anthropogenic forcing. *Geochemistry, Geophysics, Geosystems*, 6(3), Q03002 doi:10.1029/2004GC000854.

Arns, C.H., Knackstedt, M.A., Martys, N.S., 2005. Cross-property correlations and permeability estimation in sandstone. *Physical Review E*, 72(4), 046304, doi:10:1103/PhysRevE.72.046304.

ASTM International, 2003. *Standard Test Method for Particle-Size Analysis of Soils.* D422-63.

ASTM International, 2004. *Standard Test Methods for Measurement of Hydraulic Conductivity of Saturated Porous Materials Using a Flexible Wall Permeameter.* D5084-03.

ASTM International, 2006. *Standard Test Method for One-Dimensional Consolidation Properties of Saturated Cohesive Soils Using Controlled-Strain Loading.* D4186-06.

Athy, L.F., 1930. Density, porosity, and compaction of sedimentary rocks. *AAPG Bulletin*, 14(1), 1-24.

Bachir, C., 2009. *The Influence of Calcination Temperature on Structure and Magnetic Properties of Pillared Clays*. PhD thesis, Universität Fridericiana zu Karlsruhe, Karlsruhe, Germany, 143 pp.

Baker, J.C., Uwins, P.J.R., Mackinnon, I.D.R., 1993. ESEM study of illite/smectite freshwater sensitivity in sandstone reservoirs. *Journal of Petroleum Science and Engineering*, 9(2), 83-94, doi:10.1016/0920-4105(93)90069-Q.

Banavar, J.R., Schwartz, L.M., 1987. Magnetic resonance as a probe of permeability in porous media. *Physical Review Letters*, 58(14), 1411-1414.

Bangs, N.L., Hornbach, M., Berndt, C., 2009. Rapid, episodic gas migration into the South Hydrate Ridge gas hydrate field inferred from 4D seismic imaging. *Eos Transactions of the American Geophysical Union*, 90(52), Fall Meeting Supplement, Abstract OS23B-07.

Bangs, N. L., Musgrave, R.L., Tréhu, A.M., 2005. Upward shifts in the southern Hydrate Ridge gas hydrate stability zone following postglacial warming, offshore Oregon. *Journal of Geophysical Research*, 110, B03102, doi:10.1029/2004JB003293.

Bear, J., 1972. *Dynamics of Fluids in Porous Media*. New York: Elsevier, 764 pp.

Behrmann, J. H., 1991. Conditions for hydrofracture and the fluid permeability of accretionary wedges. *Earth and Planetary Science Letters*, 107, 550–558, doi:10.1016/0012-821X(91)90100-V.

Behseresht, J., 2008. *Infinite-Acting Physically Representative Networks for Capillarity-Controlled Displacements*. M.S. thesis, Department of Petroleum and Geosystems Engineering, University of Texas, Austin, TX, USA, 150 pp.

Bekins, B.A., Dreiss, S.J., 1992. A simplified analysis of parameters controlling dewatering in accretionary prisms. *Earth and Planetary Science Letters*, 109, 275-287.

Berge, L.I., Jacobsen, K.A., Solstad, A., 1999. Measured acoustic wave velocities of R11 (CCl_3F) hydrate samples with and without sand as a function of hydrate concentration. *Journal of Geophysical Research*, 104(B7), 15415-15424.

Bernabe, Y., Brace, W.F., 1990. Deformation and fracture of Berea sandstone, In: Duba, A.G., et al. (Editors), *The Brittle-Ductile Transition in Rocks: The Heard Volume, Geophysical Mongraph Series*, 56. American Geophysical Union, Washington, DC, pp. 91-102.

Berryman, J.G., Blair, S.C., 1986. Use of digital image analysis to estimate fluid permeability of porous materials: Application of two-point correlation functions. *Journal of Applied Physics*, 60(6), 1930-1938, doi:10.1063/1.337245.

Bhatnagar, G., Chapman, W.G., Dickens, G.R., Dugan, B., Hirasaki, G.J., 2007. Generalization of gas hydrate distribution and saturation in marine sediments by scaling of thermodynamic and transport processes. *American Journal of Science*, 307, 861–900, doi:10.2475/06.2007.01

Bird, R. B., Stewart, W.E., Lightfoot, E.N., 2007. *Transport Phenomena*, 2nd ed. New York: John Wiley, 905 pp.

Boswell, R., Collett, T.S., McConnell, D., Frye, M., Shedd, W., Mrozewski, S., Guerin, G., Cook, A., Shelander, D., Dai, J., Godfriaux, P., Dufrene, R., Jones, E., Roy, R., 2010. Gulf of Mexico Gas Hydrates Joint Industry Project: Overview of Leg II LWD results. Paper presented at 2010 Offshore Technology Conference, Houston, TX, 5 May 2010.

Boudreau, B., 1996. The diffusive tortuosity of fine-grained unlithified sediments. *Geochimica et Cosmichimica Acta*, 60(16), 3139-3142.

Brun, M., Lallemand, A., Quinson, J.-F., Eyraud, C., 1977. A new method for the simultaneous determination of the size and shape of pores: The thermoporometry. *Thermochimica Acta*, 21(1), 59-88, doi:10.1016/0040-6031(77)85122-8.

Bryant, S.L., King, P.R., Mellor, D.W., 1993a. Network model evaluation of permeability and spatial correlation in a real random sphere packing. *Transport in Porous Media*, 11, 53-70.

Bryant, S.L., Mellor, D.W., Cade, C.A., 1993b. Physically representative network models of transport in porous media. *AIChE Journal*, 39(3), 387-396.

Carman, P.C., 1937. Flow through a granular bed. *Transactions of the Institution for Chemical Engineers, London*, 15, 150-156.

Caruso, L., Simmons, G., Wilkens, R., 1985. The physical properties of a set of sandstones - Part I. The samples. *International Journal of Rock Mechanics and Mining Sciences and Geomechanics Abstracts*, 22(6), 381-392.

Chauveteau, G., Nabzar, L., El Attar, Y., Jacquin, C., 1996. Pore structure and hydrodynamics in sandstones. Paper presented at 1996 International Symposium, paper SCA-9607, Society of Core Analysts, Montpellier, France, 8-10 September 1996.

Chevallier, J., Tréhu, A.M., Bangs, N.L., Johnson, J.E., Meyer, H.J., 2006. Seismic sequence stratigraphy and tectonic evolution of southern Hydrate Ridge. *Proceedings of the Ocean Drilling Program, Scientific Results*, 204, 1–29, doi:10.2973/odp.proc.sr.204.121.2006.

Claypool, G. (Editor), 2006. *Cruise Report: The Gulf of Mexico Gas Hydrate Joint Industry Project*. Morgantown, WV: National Energy Technology Laboratory, 196 pp., http://www.netl.doe.gov/technologies/oil-gas/publications/Hydrates/reports/GOMJIPCruise05.pdf.

Claypool, G. E., Milkov, A.V., Lee, Y.-J., Torres, M.E., Borowski, W.S., Tomaru, H., 2006. Microbial methane generation and gas transport in shallow sediments of an accretionary complex, southern Hydrate Ridge (ODP Leg 204), offshore Oregon, USA. *Proceedings of the Ocean Drilling Program, Scientific Results*, 204, 1–52, doi:10.2973/odp.proc.sr.204.113.2006.

Clennell, M.B., Hovland, M., Booth, J.S., Henry, P., Winters, W.J., 1999. Formation of natural gas hydrates in marine sediments 1. Conceptual model of gas hydrate growth conditioned by host sediment properties. *Journal of Geophysical Research*, 104(B10), 22985-23003.

Coelho, D., Thovert, J.-F., Adler, P.M., 1997. Geometrical and transport properties of random packings of spheres and aspherical particles. *Physical Review E*, 55(2), 1959-1978.

Collett, T.S., 1992. Potential of gas hydrates outlined. *Oil and Gas Journal*, 90(25), 84-87.

Collett, T.S., Ladd, J., 2000. Detection of gas hydrate with downhole logs and assessment of gas hydrate concentrations (saturations) and gas volumes on the Blake Ridge with electrical resistivity data. *Proceedings of the Ocean Drilling Program, Scientific Results*, 164, 179-191, doi:10.2973/odp.proc.sr.164.219.2000.

Collett, T. S., et al., 2007. Results of the Indian National Gas Hydrate Program Expedition 01 initial reports, report, Director General of Hydrocarbons, Ministry of Petroleum and Natural Gas, New Delhi.

Cook, A.E., 2010. Gas hydrate-filled fracture reservoirs on continental margins. Ph.D. thesis, Department of Earth and Environmental Sciences, Columbia University, New York, NY, USA, 198 pp.

Cook, A.E., Goldberg, D., Kleinberg, R.L., 2008. Fracture-controlled gas hydrate systems in the northern Gulf of Mexico. *Marine and Petroleum Geology*, 25(9), 932-941, doi:10.1016/j.marpetgeo.2008.01.013.

Costa, A., 2006. Permeability-porosity relationship: A reexamination of the Kozeny-Carman equation based on a fractal pore-space geometry assumption. *Geophysical Research Letters*, 33, L02318, doi:10.1029/2005GL025134.

Crutchley, G.J., Geiger, S., Pecher, I.A., Gorman, A.R., Zhu, H., Henrys, S.A., 2010. The potential influence of shallow gas and gas hydrates on sea floor erosion of Rock Garden, an uplifted ridge offshore New Zealand. *Geo-Marine Letters*, doi:10.1007/s00367-010-0186-y.

Dahlin, D.C., Rule, A.R., 1993. *Magnetic Susceptibility of Minerals in High Magnetic Fields* (US Bureau of Mines Report of Investigations 9449). Washington, DC: U.S. Government Printing Office, 18 pp.

Dai, S., Lee, C., Santamarina, J.C., in press. Formation history and physical properties of sediments from the Mount Elbert gas hydrate stratigraphic test well, Alaska North Slope. *Marine and Petroleum Geology*, doi:10.1016/j.marpetgeo.2010.03.005.

Dashen, R., Day, P., Kenyon, W., Straley, C., Willemsen, J., 1987. T_1-permeability correlations. *AIP Conference Proceedings*, 154, 37-62, doi:10.1063/1.36384.

Davie, M.K., Buffett, B.A., 2001. A numerical model for the formation of gas hydrate below the seafloor. *Journal of Geophysical Research*, 106(B1), 497-514.

Day, R.W., 1992. Effective cohesion for compacted clay. *Journal of Geotechnical Engineering*, 118(4), 611-619.

Dewhurst, D.N., Aplin, A.C., Sarda, J.-P., Yang, Y., 1998. Compaction-driven evolution of porosity and permeability in natural mudstones: An experimental study. *Journal of Geophysical Research*, 103(B1), 651-661.

Dewhurst, D.N., Aplin, A.C., Sarda, J.-P., 1999. Influence of clay fraction on pore-scale properties and hydraulic conductivity of experimentally compacted mudstones. *Journal of Geophysical Research*, 104(B12), 651-661.

Dickens, G.R., Castillo, M.M., Walker, J.C.G., 1997. A blast of gas in the latest Paleocene: Simulating first-order effects of massive dissociation of oceanic methane hydrate. *Geology*, 25(3), 259-262.

Dillon, W.P., Danforth, W.W., Hutchinson, D.R., Drury, R.M., Taylor, M.H., Booth, J.S., 1998. Evidence for faulting related to dissociation of gas hydrate and release of methane off the southeastern United States. In: J.-P. Henriet, J. Mienert (Editors), *Gas Hydrates: Relevance to World Margin Stability and Climate Change*, Geological Society Special Publication 137, The Geological Society, London, pp. 293-302.

Dillon, W.P., Hutchinson, D.R., Drury, R.M., 1996. Seismic reflection profiles on the Blake Ridge near sites 994, 995, and 997. *Proceedings of the Ocean Drilling Program, Initial Results*, 164, 47-56, doi:10.2973/odp.proc.ir.164.104.1996.

Duan, Z., Møller, N., Greenberg, J., Weare, J.H., 1992. The prediction of methane solubility in natural waters to high ionic strength from 0 to 250°C and from 0 to 1600 bar. *Geochimica et Cosmochimica Acta*, 56, 1451–1460, doi:10.1016/0016-7037(92)90215-5.

Dugan, B., 2003. Measuring pore pressure in marine sediments with penetrometers: Comparison of the Piezoprobe and DVTP-P tools in ODP Leg 203. In: B.J. Thompson (Editor), *Research Papers of the Link Foundation Fellows*, vol. 3. University of Rochester, Rochester, NY, pp. 179-199.

Dugan, B., 2008. Fluid flow in the Keathley Canyon 151 mini-basin, northern Gulf of Mexico. *Marine and Petroleum Geology*, 25(9), 919-923, doi:10.1016/j.marpetgo.2007.12.005.

Dugan, B., Daigle, H., in press. Data report: Permeability, compressibility, stress state, and grain-size of shallow sediments from the sites C0004, C0006, C0007, and C0008 of the Nankai accretionary complex. *Proceedings of the Integrated Ocean Drilling Program*, 316.

Durham, W.B., Kirby, S.H., Stern, L.A., Zhang, W., 2003. The strength and rheology of methane clathrate hydrate. *Journal of Geophysical Research*, 108(B4), 2182, doi:10.1029/2002JB001872.

Egeberg, P. K., Dickens, G.R., 1999. Thermodynamic and pore water halogen constraints on gas hydrate distribution at ODP Site 997 (Blake Ridge). *Chemical Geology*, 153, 53–79, doi:10.1016/S0009-2541(98)00152-1.

Ellis, D.V., 1987. *Well Logging for Earth Scientists*. Elsevier, New York, 532 pp.

Expedition 308 Scientists, 2006. Methods. *Proceedings of the Integrated Ocean Drilling Program*, 308, 1-44, doi:10.2204/iodp.proc.308.102.2006.

Expedition 316 Scientists, 2009. Expedition 316 methods. *Proceedings of the Integrated Ocean Drilling Program*, 314/315/316, doi:10.2204/iodp.proc.314315316.132.2009.

Faivre, C., Bellet, D., Dolino, G., 1999. Phase transitions of fluids confined in porous silicon: A differential calorimetry investigation. *European Physical Journal B*, 7, 19-36.

Finkbeiner, T., Zoback, M., Flemings, P., Stump, B., 2001. Stress, pore pressure, and dynamically constrained hydrocarbon columns in the South Eugene Island 330 field, northern Gulf of Mexico. *AAPG Bulletin*, 85(6), 1007-1031.

Flemings, P.B., Behrmann, J.H., John, C.M., et al., 2006. Expedition 308 summary. *Proceedings of the Integrated Ocean Drilling Program*, 308, 1-70, doi:10.2204/iodp.proc.308.101.2006.

Flemings, P. B., Liu, X., Winters, W.J., 2003. Critical pressure and multiphase flow in Blake Ridge gas hydrates. *Geology*, 31(12), 1057–1060, doi:10.1130/G19863.1.

Fletcher, C.A.J., 1997. *Computational Techniques for Fluid Dynamics, Volume 1: Fundamental and General Techniques*, 2nd ed. Berlin: Springer, 401 pp.

Franke, C., Fu, Y., Heslop, D., von Dobeneck, T., 2009. Data report: Natural remanent magnetization of IODP Holes U1319A, U1320A, U1322B, and U1324B and magnetic carrier identification by scanning electron microscopy. *Proceedings of the Integrated Ocean Drilling Program*, 308, 1-16, doi:10.2204/iodp.proc.308.209.2009.

Freeze, R.A., Cherry, J.A., 1979. *Groundwater*. Englewood Cliffs, NJ: Prentice-Hall, 604 pp.

Friedrich, J.T., Greaves, K.H., Martin, J.W., 1993. Pore geometry and transport properties of Fontainebleau sandstone. *International Journal of Rock Mechanics and Mining Sciences and Geomechanical Abstracts*, 30(7), 691-697.

Garg, S. K., Pritchett, J.W., Katoh, A., Baba, K., Fujii, T., 2008. A mathematical model for the formation and dissociation of methane hydrates in the marine environment. *Journal of Geophysical Research*, 113, B01201, doi:10.1029/2006JB004768.

Ginsburg, G., Soloviev, V., Matveeva, T., Andreeva, I., 2000. Sediment grain-size control on gas hydrate presence, Site 994, 995, and 997. *Proceedings of the Ocean Drilling Program, Scientific Results*, 164, 237-245, doi:10.2973/odp.proc.sr.164.236.2000.

Gorman, A. R., Holbrook, W.S., Hornbach, M.J., Hackwith, K.L., Lizzaralde, D., Pecher, I., 2002. Migration of methane gas through the hydrate stability zone in a low-flux hydrate province. *Geology*, 30(4), 327–330, doi:10.1130/0091-7613(2002)030<0327:MOMGTT>2.0.CO;2.

Gràcia, E., Martínez-Ruiz, F., Piñero, E., Larrasoaña, J.C., Vizcaino, A., Ercilla, G., 2006. Data report: Grain-size and bulk and clay mineralogy of sediments from the summit and flanks of southern Hydrate Ridge, Sites 1244-1250, ODP Leg 204. *Proceedings of the Ocean Drilling Program, Scientific Results*, 204, 1-19, doi:10.2973/odp.proc.sr.204.110.2006.

Guerin, G., Goldberg, D., Meltser, A., 1999. Characterization of in situ elastic properties of gas-hydrate bearing sediments on the Blake Ridge. *Journal of Geophysical Research*, 104(B8), 17,781–17,795, doi:10.1029/1999JB900127.

Hadley, C., Peters, D., Vaughn, A., 2008. Gumusut-Kakap project: Geohazard characterization and impact on field development plans, paper presented at International Petroleum Technology Conference, Kuala Lumpur, Malaysia.

Handa, Y.P., 1990. Effect of hydrostatic pressure and salinity on the stability of gas hydrates. *Journal of Physical Chemistry*, 94(6), 2652-2657, doi:10.1021/j100369a077.

Handa, Y.P., Stupin, D., 1992. Thermodynamic properties and dissociation characteristics of methane and propane hydrates in 70-Å-radius silica gel pores. *Journal of Physical Chemistry*, 96(21), 8599-8603, doi:10.1021/j100200a071.

Happel, J., Brenner, H., 1983. *Low Reynolds Number Hydrodynamics with Special Applications to Particulate Media*, first paperback ed. Martins Nijhoff Publishers, The Hague, 553 pp.

Henry, P., Thomas, M., Clennell, M.B., 1999. Formation of natural gas hydrates in marine sediments: 2. Thermodynamic calculations of stability conditions in porous sediments. *Journal of Geophysical Research*, 104(B10), 23,005–23,022, doi:10.1029/1999JB900167.

Hiltl, M., Hagelberg, C.R., Swift, R.P., Carney, T.C., Nellis, W.J., 2000. Dynamic response of Berea Sandstone shock loaded under dry, wet, and water-pressurized conditions. Paper presented at International Conference on High Pressure Science and Technology, International Association for the Advancement of High Pressure Science and Technology, Honolulu, HI, 25-30 July, 1999.

Holbrook, W.S., 2001. Seismic studies of the Blake Ridge: Implications for hydrate distribution, methane expulsion, and free gas dynamics. In: C.K. Paull and W.P. Dillon

(Editors), *Natural Gas Hydrates: Occurrence, Distribution, and Detection, Geophysical Monograph Series,* 124, Washington, DC: American Geophysical Union, pp. 235-256.

Holbrook, W.S., Hoskins, H., Wood, W.T., Stephen, R.A., Lizarralde, D., Leg 164 Science Party, 1996. Methane hydrate and free gas on the Blake Ridge from vertical seismic profiling. *Science*, 273(5283), 1840-1843, doi:10.1126/science.273.5283.1840.

Holbrook, W.S., Lizarralde, D., Pecher, I.A., Gorman, A.R., Hackwith, K.L., Hornbach, M., Saffer, D., 2002. Escape of methane gas through sediment waves in a large methane hydrate province. *Geology*, 30(5), 467-470.

Hornbach, M. J., Saffer, D.M., Holbrook, W.S., 2004. Critically pressured free-gas reservoirs below gas-hydrate provinces. *Nature*, 427, 142–144, doi:10.1038/nature02172.

Hornbach, M. J., Saffer, D.M., Holbrook, W.S., Van Avendonk, H.J.A., Gorman, A.R., 2008. Three-dimensional seismic imaging of the Blake Ridge methane hydrate province: Evidence for large, concentrated zones of gas hydrate and morphologically driven advection. *Journal of Geophysical Research*, 113, B07101, doi:10.1029/2007JB005392.

Huang, C.-C., 1997. *Estimation of Rock Properties by NMR Relaxation Methods.* MS Thesis, Department of Chemical Engineering, Rice University, Houston, TX, 168 pp.

Hürlimann, M.D., 1998. Effective gradients in porous media due to susceptibility differences. *Journal of Magnetic Resonance,* 131, 232-240.

Hutchinson, D.R., Hart, P.E., Collett, T.S., Edwards, K.M., Twichell, D.C., Snyder, F., 2008. Geologic framework of the 2005 Keathley Canyon gas hydrate research well, northern Gulf of Mexico. *Marine and Petroleum Geology*, 25(9), 906-918, doi:10.1016/j.marpetgeo.2008.01.012.

Hyodo, M., Nakata, Y., Yoshimoto, N., Ebinuma, T., 2005. Basic research on the mechanical behavior of methane hydrate-sediments mixture. *Soils and Foundations*, 45(1), 75-85.

Ingebritsen, S., Sanford, W., Neuzil, C., 2006. *Groundwater in Geologic Processes*, 2nd ed. Cambridge, UK: Cambridge University Press, 536 pp.

Jain, A.K., Juanes, R., 2009. Preferential mode of gas invasion in sediments: Grain-scale mechanistic model of coupled multiphase fluid flow and sediment mechanics. *Journal of Geophysical Research*, 114, B08101, doi:10.1029/2008JB006002.

John, C.M., Adatte, T., 2009. Data report: X-ray analyses of bulk sediment in IODP Holes U1320A and U1324B, northern Gulf of Mexico. *Proceedings of the Integrated Ocean Drilling Program,* 308, 1-19, doi:10.2204/iodp.proc.308.214.2009.

Johnson, D.L., Koplik, J., Schwartz, L.M., 1986. New pore-size parameter characterizing transport in porous media. *Physical Review Letters*, 57(20), 2564-2567.

Kameda, A., Dvorkin, J., Keehm, Y., Nur, A., Bost, W., 2006. Permeability-porosity transforms from small sandstone fragments. *Geophysics*, 71(1), N11-N19, doi:10.1190/1.2159054.

Karig, D.E., Hou, G., 1992. High-stress consolidation experiments and their geologic implications. *Journal of Geophysical Research*, 97(B1), 289-300.

Kastner, M., Claypool, G., Robertson, G., 2008. Geochemical constraints on the origin of the pore fluids and gas hydrate distribution at Atwater Valley and Keathley Canyon, northern Gulf of Mexico. *Marine and Petroleum Geology*, 25(9), 860-872, doi:10.1016/j.marpetgeo.2008.01.022.

Katz, A.J., Thompson, A.H., 1986. Quantitative prediction of permeability in porous rock. *Physical Review B*, 34(11), 8179-8181.

Kenyon, W.E., Day, P.I., Straley, C., Willemsen, J.F., 1988. A three-part study of NMR longitudinal relaxation properties of water-saturated sandstones. *SPE Formation Evaluation*, 3(3), 622-636.

Kenyon, W.E., Kleinberg, R.L., Straley, C., Gubelin G.,, Morriss, C., 1995. Nuclear magnetic resonance imaging– technology for the 21st century. *Oilfield Review*, 7(3), 19-33.

Kenyon, W.E., Kolleeny, J.A., 1995. NMR surface relaxivity of calcite with adsorbed Mn2+. *Journal of Colloid and Interface Science*, 170(2), 502-514, doi:10.1006/jcis.1995.1129.

Kleinberg, R.L., 1996. Utility of NMR T_2 distributions, connection with capillary pressure, clay effect, and determination of the surface relaxivity parameter ρ_2. *Magnetic Resonance Imaging*, 14(7/8), 761-767.

Kleinberg, R.L., 1999. Nuclear magnetic resonance. In: P.-Z. Wong (Editor), *Methods in the Physics of Porous Media*. Academic Press, San Diego, pp. 337-385.

Kleinberg, R.L., Flaum, C., Straley, C., Brewer, P.G., Malby, G.E., Peltzer III, E.T., Friedrich, G., Yesinowski, J.P., 2003a. Seafloor nuclear magnetic resonance assay of methane hydrate in sediment and rock. *Journal of Geophysical Research*, 108(B3), 2137, doi:10.1029/2001JB000919.

Kleinberg, R.L., Flaum, C., Griffin, D.D., Brewer, P.G., Malby, G.E., Peltzer, E.T., Yesinowski, J.P., 2003b. Deep sea NMR: Methane hydrate growth habit in porous media and its relationship to hydraulic permeability, deposit accumulation, and submarine slope stability. *Journal of Geophysical Research*, 108(B10), 2508, doi:10.1029/2003JB002389.

Kozeny, J., 1927. Über kapillare Leitung des Wassers im Boden – Aufstieg, Versickerung und Anwendung auf die Bewässerung. *Sitzungsberichte der Akademie der Wissenschaften in Wien*, 136, 271-306.

Kraemer, L.M., Owen, R.M., Dickens, G.R., 2000. Lithology of the upper gas hydrate zone, Blake Outer Ridge: A link between diatoms, porosity, and gas hydrate. *Proceedings of the Ocean Drilling Program, Scientific Results*, 164, 229-236, doi:10.2973/odp.proc.sr.164.221.2000.

Krause, F.F., 2000. Genesis and geometry of the Meiklejohn Peak lime mud-mound, Bare Mountain Quadrangle, Nevada, USA: Ordovician limestone with submarine frost heave structures – a possible response to gas clathrate hydrate evolution. *Sedimentary Geology*, 145, 189-213.

Kvamme, B., Graue, A., Buanes, T., Kuznetsova, T., Ersland, G., 2009. Effects of solid surfaces on hydrate kinetics and stability. In: D. Long, et al. (Editors), *Sediment-Hosted Gas Hydrates: New Insights on Natural and Synthetic Systems, Geological Society of London Special Publications Series*, 319. The Geological Society, London, pp. 131-144.

Kvenvolden, K.A., 1993. Gas hydrates – geological perspective and global change. *Reviews of Geophysics*, 31(2), 173-187..

Lee, J.Y., Santamarina, J.C., Ruppel, C., 2008. Mechanical and electromagnetic properties of northern Gulf of Mexico sediments with and without THF hydrates. *Marine and Petroleum Geology*, 25(9), 884-895, doi:10.1016/j.marpetgeo.2008.01.019.

Lee, J.Y., Santamarina, J.C., Ruppel, C., 2010. Volume change associated with formation and dissociation of hydrate in sediment. *Geochemistry, Geophysics, Geosystems*, 11(3), Q03007, doi:10.1029/2009GC002667.

Lee, J.Y., Yun, T.S., Santamarina, J.C., Ruppel, C., 2007. Observations related to tetrahydrofuran and methane hydrates for laboratory studies of hydrate-bearing sediments. *Geochemistry, Geophysics Geosystems*, 8(6), Q06003, doi:10.1029/2006GC001531.

Lee, M. W., 2000. Gas hydrates amount estimated from acoustic logs at the Blake Ridge, Site 994, 995, and 997. *Proceedings of the Ocean Drilling Program, Scientific Results*, 164, 193–198, doi:10.2973/odp.proc.sr.164.239.2000.

Lee, M. W., Collett, T.S., 2006. Gas hydrate and free gas saturations estimated from velocity logs on Hydrate Ridge, offshore Oregon, USA. *Proceedings of the Ocean Drilling Program, Scientific Results*, 204, 1–25, doi:10.2973/odp.proc.sr.204.103.2006.

Lee, M.W., Collett, T.S., 2008. Integrated analysis of well logs and seismic data to estimate gas hydrate concentrations at Keathley Canyon, Gulf of Mexico. *Marine and Petroleum Geology*, 25(9), doi:10.1016/j.marpetgeo.2007.09.002.

Lee., M.W., Collett, T.S., 2009. Gas hydrate saturations estimated from fractured reservoir at Site NGHP-01-10, Krishna-Godavari Basin, India. *Journal of Geophysical Research*, 114, B07102, doi:10.1029/2008JB006237.

Lide, D.R. (Ed.), 2009. *Handbook of Chemistry and Physics*, 90th ed. Cleveland, OH: Chemical Rubber Company, 2804 pp.

Liu, X., Flemings, P.B., 2006. Passing gas through the hydrate stability zone at southern Hydrate Ridge, offshore Oregon. *Earth and Planetary Science Letters*, 241(1–2), 211–226, doi:10.1016/j.epsl.2005.10.026.

Liu, X., Flemings, P.B., 2007. Dynamic multiphase flow model of hydrate formation in marine sediments. *Journal of Geophysical Research*, 112, B03101, doi:10.1029/2005JB004227.

Lovely, P.J., Pollard, D.D., Mutlu, O., 2009. Regions of reduced static stress drop near fault tips for large strike-slip earthquakes. *Bulletin of the Seismological Society of America*, 99(3), 1691-1704, doi:10.1785/0120080358.

Malinverno, A., 2010. Marine gas hydrates in thin sand layers that soak up microbial methane. *Earth and Planetary Science Letters*, 292, 399-408, doi:10.1016/j.epsl.2010.02.008.

Malinverno, A., Kastner, M., Torres, M.E., Wortmann, U.G., 2008. Gas hydrate occurrence from pore water chlorinity and downhole logs in a transect across the northern Cascadia margin (Integrated Ocean Drilling Progam Expedition 311). *Journal of Geophysical Research*, 113, B08103, doi:10.1029/2008JB005702.

March, A., 1932. Mathematische Theorie der Regelungen nach der Korngestalt bei affiner Deformation. *Zeitschrift für Kristallographie, Mineralogie, und Petrographie*, 1, 285-297.

Martys, N.S., Torquato, S., Bentz, D.P., 1994. Universal scaling of fluid permeability for sphere packings. *Physical Review E*, 50(1), 403-409.

Mason, G., 1981. The effect of pore-space connectivity on the hysteresis of capillary condensation in adsorption-desorption isotherms. *Journal of Colloid and Interface Science*, 88(1), 36-46.

Masui, A., Miyazaki, K., Haneda, H., Ogata, Y., Aoki, K., 2008. Mechanical characteristics of natural and artificial gas hydrate bearing sediments, paper 5697 presented at 6th International Conference on Gas Hydrates, Vancouver, British Columbia, Canada.

Matteson, A., Tomanic, J.P., Herron, M.M., Allen, D.F., Kenyon, W.E., 2000. NMR relaxation of clay/brine mixtures. *Society of Petroleum Engineers Formation Evaluation and Engineering*, 3(5), 408-413.

Mazzei, D.P.C., 2008. *Normalized Mechanical Properties of Resedimented Gulf of Mexico Clay from Integrated Ocean Drilling Program Expedition Leg 308*. MS Thesis, Department of Civil and Environmental Engineering, Massachusetts Institute of Technology, Cambridge, MA, 137 pp.

Mello, U.T., Karner, G.D., Anderson, R.N., 1994. A physical explanation for the positioning of the depth to the top of overpressure in shale-dominated sequences in the Gulf Coast basin, United States. *Journal of Geophysical Research*, 99(B2), 2775-2789.

Menéndez, B., Zhu, W., Wong, T.-F., 1996. Micromechanics of brittle faulting and cataclastic flow in Berea sandstone. *Journal of Structural Geology*, 18(1), 1-16.

Moore, D.S., McCabe, G.P., 1999. *Introduction to the Practice of Statistics,* third ed. W.H. Freeman and Company, New York, 825 pp.

Mountain, G.S., Tucholke, B.E., 1985. Mesozoic and Cenozoic geology of the US Atlantic continental slope and rise. In: C.W. Poag (Editor), *Geologic Evolution of the United States Atlantic Margin*. New York: Van Nostrand Reinhold, pp. 293-341.

Neuzil, C., 1994. How permeable are clays and shales? *Water Resources Research*, 30, 145-150.

Nimblett, J., Ruppel, C., 2003. Permeability evolution during the formation of gas hydrates in marine sediments. *Journal of Geophysical Research*, 108(B9), doi:10.1029/2001JB001650.

Panda, M.N., Lake, L.W., 1994. Estimation of single-phase permeability from parameters of particle-size distribution. *AAPG Bulletin,* 78(7), 1028-1039.

Paterson, L., Painter, S., Knackstedt, M.A., Pinczewski, W.V., 1996. Patterns of fluid flow in naturally heterogeneous rocks. *Physica A* 233, 619-628.

Paull, C.K., Matsumoto, R., 2000. Leg 164 overview. *Proceedings of the Ocean Drilling Program, Scientific Results*, 164. 3-10, doi:10.2973/odp.proc.sr.164.204.2000.

Peyron, M., Pierens, G.K., Lucas, A.J., Hall, L.D., Stewart, R.C., 1996. The modified stretched-exponential model for characterization of NMR relaxation in porous media. *Journal of Magnetic Resonance Series A*, 118, 214-220.

Porter, D.A., Easterling, K.E., 1992. *Phase Transformations in Metals and Alloys*. London: Chapman and Hall, 514 pp.

Prodanović, M., Bryant, S.L., 2006. A level set method for determining critical curvatures for drainage and imbibitions. *Journal of Colloid and Interface Science*, 304(2), 442-458, doi:10.1016/j.jcis.2006.08.048.

Rempel, A.W., 2007. Formation of ice lenses and frost heave. *Journal of Geophysical Research*, 112, F02S21, doi:10.1029/2006JF000525.

Rempel, A. W., Buffett, B.A., 1997. Formation and accumulation of gas hydrate in porous media. *Journal of Geophysical Research*, 102(B5), 10,151–10,164, doi:10.1029/97JB00392.

Rempel, A.W., Wettlaufer, J.S., Worster, M.G., 2004. Premelting dynamics in a continuum model of frost heave. *Journal of Fluid Mechanics*, 498, 227-244, doi:10.1017/S0022112003006761.

Revil, A., Cathles, L.M., 1999. Permeability of shaly sands. *Water Resources Research*, 35(3), 651-662, doi:10.1029/98WR02700.

Revil, A., Cathles, L.M., Shosa, J.D., Pezard, P.A., de Larouzière, F.D., 1998. Capillary sealing in sedimentary basins: A clear field example. *Geophysical Research Letters*, 25(3), 389-392.

Revil, A., Florsch, N., 2010. Determination of permeability from spectral induced polarization in granular media. *Geophysical Journal International*, 181(3), 1480-1498, doi:10.1111/j.1365-246X.2010.04573.x.

Reynolds, J.M., 1997. *An Introduction to Applied and Environmental Geophysics*. Chichester, England: John Wiley and Sons, 796 pp.

Riedel, M., 2007. 4D seismic time-lapse monitoring of an active cold vent, northern Cascadia margin. *Marine Geophysical Researches*, 38(4), 355-371, doi:10.1007/s11001-007-9037-2.

Riedel, M., Collett, T.S., Malone, M.J., Expedition 311 Scientists, 2006. Site U1325. *Proceedings of the Integrated Ocean Drilling Program*, 311, 1-111, doi:10.2204/iodp.proc.311.103.2006.

Rose, H.E., 1945. An investigation into the laws of flow of fluids through beds of granular materials. *Proceedings of the Institution of Mechanical Engineers*, 153, 141-148.

Rowe, M.M., Gettrust, J.F., 1993. Fine structure of methane hydrate-bearing sediments on the Blake Outer Ridge as determined from deep-tow multichannel seismic data. *Journal of Geophysical Research*, 98(B1), 463-473.

Ruppel, C., 1997. Anomalously cold temperatures observed at the base of the gas hydrate stability zone on the U.S. Atlantic passive margin. *Geology*, 25(8), 699-702.

Ruppel, C., Boswell, R., Jones, E., 2008. Scientific results from Gulf of Mexico Gas Hydrates Joint Industry Project Leg 1 drilling: Introduction and overview. *Marine and Petroleum Geology*, 25(9), 819-829, doi:10.1016/j.marpetgeo.2008.02.007.

Saffer, D.M., McKiernan, A.W., 2005. Permeability of underthrust sediments at the Costa Rican subduction zone: Scale dependence and implications of dewatering. *Geophysical Research Letters*, 32, L02302, doi:10.1029/2004GL021388.

Santamarina, J.C., Klein, K.A., Fam, M.A., 2001. *Soils and Waves*. Chichester, England: John Wiley and Sons, 488 pp.

Santamarina, J.C., Klein, K.A., Wang, Y.H., Prencke, E., 2002. Specific surface: determination and relevance. *Canadian Geotechnical Journal*, 39, 233-241, doi:10.1139/T01-077.

Sawyer, D.E., Flemings, P.B., Shipp, R.C., Winker, C.D., 2007. Seismic geomorphology, lithology, and evolution of the Pleistocene Mars-Ursa turbidite region, Mississippi Canyon area, northern Gulf of Mexico. *AAPG Bulletin*, 91(2), 215-234, doi:10.1306/08290605190.

Sawyer, D.E., Jacoby, R., Flemings, P.B., Germaine, J.T., 2009. Data report: Particle size analysis of sediments in the Ursa Basin, IODP Expedition 308 Sites U1324 and U1322, northern Gulf of Mexico. *Proceedings of the Integrated Ocean Drilling Program,* 308, 1-20, doi:10.2204/iodp.proc.308.205.2008.

Sayers, C.M., van Munster, J.G., King, M.S., 1990. Stress-induced ultrasonic anisotropy in Berea sandstone. *International Journal of Rock Mechanics and Mining Sciences and Geomechanics Abstracts*, 27(5), 429-436.

Scheidegger, A., 1974. *The Physics of Flow Through Porous Media*, third ed. University of Toronto Press, Toronto, 353 pp.

Schleuter, E.M., 1995. *Predicting the Transport Properties of Sedimentary Rocks from Microstructure*. PhD thesis, Department of Materials Science and Mineral Engineering, University of California, Berkeley, CA, 268 pp.

Schlumberger Limited, 2004. *DSI Dipole Shear Sonic Imager*, http://www.slb.com/~/media/Files/evaluation/product_sheets/wireline_open_hole/petrophysics/acoustic/dsi.ashx.

Schlumberger Limited, 2007. *GeoVISION: Resistivity imaging provides multiple depths of investigation while drilling*, http://www.slb.com/media/services/drilling/imaging/geovision.pdf.

Schreiner, W.H., Lombardi, K.C., de Oliveira, A.J.A., Mattoso, N., Abbate, M., Wypych, F., Mangrich, A.S., 2002. Paramagnetic anisotropy of a natural kaolinite and its modification by chemical reduction. *Journal of Magnetism and Magnetic Materials,* 241(2-3), 422-429, doi:10.1016/S0304-8853(01)00480-2.

Schultheiss, P., Holland, M., Roberts, J., 2006. Gulf of Mexico Gas Hydrates Joint Industry Project pressure coring and core logging. In: G.E. Claypool (Editor), *Cruise Report: The Gulf of Mexico Gas Hydrate Joint Industry Project*, http://www.netl.doe.gov/technologies/oil-gas/publications/Hydrates/reports/GOMJIPCruise05.pdf.

Schwartz, L.M., Banavar, J.R., 1989. Transport properties of disordered continuum systems. *Physical Review B*, 39(16), 11965-11970.

Screaton, E.J., Kimura, G., Curewitz, D., et al., 2009. Expedition 316 summary. *Proceedings of the Integrated Ocean Drilling Program,* 314/315/316, 1-29, doi:10.2204/iodp.proc.314315316.131.2009.

Seevers, D.O., 1966. A nuclear magnetic method for determining the permeability of sandstones. *Transactions of the Society of Petrophysicists and Well Log Analysts 7th Annual Logging Symposium,* Paper L.

Serra, O., 1990. *Element Mineral Rock Catalog.* Sugar Land, TX: Schlumberger Limited, 253 pp.

Shipboard Scientific Party, 1996. Site 997. *Proceedings of the Ocean Drilling Program, Initial Reports,* 164, 277–334, doi:10.2973/odp.proc.ir.164.110.1996.

Shipboard Scientific Party, 2003. Leg 204 summary. *Proceedings of the Ocean Drilling Program, Initial Reports,* 204, 1–75, doi:10.2937/odp.proc.ir.204.101.2003.

Shosa, J.D., Cathles, L.M., 2001. Experimental investigation of capillary blockage of two phase flow in layered porous media. Paper presented at 21st Annual Bob Perkins Research Conference, Gulf Coast Section SEPM Foundation, Houston, Texas, 2-5 December 2001.

Simpson, J.H., Carr, H.Y., 1958. Diffusion and nuclear spin relaxation in water. *Physical Review,* 111(5), 1201-1202.

Slade, P.G., Quirk, J.P., Norrish, K., 1991. Crystalline swelling of smectite samples in concentrated NaCl solutions in relation to layer charge. *Clays and Clay Minerals,* 39(3), 234-238.

Sloan, E.D. Jr., 1990. *Clathrate Hydrates of Natural Gases.* New York: M. Dekker, 641 pp.

Snow, D.T., 1968. Rock fracture spacings, openings, and porosities. *Journal of the Soil Mechanics and Foundation Division of the American Society of Civil Engineers,* 94(SM1), 73-91.

Straley, C., Rossini, D., Vinegar, H., Tutunjian, P., Morriss, C., 1994. Core analysis by low field NMR. Paper presented at 1994 International Symposium, paper SCA-9404, Society of Core Analysts, Stavanger, Norway, 12-14 September 1994.

Sun, X., Mohanty, K.K., 2006. Kinetic simulation of methane hydrate formation and dissociation in porous media. *Chemical Engineering Science,* 61(11), 3476-3495, doi:10.1016/j.ces.2005.12.017.

Svandal, A., Kuznetsova, T., Kvamme, B., 2006. Thermodynamic properties and phase transitions in the H2O/CO2/CH4 system. *Fluid Phase Equilibria,* 246(1-2), 177-184, doi:10.1016/j.fluid.2006.06.003.

Tan, B., Germaine, J.T., Flemings, P.B., 2006. Data report: Consolidation and strength characteristics of sediments from ODP Site 1244, Hydrate Ridge, Cascadia continental margin. *Proceedings of the Ocean Drilling Program, Scientific Results*, 204, 1–148, doi:10.2973/odp.proc.sr.204.102.2006.

Thomson, W., 1871. On the equilibrium of vapour at a curved surface of liquid. *Philosophical Magazine*, 42(282), 448-452, doi:10.1080/14786447108640606.

Timur, A., 1968. An investigation of permeability, porosity, & residual water saturation relationships for sandstone reservoirs. *The Log Analyst*, 9(4), 8-17.

Tohidi, B., Anderson, R., Clennell, M.B., Burgass, R.W., Biderkab, A.B., 2001. Visual observation of gas-hydrate formation and dissociation in synthetic porous media by means of glass micromodels. *Geology*, 29(9), 867-870, doi:10.1130/0091-7613(2001)029<0867:VOOGHF>2.0.CO;2.

Torres, M. E., McManus, J., Hammond, D.E., de Angelis, M.A., Heeschen, D.U., Colbert, S.L., Tryon, M.D., Brown, K.M., Suess, E., 2002. Fluid and chemical fluxes in and out of sediments hosting methane hydrate deposits on Hydrate Ridge, OR, I: Hydrological provinces. *Earth and Planetary Science Letters*, 201, 525–540, doi:10.1016/S0012-821X(02)00733-1.

Torres, M.E., Tréhu, A.M., Cespedes, N., Kastner, M., Wortmann, U.G., Kim, J.-H., Long, P., Malinverno, A., Pohlmann, J.W., Riedel, M., Collett, T., 2008. Methane hydrate formation in turbidite sediments of northern Cascadia, IODP Expedition 311. *Earth and Planetary Science Letters*, 271, 170-180, doi:10.1016/j.epsl.2008.03.061.

Tréhu, A. M., 2006. Subsurface temperatures beneath southern Hydrate Ridge. *Proceedings of the Ocean Drilling Program, Scientific Results*, 204, 1–26, doi:10.2973/odp.proc.sr.204.114.2006.

Tréhu, A. M., Flemings, P.B., Bangs, N.L., Chevallier, J., Gràcia, E., Johnson, J.E., Liu, C.-S., Liu, X., Riedel, M., Torres, M.E., 2004. Feeding methane vents and gas hydrate deposits at South Hydrate Ridge. *Geophysical Research Letters*, 31, L23310, doi:10.1029/2004GL021286.

Tréhu, A.M., Ruppel, C., Holland, M., Dickens, G.R., Torres, M.E., Collett, T.S., Goldberg, D., Riedel, M., Schultheiss, P., 2006a. Gas hydrates in marine sediments: Lessons from scientific ocean drilling. *Oceanography*, 19(4), 124-142.

Tréhu, A.M., Torres, M.E., Bohrmann, G., Colwell, F.S., 2006b. Leg 204 synthesis: Gas hydrate distribution and dynamics in the central Cascadia accretionary complex. *Proceedings of the Ocean Drilling Program, Scientific Results*, 204, 1–40, doi:10.2973/odp.proc.sr.204.101.2006.

Tryon, M. D., Brown, K.M., Torres, M.E., 2002. Fluid and chemical flux in and out of sediments hosting methane hydrate deposits on Hydrate Ridge, OR, II: Hydrological

processes. *Earth and Planetary Science Letters*, 201, 541–557, doi:10.1016/S0012-821X(02)00732-X.

Turner, D.J., Cherry, R.S., Sloan, E.D., 2006. Sensitivity of methane hydrate equilibria to sediment pore size. *Fluid Phase Equilibria*, 228-229, 505-510, doi:10.1016/j.fluid.2005.09.025.

Uchida, T., Ebinuma, T., Ishizaki, T., 1999. Dissociation condition measurements of methane hydrate in confined small pores of porous glass. *Journal of Physical Chemistry B*, 103(18), 3659-3662, doi:10.1021/jp984559l.

Uchida, T., Ebinuma, T., Takeya, S., Nagao, J., Narita, H., 2002. Effects of pore sizes on dissociation temperatures and pressures of methane, carbon dioxide, and propane hydrates in porous media. *Journal of Physical Chemistry B*, 106(4), 820-826, doi:10.1021/jp012823w.

Uchida, T., Takeya, S., Chuvilin, E.M., Ohmura, R., Nagao, J., Yakushev, V.S., Istomin, V.A., Minagawa, H., Ebinuma, T., Narita, H., 2004. Decomposition of methane hydrates in sand, sandstone, clays, and glass beads. *Journal of Geophysical Research*, 109, B05206, doi:10.1029/2003JB002771.

Valkó, P., Economides, M.J., 1995. *Hydraulic Fracture Mechanics*. Chichester, UK: John Wiley, 298 pp.

Vasseur, G., Djeran-Maigre, I., Grunberger, D., Rousset, G., Tessier, D., Velde, B., 1995. Evolution of structural and physical parameters of clays during experimental compaction. *Marine and Petroleum Geology*, 12(8), 941-954.

Waite, W.F., Santamarina, J.C., Cortes, D.D., Dugan, B., Espinoza, D.N., Germaine, J., Jang, J., Jung, J.W., Kneafsey, T.J., Shin, H., Soga, K., Winters, W.J., Yun, T.-S., 2009. Physical properties of hydrate-bearing sediments. *Reviews of Geophysics*, 47, RG4003, doi:10.1029/2008RG000279.

Wang, K., Hyndman, R.D., Davis, E.E., 1993. Thermal effects of sediment thickening and fluid expulsion in accretionary prisms: Model and parameter analysis. *Journal of Geophysical Research*, 98(B6), 9975-9984.

Watson, A.T., Chang, C.T.P., 1997. Characterizing porous media with NMR methods. *Progress in Nuclear Magnetic Resonance Spectroscopy*, 31, 343-386.

Wehner, H., Faber, E., Hufnagel, H., 2000. Characterization of low and high molecular-weight hydrocarbons in sediments from the Blake Ridge, Sites 994, 995, and 997. *Proceedings of the Ocean Drilling Program, Scientific Results*, 164, 47-58, doi:10.2973/odp.proc.sr.164.225.2000.

Weinberger, J. L., Brown, K.M., 2006. Fracture networks and hydrate distribution at Hydrate Ridge, Oregon. *Earth and Planetary Science Letters*, 245, 123–136, doi:10.1016/j.epsl.2006.03.012.

Weinberger, J.L., Brown, K.M., Long, P.E., 2005. Painting a picture of gas hydrate distribution with thermal images. *Geophysical Research Letters*, 32, L04609, doi:10.1029/2004GL021437.

Winters, W.J., Dallimore, S.R., Collett, T.S., Katsube, T.J., Jenner, K.A., Cranston, R.E., Wright, J.F., Dixon, F.M., Uchida, T., 1999. Physical properties of sediments from the JAPEX/JNOC/GSC Mallik 2L-38 gas hydrate research well. *Geological Survey of Canada Bulletin*, 544, 95-100.

Winters, W.J., Dugan, B., Collett, T.S., 2008. Physical properties of sediments from Keathley Canyon and Atwater Valley, JIP Gulf of Mexico gas hydrate drilling program. *Marine and Petroleum Geology*, 25(9), 896-905, doi:10.1016/j.marpetgeo.2008.01.018.

Wong, R.C.K., 2003. A model for strain-induced permeability anisotropy in deformable granular media. *Canadian Geotechnical Journal,* 40, 95-106, doi:10.1139/T02-088.

Wood, W. T., Ruppel, C., 2000. Seismic and thermal investigations of the Blake Ridge gas hydrate area: A synthesis. *Proceedings of the Ocean Drilling Program, Scientific Results*, 164, 253–264, doi:10.2973/odp.proc.sr.164.203.2000.

Wright, H.M.N., Cashman, K.V., Gottesfeld, E.H., Roberts, J.J., 2009. Pore structure of volcanic clasts: Measurements of permeability and electrical conductivity. *Earth and Planetary Science Letters,* 280, 93-104, doi:10.1016/j.epsl.2009.01.023.

Wright, J. F., Nixon, F.M., Dallimore, S.R., Henninges, J., Côté, M.M., 2005. In situ stability of gas hydrate in reservoir sediments of the JAPEX/JNOC/GSC et al. Mallik 5L-38 gas hydrate production research well, paper presented at Scientific Results from the Mallik 2002 Gas Hydrate Production Research Well Program, Mackenzie Delta, Geological Survey of Canada, Ottawa, Ontario.

Xu, M., Eckstein, Y., 1995. Use of weighted least-squares method in evaluation of the relationship between dispersivity and field scale. *Ground Water*, 33(6), 905-908.

Xu, P., Yu, B., 2008. Developing a new form of permeability and Kozeny-Carman constant for homogeneous porous media by means of fractal geometry. *Advances in Water Resources,* 31, 74-81, doi:10.1016/j.advwatres.2007.06.003.

Xu, W., Ruppel, C., 1999. Predicting the occurrence, distribution, and evolution of methane gas hydrate in porous marine sediments. *Journal of Geophysical Research*, 104(B3), 5081-5095.

Yang, Y., Aplin, A.C., 1998. Influence of lithology and compaction on the pore size distribution and modelled permeability of some mudstones from the Norwegian margin. *Marine and Petroleum Geology*, 15, 163-175.

Yang, Y., Aplin, A.C., 2007. Permeability and petrophysical properties of 30 natural mudstones. *Journal of Geophysical Research*, 112, B03026, doi:10.1029/2005JB004243.

Yang, Y., Aplin, A.C., 2010. A permeability-porosity relationship for mudstones. *Marine and Petroleum Geology,* 27, 1692-1697, doi:10.1016/j.marpetgeo.2009.07.001.

Yang, Y., Aplin, A.C., Larter, S.R., 2004. Quantitative assessment of mudstone lithology using geophysical wireline logs and artificial neural networks. *Petroleum Geoscience*, 10, 141-151.

Yun, T.S., Francisca, F.M., Santamarina, J.C., Ruppel, C., 2005. Compressional and shear wave velocities in uncemented sediment containing gas hydrate. *Geophysical Research Letters*, 32, L10609, doi:10.1029/2005GL022607.

Yun, T.S., Narsilio, G.A., Santamarina, J.C., 2006. Physical characterization of core samples recovered from Gulf of Mexico. *Marine and Petroleum Geology*, 23, 893-900, doi:10.1016/j.marpetgeo.2006.08.002.

Yun, T.S., Santamarina, J.C., Ruppel, C., 2007. Mechanical properties of sand, silt, and clay containing tetrahydrofuran hydrate. *Journal of Geophysical Research*, 112, B04106, doi:10.1029/2006JB004484.

Zatsepina, O.Y., Buffett, B.A., 1997. Phase equilibrium of gas hydrate: Implications for the formation of hydrate in the deep sea floor. *Geophysical Research Letters*, 24(13), 1567-1570.

Zatsepina, O. Y., Buffett, B.A., 1998. Thermodynamic conditions for the stability of gas hydrate in the seafloor. *Journal of Geophysical Research*, 103(B10), 24,127–24,139, doi:10.1029/98JB02137.

Zatsepina, O.Y., Buffett, B.A., 2003. Nucleation of gas hydrate in marine environments. *Geophysical Research Letters*, 30(9), 1451, doi:10.1029/2002GL016802.

Zhang, Q., 2001. *NMR Formation Evaluation: Hydrogen Index, Wettability and Internal Field gradients*. PhD thesis, Department of Chemical Engineering, Rice University, Houston, TX, 216 pp.

Zhang, X., Knackstedt, M.A., 1995. Direct simulation of electrical and hydraulic tortuosity in porous solids. *Geophysical Research Letters*, 22(17), 2333-2336, doi:10.1029/95GL02230.

Appendix A: Example experimental data

The following figures are examples of output data from CRS experiments, flow-through permeability measurements, and NMR T_2 measurements. All data are archived on a DVD-ROM available from Brandon Dugan.

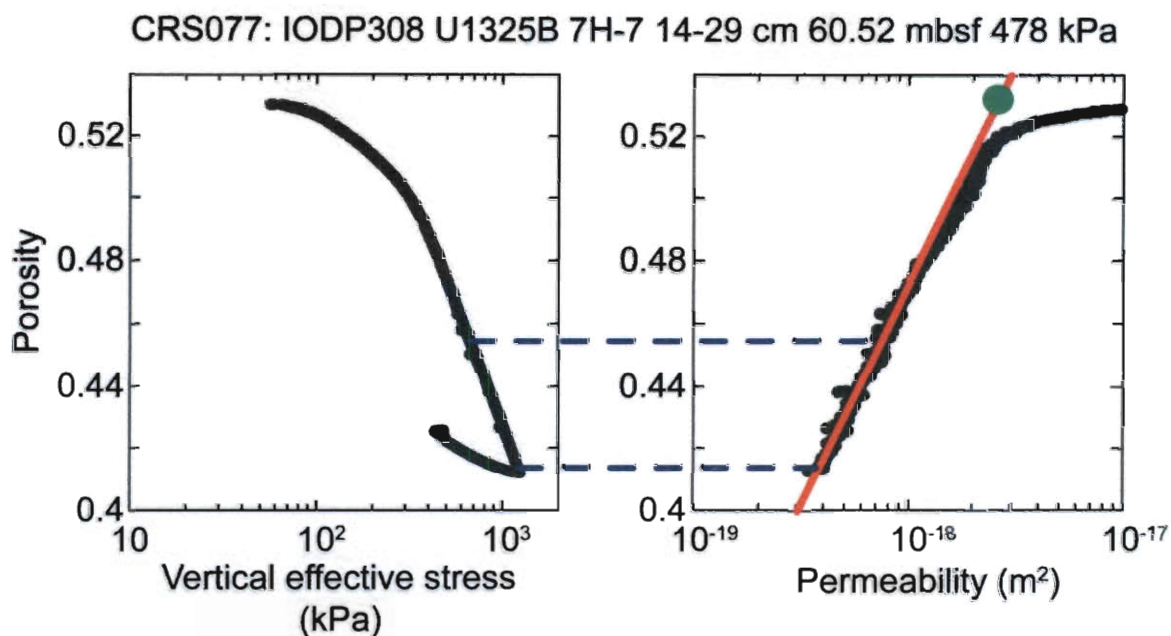CRS077: IODP308 U1325B 7H-7 14-29 cm 60.52 mbsf 478 kPa

Figure A.1. Data from CRS experiment used to determine permeability. On the left, porosity is plotted against vertical effective stress on a logarithmic scale. The elasto-plastic (virgin) portion of the consolidation curve is the linear portion of this curve. On the right, porosity is plotted against permeability on a logarithmic scale. The permeability data from the elasto-plastic portion of the consolidation curve are isolated, here represented by the area between the blue dashed lines. A log-linear relationship is determined between porosity and permeability for this portion of the data, shown on the right as the red line. This relationship is then extrapolated to the initial porosity, shown by the green dot. Initial porosity was determined by comparing saturated and dry masses of the sample. The initial permeability of the sample is the permeability corresponding to the initial porosity. Errors reported for CRS permeabilities are the standard deviation of the φ-log$k$ regression in units of log$k$. In this test the initial porosity was 0.530 and the permeability was determined to be 2.57×10^{-18} m^2 with an error of 0.028 log$k$.

PERM045: IODP316 C0004C
3H-2 10-15 cm 17.41 mbsf
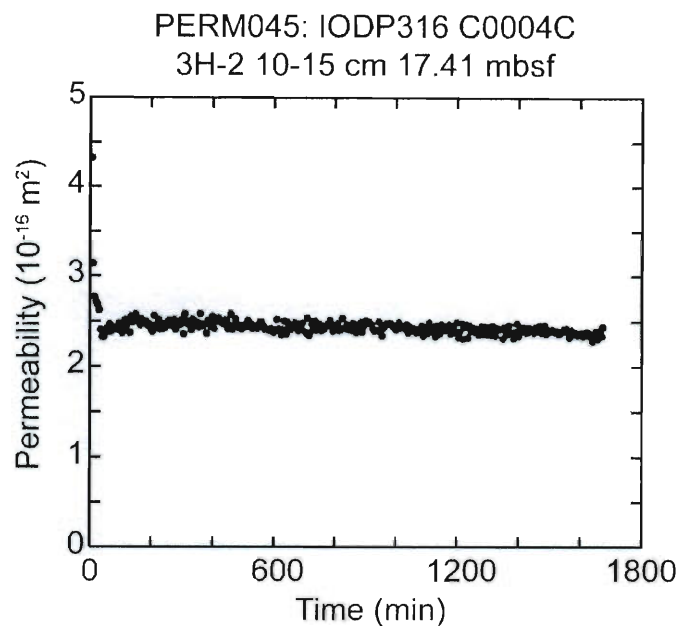
Figure A.2. Example data from flow-through permeability measurement. The pressure gradient across the sample is ramped up from 0 to the specified value over the first 30 minutes of the test. After this, the test is run for at least 24 hours to ensure that a steady-state permeability value is reached. Reported permeability values are the determined as the mean of the steady-state data. Reported errors are the standard deviation of the steady-state data. In this test the pressure gradient was 0.561 MPa m^{-1} and the permeability was determined to be $2.43 \pm 0.05 \times 10^{-16}$ m^2.

IODP316 C0004C 3H-2 10-15 cm 17.41 mbsf
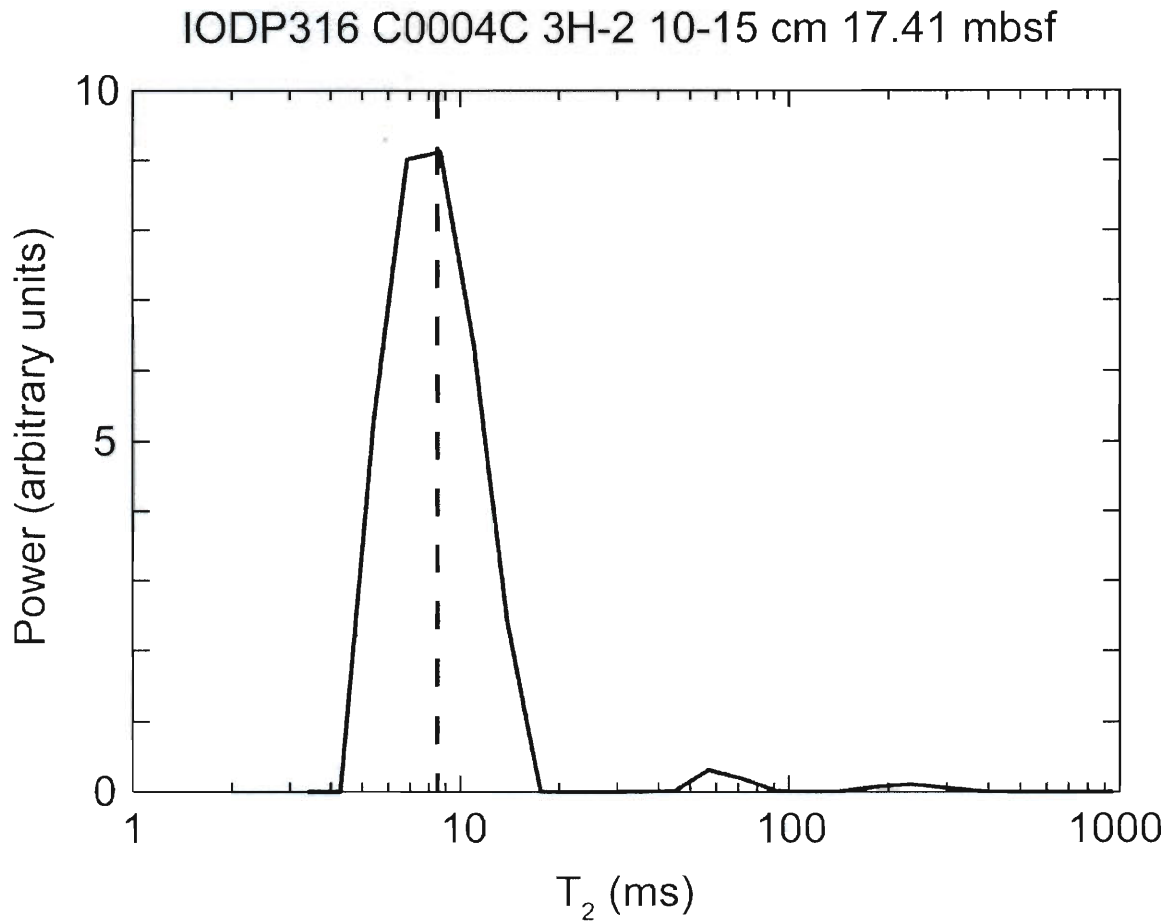
Figure A.3. Example T_2 distribution. T_2 is plotted on a logarithmic scale against the relative contribution each T_2 value makes to the total signal. T_{2LM} is the geometric mean of this distribution. For this sample, T_{2LM} = 8.7 ms (vertical dashed line).

Appendix B: Derivation of critical time for fracture generation

The partial derivative of λ^* with respect to time can be expanded according to the chain rule:

$$\frac{\partial \lambda^*}{\partial t} = \frac{\partial S_h}{\partial t} \frac{\partial \lambda^*}{\partial S_h} = \frac{\partial S_h}{\partial t} \left(\frac{\partial P^*}{\partial S_h} \frac{\partial \lambda^*}{\partial P^*} + \frac{\partial \sigma_v'}{\partial S_h} \frac{\partial \lambda^*}{\partial \sigma_v'} \right). \qquad \text{(Equation B1)}$$

The partial derivatives of overpressure and vertical effective stress with respect to S_h are

$$\frac{\partial P^*}{\partial S_h} = \int_0^z \frac{-2|\vec{q}|_f \mu_w}{k(1-S_h)^3} dz', \qquad \text{(Equation B2)}$$

$$\frac{\partial \sigma_v'}{\partial S_h} = g(\rho_h - \rho_w) \int_0^z \varphi dz' = g(\rho_h - \rho_w)[\varphi_\infty z + B(\varphi_0 - \varphi)]. \qquad \text{(Equation B3)}$$

The partial derivatives of λ^* with respect to P^* and σ_v' are

$$\frac{\partial \lambda^*}{\partial P^*} = \frac{1}{\sigma_v'}, \qquad \text{(Equation B4)}$$

$$\frac{\partial \lambda^*}{\partial \sigma_v'} = -\frac{P^*}{\sigma_v'^2} = -\frac{\lambda^*}{\sigma_v'}. \qquad \text{(Equation B5)}$$

We then approximate the partial derivatives with respect to S_h as their values when $S_h = 0$, so Equation B2 becomes

$$\frac{\partial P^*}{\partial S_h} = \int_0^z \frac{-2|\vec{q}|_f \mu_w}{k} dz' = 2P^*,$$

(Equation B6)

and Equation B5 becomes

$$\frac{\partial \lambda^*}{\partial \sigma_v'} = -\frac{\lambda^*}{g(\rho_s z + (\rho_w - \rho_s)(\varphi_\infty z + B(\varphi_0 - \varphi)))}.$$

(Equation B7)

Combining Equations B3, B4, B6, and B7, we can re-express Equation B1 as

$$\frac{\partial \lambda^*}{\partial t} = \frac{\partial S_h}{\partial t} \lambda^* \left(2 - \frac{(\rho_h - \rho_w)(\varphi_\infty z + B(\varphi_0 - \varphi))}{\rho_s z + (\rho_w - \rho_s)(\varphi_\infty z + B(\varphi_0 - \varphi))} \right),$$

(Equation B8)

which we simplify by assuming that $\lambda^* \ll \sigma_v'$:

$$\frac{\partial \lambda^*}{\partial t} = 2\lambda^* \frac{\partial S_h}{\partial t}.$$

(Equation B9)

We approximate the partial derivative of S_h with respect to time as the advective terms of Equation 4.1:

$$\frac{\partial S_h}{\partial t} = \frac{-\left|\vec{q}\right|_f \rho_w \frac{\partial c_m^l}{\partial z}}{\varphi\left(\rho_h c_m^h - \rho_w c_m^l\right)}.$$

(Equation B10)

Combining Equations B9 and B10 yields Equation 4.8.

Appendix C: MATLAB code used for Chapter 4

This MATLAB code is translated from the original FORTRAN code from

Bhatnagar et al. (2007). The mass balance equations are solved explicitly using a forward

in time, centered in space (FTCS) scheme (Fletcher, 1997). Methane solubility is

computed in two separate programs, total_solubility and liquid_vapor_solubility. The

code for these programs is appended after the main code.

```matlab
% Main program
% This is a Matlab version of Gaurav Bhatnagar's 1-D Fortran code
% set domain, time and depth steps
clear all
base = 550; %in meters
depth_step = 5; %in meters
dt = 5; %in years
maxiter = 10000000;
t_final = dt*maxiter % in years
% make depth vector
dz=depth_step*ones(1,base/depth_step+1);
depth=cumsum(dz)-dz(1);
% set environmental parameters
T0 = 276; %seafloor temp (K)
d0 = 1000; %seafloor depth (m)
G = 0.04; %geothermal gradient (K/m)
qf = 10; %fluid flux (mm/yr)
mNa = 0.6; % inital salt concentration (molality)
cm_ext = 1; % methane concentration in external flux w.r.t maximum
solubility
chlorides = (mNa*0.05844247)/(1+(mNa*0.05844247));
% set sediment physical properties
por = 0.5.*ones(1,length(depth));
perm = 1e-15.*ones(1,length(depth));
perm(28)=1e-15;
perm(29)=1e-15;
phi_0 = 0.63;
phi_inf = 0.1;
B = 1100; % porosity-depth constant
C = 13.05; % these are the perm function constants
D = -40.19; % k = exp(C*phi + D)
rhos = 2700; % grain density in kg/m^3
% global parameters
rhow = 1024;
g = 9.80665;
muw = 0.000887;
```

```matlab
rhoh = 930;
cmh = 0.134;
cmg = 1;
Dm = 1e-9;
Dc = 1e-9;
% compute porosity and permeability
%por = phi_inf + ((phi_0-phi_inf)*exp(-depth./B));
por_end = phi_inf + ((phi_0-phi_inf)*exp(-
(depth(length(depth))+(dz(length(depth))/2))/B));
dpordz = (phi_inf-por)./B;
%perm = exp((C.*por)+D);
clear B
clear C
clear D
% make temperature and pressure vectors
T = T0 + (depth.*G); %in K
P_inc = (qf*0.001*muw*dz.*1e-6)./(perm.*365*24*3600);
P = (cumsum(P_inc))+((depth+d0).*rhow*g*1e-6); %in MPa
P0 = d0*rhow*g*1e-6;
% find base of MHSZ and compute solubility curve
total_solubility
Lt
% compute necessary spatial derivatives
for i=1:length(cm_hyd)-1
    dcm_hyddz(i) = (cm_hyd(i+1)-cm_hyd(i))/dz(i);
end
dcm_hyddz(length(cm_hyd)) = 0;
for i=1:length(cm_hyd)-1
    d2cm_hyddz = (dcm_hyddz(i+1)-dcm_hyddz(i))/dz(i);
end
d2cm_hyddz(length(cm_hyd)) = 0;
d_space_dz = dpordz;
% make all the dimensionless groups
por_dim = (por-phi_inf)./(1-phi_inf);
gamma = (1-phi_inf)/phi_inf;
dz_dim = dz./Lt;
dt_dim = (dt*365*24*3600)*(Dm/(Lt^2));
cm_hyd_dim = cm_hyd./(max(cm_hyd));
rhoh_dim = rhoh/rhow;
cmh_dim = cmh/max(cm_hyd);
Pe2 = -((qf*0.001)/(365*24*3600))*(Lt/Dm);
por_end_dim = (por_end-phi_inf)/(1-phi_inf);
% initialize Sh, Sg, and salt matrices
Sh = zeros(length(depth),1);
Sg = zeros(length(depth),1);
Sh_new = zeros(length(depth),1);
Sg_new = zeros(length(depth),1);
cml_new = zeros(length(depth),1);
ccl = chlorides.*(ones(length(depth),1));
for i=1:length(depth)
    if depth(i)<Lt
        cml(i)=0;
    else
        cml(i)=cm_hyd(i);
    end
end
cml(length(depth))=cm_ext*max(cm_hyd);
```

```matlab
cml_dim=cml./(max(cm_hyd));
dshdt = zeros(length(depth),1);
dsgdt = zeros(length(depth),1);
% initialize coefficient matrices
for i=1:length(depth)
    if cml(i)>0
        Uf(i)=-1;
    else
        Uf(i)=-1;
    end
end
ddt = zeros(length(depth),1);
iter = 0;
% calculation loop
while iter<maxiter
    for i=1:length(depth)
        if cml(i)<cm_hyd(i)
            if T(i)<T3P(i)
                if i==1
                    f1(i) =
(abs(Pe2))*(1+gamma)*dt_dim*((Uf(i)*cml_dim(i+1))-
(Uf(i)*cml_dim(i)))/((1+por_dim(i))*dz_dim(i));
                    dflux(i) = (dt_dim/(1+por_dim(i)))*(
(1+((por_dim(i+1)+por_dim(i))/2))*(1-(Sh(i+1)/2))*(cml_dim(i+1)-
cml_dim(i))/(dz_dim(i)*dz_dim(i)) -
(1+por_dim(i))*cml_dim(i)*2/(dz_dim(i)*dz_dim(i)) );
                    cml_new(i) = (cml_dim(i) - f1(i) +
dflux(i))*max(cm_hyd);
                else
                    f1(i) =
(((abs(Pe2)))*(1+gamma)*dt_dim/((1+por_dim(i))*dz_dim(i)))*(
(Uf(i+1)*cml_dim(i+1)) - (Uf(i)*cml_dim(i)) );
                    dflux(i) = (dt_dim/(1+por_dim(i)))*(
(1+((por_dim(i+1)+por_dim(i))/2))*(1-(Sh(i+1)/2))*(cml_dim(i+1)-
cml_dim(i))/(dz_dim(i)*dz_dim(i)) - (1+((por_dim(i-
1)+por_dim(i))/2))*(1-(Sh(i-1)/2))*(cml_dim(i)-cml_dim(i-
1))/(dz_dim(i)*dz_dim(i)) );
                    cml_new(i) = (cml_dim(i) - f1(i) +
dflux(i))*max(cm_hyd);
                end
                if cml_new(i)>cm_hyd(i)
                    Sh_new(i)=((cml_new(i)-
cm_hyd(i))/(max(cm_hyd)))/(cmh_dim*rhoh_dim-cm_hyd_dim(i));
                    cml_new(i)=cm_hyd(i);
                end
            elseif T(i)>=T3P(i)
                if i==length(depth)
                    f1(i) =
((abs(Pe2))*(1+gamma)*dt_dim/((1+por_dim(i))*dz_dim(i)))*( Uf(i)*cm_ext
- Uf(i)*cml_dim(i) );
                    dflux(i) = (dt_dim/(1+por_dim(i)))*(
1*(1+por_end_dim)*(cm_ext-cml_dim(i))/(dz_dim(i)*dz_dim(i)) -
(1+((por_dim(i-1)+por_dim(i))/2))*(1-(Sg(i-1)/2))*(cml_dim(i)-
cml_dim(i-1))/(dz_dim(i)*dz_dim(i)) );
                    cml_new(i) = (cml_dim(i) - f1(i) +
dflux(i))*max(cm_hyd);
                else
```

```
                        f1(i) =
((abs(Pe2))*(1+gamma)*dt_dim/((1+por_dim(i))*dz_dim(i)))*((
Uf(i+1)*cml_dim(i+1) - Uf(i)*cml_dim(i) - 0*0*(1+((por_dim(i-
1)+por_dim(i))/2))*(cmg/max(cm_hyd))*Sg(i-1)*(rhog(i-
1)/rhow))/((abs(Pe2))*(gamma-((por_dim(i-1)+por_dim(i))/2))) -
0*0*(1+((por_dim(i-1)+por_dim(i))/2))*cmh_dim*Sh(i-
1)*rhoh_dim/((abs(Pe2))*(gamma-((por_dim(i-1)+por_dim(i))/2))) );
                        dflux(i) = (dt_dim/(1+por_dim(i)))*(
(1+((por_dim(i+1)+por_dim(i))/2))*(1-(Sg(i+1)/2))*(cml_dim(i+1)-
cml_dim(i))/(dz_dim(i)*dz_dim(i)) - (1+((por_dim(i-
1)+por_dim(i))/2))*(1-((Sh(i-1)+Sg(i-1))/2))*(cml_dim(i)-cml_dim(i-
1))/(dz_dim(i)*dz_dim(i)) );
                        cml_new(i) = (cml_dim(i) - f1(i) +
dflux(i))*max(cm_hyd);
                    end
                    if cml_new(i)>cm_hyd(i)
                        Sg_new(i) = ((cml_new(i)-
cm_hyd(i))/(max(cm_hyd)))/((cmg/max(cm_hyd))*(rhog(i)/rhow)-
cm_hyd_dim(i));
                        cml_new(i)=cm_hyd(i);
                    end
                end
            elseif cml(i)==cm_hyd(i)
                if T(i)<T3P(i)
                    const1(i) = -(1+por_dim(i))*cm_hyd_dim(i) + (
(1+por_dim(i))*(1-Sh(i))*cm_hyd_dim(i) +
(1+por_dim(i))*Sh(i)*cmh_dim*rhoh_dim );
                    const2(i) = -(abs(Pe2))*(1+gamma)*(dt_dim/dz_dim(i))*(
Uf(i+1)*cml_dim(i+1) - Uf(i)*cm_hyd_dim(i) );
                    const4(i) = dt_dim*(
(1+((por_dim(i+1)+por_dim(i))/2))*(1-
(Sh(i+1)+Sg(i+1)+Sh(i))/2)*(cml_dim(i+1)-
cm_hyd_dim(i))/(dz_dim(i)*dz_dim(i))-(1+((por_dim(i-
1)+por_dim(i))/2))*(1-(Sh(i)+Sh(i-1))/2)*(cm_hyd_dim(i)-cml_dim(i-
1))/(dz_dim(i)*dz_dim(i)) );
                    const6(i) = (1+por_dim(i))*(cmh_dim*rhoh_dim-
cm_hyd_dim(i));
                    Sh_new(i) = (const1(i) + const2(i) +
const4(i))/const6(i);
                    cml_new(i)=cm_hyd(i);
                elseif T(i)>=T3P(i)
                    const1(i) = -(1+por_dim(i))*cm_hyd_dim(i) + (
(1+por_dim(i))*(1-Sg(i))*cm_hyd_dim(i) +
(1+por_dim(i))*Sg(i)*(cmg/max(cm_hyd))*(rhog(i)/rhow) );
                    if i==length(depth)
                    const2(i) = -
(abs(Pe2))*(1+gamma)*(dt_dim/dz_dim(i))*( Uf(i)*cm_ext -
Uf(i)*cm_hyd_dim(i) );
                    const4(i) = dt_dim*( (1+por_dim(i))*(1-(Sg(i)+Sg(i-
1))/2)*1*(cm_ext-cm_hyd_dim(i))/(dz_dim(i)*dz_dim(i))- (1+((por_dim(i-
1)+por_dim(i))/2))*(1-(Sg(i)+ Sh(i-1) +Sg(i-1))/2)*(cm_hyd_dim(i)-
cml_dim(i-1))/(dz_dim(i)*dz_dim(i)) );
                    else
                    const2(i) = -
(abs(Pe2))*(1+gamma)*(dt_dim/dz_dim(i))*( Uf(i+1)*cml_dim(i+1) -
Uf(i)*cm_hyd_dim(i) );
```

```matlab
                const4(i) = dt_dim*(
(1+((por_dim(i+1)+por_dim(i))/2))*(1-(Sg(i+1)+Sg(i))/2)*(cml_dim(i+1)-
cm_hyd_dim(i))/(dz_dim(i)*dz_dim(i))- (1+((por_dim(i-
1)+por_dim(i))/2))*(1-(Sg(i)+Sh(i-1) + Sg(i-1))/2)*(cm_hyd_dim(i)-
cml_dim(i-1))/(dz_dim(i)*dz_dim(i)) );
                end
                const6(i) =
(1+por_dim(i))*(((cmg/max(cm_hyd))*(rhog(i)/rhow))-cm_hyd_dim(i));
                Sg_new(i) = (const1(i) + const2(i) +
const4(i))/const6(i);
                cml_new(i) = cm_hyd(i);
            end
        end
    end
    % clean up vectors
    for i=1:length(depth)
        if Sg_new(i)<0
            Sg_new(i)=0;
        elseif Sh_new(i)<0
            Sh_new(i)=0;
        else
            Sg_new(i)=Sg_new(i);
            Sh_new(i)=Sh_new(i);
        end
    end
    cml_new(1)=0;
    cml_new(length(depth))=cm_ext*max(cm_hyd);
    Sg_new(length(depth)-1)=0;
    ccl_new=chlorides./(1-Sh_new);
    % make the time derivative vectors
    ddt = ((1-Sh_new-Sg_new)-(1-Sh-Sg))./(dt*24*365*3600);
    dshdt = (Sh_new-Sh)./(dt*24*365*3600);
    dsgdt = (Sg_new-Sg)./(dt*24*365*3600);
    for i=1:length(depth)-1
        d_space_dz(i)=((por(i+1)*(1-Sh_new(i+1)-Sg_new(i+1)))-
(por(i)*(1-Sh_new(i)-Sg_new(i))))/dz(i);
    end
    d_space_dz(length(depth))=dpordz(length(depth));
    % switch the vectors
    Sh=Sh_new;
    Sg=Sg_new;
    cml=cml_new;
    cml_dim=cml./max(cm_hyd);
    ccl=ccl_new;
    % compute new perm and pressures
    for i=1:length(Sh)
        perm_new(i)=perm(i)*((1-Sh(i))^2);
    end
    for i=1:length(Sh)
        ob_inc(i)=(((1-por(i))*rhos)+(por(i)*(1-Sh(i)-
Sg(i))*rhow)+(por(i)*Sh(i)*rhoh)+(por(i)*Sg(i)*rhog(i)))*g*dz(i)*1e-6;
        pp_inc(i)=(qf*0.001*muw*dz(i)*1e-6)/(perm_new(i)*365*24*3600);
    end
    ob=cumsum(ob_inc);
    pp=cumsum(pp_inc);
    lambda_star=pp./(ob-(depth.*rhow*g*1e-6));
    if max(lambda_star)>0.6
```

```matlab
        break
    end
    iter=iter+1;
end
% compute heave force
dT = T(2)-T(1);
prod = por'.*Sh.*dT;
for i=1:count
    new_prod(i)=prod((count+1)-i);
end
int=cumsum(new_prod);
for j=count+1:length(prod)
    int(j)=int(count);
end
heave_force = (T3P-T-int).*((rhoh.*5.47e5)./T3P);
H_star = (heave_force*1e-6)./(ob-(depth.*rhow*g*1e-6));
for i=1:length(depth)-1
    if H_star(i)>0.6
        if H_star(i+1)<0.6
            H_bot=i-1;
        end
    end
end
H_rat=depth(H_bot)/Lt
for i=1:length(Sh)
        ob_inc(i)=(((1-por(i))*rhos)+(por(i)*rhow))*g*dz(i)*1e-6;
        pp_inc(i)=(qf*0.001*muw*dz(i)*1e-6)/(perm(i)*365*24*3600);
end
ob=cumsum(ob_inc);
pp=cumsum(pp_inc);
lambda_star_org=pp./(ob-(depth.*rhow*g*1e-6));
iter*dt
figure
subplot(1,5,1)
plot(Sh,depth)
set(gca,'YDir','reverse')
xlabel('Sh')
ylabel('Depth (mbsf)')
subplot(1,5,2)
plot(por,depth)
set(gca,'YDir','reverse')
xlabel('Porosity')
subplot(1,5,3)
semilogx(perm,depth,'--k',perm_new,depth,'-k')
set(gca,'YDir','reverse')
xlabel('Permeability (m2)')
subplot(1,5,4)
plot(lambda_star_org,depth,'--k',lambda_star,depth,'-k')
set(gca,'YDir','reverse')
xlabel('l*')
subplot(1,5,5)
plot(H_star,depth)
set(gca,'YDir','reverse')
xlabel('H*')
```

```
% Program total_solubility
% Determines thickness of MHSZ and computes solubility curve
% using program liquid_vapor_solubility
% iterate to find base of MHSZ
T_try = 0;
P_try = 0;
rhog = 0;
Salt = 100*((mNa*0.05844247)/(1+(mNa*0.05844247)));
cm_triplept = 0;
a1 = 258.4719097;
a2 = 16.54979759;
a3 = -0.20037934;
a4 = -2.51786785;
a5 = -8.31210883e-2;
a6 = 2.90289187e-2;
a7 = 0.24786712;
a8 = 5.07299816e-3;
a9 = -1.17856658e-3;
a10 = -8.27706806e-3;
d = 100;
T3P = a1 + (a2*log(P0+1e-2*d)) + (a3*Salt) + (a4*(log(P0+1e-2*d))^2) +
(a5*(Salt^2)) + (a6*(log(P0+1e-2*d))*Salt) + (a7*(log(P0+1e-2*d))^3) +
(a8*(Salt)^3) + (a9*log(P0+1e-2*d)*(Salt)^2) + (a10*Salt*(log(P0+1e-
2*d))^2);
fz = T0 + (G*d) - T3P;
norm2 = abs(fz);
norm1 = 1e6;
while norm1>1e-8 && norm2>1e-8
    dfdz = G - (1e-2/(P0+1e-2*d))*(a2 + 2*a4*log(P0+1e-2*d) + a6*Salt +
3*a7*(log(P0+1e-2*d))^2 +  a9*(Salt)^2 + 2*a10*Salt*log(P0+1e-2*d));
    dnew = d - (fz/dfdz);
    norm1 = abs(d-dnew);
    T3P = a1 + a2*log(P0+1e-2*dnew) + a3*Salt + a4*(log(P0+1e-
2*dnew))^2 + a5*(Salt^2) + a6*(log(P0+1e-2*dnew))*Salt+a7*(log(P0+1e-
2*dnew))^3 + a8*(Salt)^3 + a9*log(P0+1e-2*dnew)*(Salt)^2 +
a10*Salt*(log(P0+1e-2*dnew))^2;
    fz = T0 + (G*dnew) - T3P;
    norm2 = abs(fz);
    d = dnew;
end
% set base of MHSZ
Lt = dnew;
% compute temp at base of MHSZ
Teq = T0 + (G*dnew);
% compute L-V solubility profile
liquid_vapor_solubility;
LV_sol = sol;
clear T
T3P = 1./(-3.6505e-6.*(log(P)).^3+3.704e-5.*(log(P)).^2 -
0.00021948.*log(P) + 0.0038494);
T=T3P;
liquid_vapor_solubility;
LH_sol = sol;
clear T
T = T0 + (depth.*G);
% inside the MHSZ, compute solubility from Buffett's expression
% below MHSZ, use L-V solubility
```

```
for i=1:length(depth)
    if T(i)>Teq
        cm_eq(i)=LV_sol(i);
    else
        cm_eq(i)=LH_sol(i)*exp((T(i)-T3P(i))/15.3);
    end
end
% smooth the solubility curve at the base of MHSZ
count=length(depth)-(round((Lt/(max(depth)))*(length(depth))));
corr=abs(cm_eq(count)-cm_eq(count+1));
for i=1:length(depth)
    if T(i)<Teq
        cm_eq(i)=cm_eq(i)+corr;
    else
        cm_eq(i)=cm_eq(i);
    end
end
% convert to mass fraction
for i=1:length(depth)
    if T(i)<Teq
        cm_hyd(i) = (16.*cm_eq(i))./(18 - (2.*cm_eq(i)));
    else
        cm_hyd(i) = (16.*max(cm_eq))./(18 - (2.*max(cm_eq)));
    end
end
% compute gas density from ideal gas law
rhog = 1000*(P.*16)./(8.314.*T);
% compute gas viscosity from Lennard-Jones parameters
mug =
(((16.*T).^0.5)./(((2.44.*((T3P./(P.*9.86923267)).^(1/3))).^2).*1.401))
.*2.6693e-6;




% Program liquid_vapor_solubility
% Method of Bhatnagar et al. (2007)
% Water properties
Tcw = 647.14; %K
Pcw = 22.064; %MPa
rho_cw = 322; %kg/m^3
% Methane properties
Tcm = 190.56; %K
Pcm = 4.599; %MPa
w = 0.0115; %Acentric factor
MW = 16; %Molar weight of methane
R = 8.314; %Ideal gas constant
% Saul & Wagner (1987) vapor pressure of water
a1 = -7.85823;
a2 = 1.83991;
a3 = -11.7811;
a4 = 22.6705;
a5 = -15.9393;
a6 = 1.77516;
tau = 1-(T./Tcw);
var1 = (a1.*tau) + (a2.*(tau.^1.5)) + (a3.*(tau.^3)) + (a4.*(tau.^3.5))
+ (a5.*(tau.^4)) + (a6.*(tau.^7.5));
% Vapor pressure in MPa
```

```matlab
Pwsat = Pcw.*(exp((var1.*Tcw)./T));
deltat = 1e-5;
taudt = 1 - ((T+deltat)./Tcw);
var1 = (a1.*taudt) + (a2.*(taudt.^1.5)) + (a3.*(taudt.^3)) +
(a4.*(taudt.^3.5)) + (a5.*(taudt.^4)) + (a6.*(taudt.^7.5));
var2 = (var1.*Tcw)./(T+deltat);
% Vapor pressure at T+dt in MPa
Pwsatdt = Pcw.*exp(var2);
dpdt = (Pwsatdt-Pwsat)./deltat;
dpdt = dpdt.*1e6;
% Reduced variables in terms of critical methane properties
Trm = T./Tcm;
Prm = P./Pcm;
% Equation of state parameters for a pure component
m = 0.37464 + (1.54226*w) - (0.26992*(w^2));
alfa = (1 + (m.*(1-(Trm.^0.5)))).^2;
a1 = 0.45724*((R.*Tcm)^2).*alfa./(Pcm.*1e6);
b1 = 0.0778*R.*Tcm./(Pcm.*1e6);
A = a1.*P.*1e6./(R.*T).^2;
B = b1.*P.*1e6./(R.*T);
% Coefficients of the cubic in z
a1 = -1.*(1 - B);
a2 = A - (3.*(B.^2)) - (2.*B);
a3 = -((A.*B) - (B.^2) - (B.^3));
q = ((3.*a2) - (a1.^2))./9;
j = ((9.*a1.*a2) - (27.*a3) - (2.*(a1.^3)))./54;
det = (q.^3) + (j.^2);
% Find the roots
for i=1:length(det)
if det(i)>0
    z(i) = (j(i)+(det(i).^0.5)).^(1/3) + (j(i)-(det(i).^0.5)).^(1/3) -
a1(i)./3;
elseif det(i)<0
    ang = acos(j(i)./((-(q(i).^3)).^0.5));
    z1 = 2.*((-q(i)).^0.5).*cos(ang./3) - a1(i)./3;
    z2 = 2.*((-q(i)).^0.5).*cos(ang./3 + 2.09439513) - a1(i)./3;
    z3 = 2.*((-q(i)).^0.5).*cos(ang./3 + 4.18879027) - a1(i)./3;
    z(i) = max([z1 z2 z3]);
else
    z1 = 2.*(j(i).^(1/3)) - a1(i)./3;
    z2 = -(j(i).^(1/3)) - a1(i)/3;
    z(i) = max([z1 z2]);
end
end
% Compute fugacity
phi = exp(z - 1 - log(z-B) - A./(2.*B*(2^0.5)).*log((z + (1 +
(2^0.5)).*B)./(z + (1 - (2^0.5)).*B)));
% Duan's EoS parameters
Pbar = P.*10;
% Chemical potential parameters
m1 = 4.30210345e1;
m2 = -6.83277221e-2;
m3 = -5.68718730e3;
m4 = 3.56636281e-5;
m5 = -5.79133791e1;
m6 = 6.11616662e-3;
m7 = -7.85528103e-4;
```

```
m8 = -9.42540759e-2;
m9 = 1.92132040e-2;
m10 = -9.17186899e-6;
% Binary iteraction paramter CH4-Na
bb1 = 9.92230792e-2;
bb2 = 2.57906811e-5;
bb8 = 1.83451402e-2;
bb10 = -8.07196716e-6;
% Ternary interaction parameter CH4-Na-Cl
t1 = -6.23943799e-3;
mu = m1 + (m2.*T) + (m3./T) + (m4.*(T.^2)) + (m5./(680-T)) + (m6.*Pbar)
+ (m7.*Pbar.*log(T)) + (m8.*Pbar./T) + (m9.*Pbar./(680-T)) +
(m10.*Pbar.*Pbar./T);
lambda = bb1 + (bb2.*T) + (bb8.*Pbar./T) + (bb10.*Pbar.*Pbar./T);
ksi = t1;
y_CH4 = (P-Pwsat)./P;
log_m_CH4 = log(y_CH4.*Pbar.*phi) - mu - (2.*lambda.*mNa) +
(0.00624.*mNa.*mNa);
molality = exp(log_m_CH4);
sol = molality./(molality+(1000/18));
```

Appendix D: MATLAB code used for Chapter 5

This code incorporates multiphase flow and a constant pressure basal boundary

condition. Salt mass balance is computed implicitly, and methane mass balance is

computed explicitly. All mass balances are solved using a forward in time, centered in

space (FTCS) scheme (Fletcher, 1997). Methane solubility is computed using the same

subroutines as in Appendix C.

```
clear all
dz=10;
dt=0.005;
maxiter=1e10;
depth=[910:-dz:0];
por=0.05+((0.75-0.05).*exp(-depth./1600));
perm=exp((1.5.*por)-36);
%por=0.1+((0.63-0.1).*exp(-depth./1400));
%perm=exp((13.*por)-40);
%por=0.5*ones(length(depth),1);
%perm=1e-15*ones(length(depth),1);
t_final = maxiter*dt
% set environmental parameters
pw0 = 4000000; %water overpressure at base of domain (Pa)
T0 = 276.4; %seafloor temp (K)
d0 = 2781; %seafloor depth (m)
G = 0.04; %geothermal gradient (K/m)
mNa = 0.593; % inital salt concentration (molality)
cm_ext = 1; % methane concentration in external flux w.r.t maximum
solubility
Sgmin = 0.1; %minimum gas saturation for flow of free gas phase
chlorides = (mNa*0.05844247)/(1+(mNa*0.05844247));
% global parameters
rhow = 1024;
rhos = 2700;
g = 9.80665;
muw = 0.000887;
rhoh = 930;
cmh = 0.134;
Dm = 1e-9;
Dc = 1e-9;
% make temperature and pressure vectors
T = T0 + (depth.*G); %in K
P = (depth+d0).*rhow*g*1e-6; %in MPa
P0 = d0*rhow*g*1e-6;
% find triple point salt concentration
```

```
salt_eq
% find base of MHSZ and compute solubility curve
total_solubility
Lt
cml=zeros(length(depth),1);
cmg=zeros(length(depth),1);
cml_new=zeros(length(depth),1);
cmg_new=zeros(length(depth),1);
Sg=zeros(length(depth),1);
Sg_new=zeros(length(depth),1);
cml(length(depth))=0;
if pw0>0
    cml(1)=cm_ext*max(cm_hyd);
else
    cml(1)=0;
end
cmg(length(depth))=0;
cmg(1)=1;
ccl=chlorides.*ones(length(depth),1);
Sh=zeros(length(depth),1);
Sh_new=zeros(length(depth),1);
krelw = ones(length(depth),1);
krelg = 0.001*ones(length(depth),1);
qg = zeros(length(depth),1);
qw = zeros(length(depth),1);
iter=0;
while iter<maxiter
    for i=2:length(depth)-1
        cml_new(i)=((1-
((qw(i)*0.001*dt)/(por(i)*dz)))*cml(i))+(((qw(i)*0.001*dt)/(por(i)*dz))
*cml(i-1));
        cmg_new(i)=((1-((qg(i-1)*0.001*dt)/(dz)))*cmg(i))+(((qg(i-
1)*0.001*dt)/(dz))*cmg(i-1));
    end
    cml_new(1)=cml(1);
    cml_new(length(depth))=0;
    cmg_new(1)=1;
    cmg_new(length(depth))=0;
    for i=1:length(depth)
        if T(i)<T3P(i)
            cmg_new(i)=0;
        else
            cmg_new(i)=cmg_new(i);
        end
    end
    % explicit FTCS scheme for hydrate & gas formation
    for i=1:length(depth)
        if cml_new(i)>cm_hyd(i)
            if T(i)>=T3P(i)
                if cmg_new(i)>0
                    if Sg(i)<=Sgmin
                        Sg_new(i) =
Sg(i)+(cmg_new(i)/(rhog(i)*por(i)));
                    else
                        Sg_new(i) = max([Sg(i)
(cmg_new(i)/(rhog(i)*por(i)))]);
                    end
```

```
                    Sh_new(i) = Sh(i);
                else
                    Sg_new(i)=Sg(i);
                    Sh_new(i)=Sh(i);
                end
            else
                Sh_new(i)= Sh(i)+((cml_new(i)-cm_hyd(i))*((rhow*(1-
Sh(i)))/((rhoh*cmh)-(rhow*cm_hyd(i))))));
                cml_new(i)=cm_hyd(i);
            end
        elseif cml_new(i)==cm_hyd(i)
            if T(i)>=T3P(i)
                if cmg_new(i)>0
                    if Sg(i)<=Sgmin
                        Sg_new(i) =
Sg(i)+(cmg_new(i)/(rhog(i)*por(i)));
                    else
                        Sg_new(i) = max([Sg(i)
(cmg_new(i)/(rhog(i)*por(i)))]);
                    end
                    Sh_new(i) = Sh(i);
                else
                    Sg_new(i)=Sg(i);
                    Sh_new(i)=Sh(i);
                end
            else
                Sh_new(i) = Sh(i)+(((dt*0.001)/dz)*(
((qw(i)*rhow*(cml_new(i)-cml_new(i-1))))/(por(i)*((rhoh*cmh)-
(rhow*cml_new(i))))));
            end
        else
            if T(i)>=T3P(i)
                if cmg_new(i)>0
                    if Sg(i)<=Sgmin
                        Sg_new(i) =
Sg(i)+(cmg_new(i)/(rhog(i)*por(i)));
                    else
                        Sg_new(i) = max([Sg(i)
(cmg_new(i)/(rhog(i)*por(i)))]);
                    end
                    Sh_new(i) = Sh(i);
                else
                    Sg_new(i)=Sg(i);
                    Sh_new(i)=Sh(i);
                end
            else
                Sh_new(i) = Sh(i)+(((dt*0.001/dz)*(qg(i-
1)*rhog(i)*(cmg_new(i-1)-cmg_new(i))))/(por(i)*rhoh*cmh));
                cmg_new(i)=0;
                Sg_new(i)=0;
            end
        end
        if Sg_new(i)<Sg(i)
            Sg_new(i)=Sg(i);
        else
            Sg_new(i)=Sg_new(i);
        end
```

```
        if Sh_new(i)<0
            Sh_new(i)=Sh(i);
        else
            Sh_new(i)=Sh_new(i);
        end
    end
    % check to see if saturations are reasonable
    if max(Sh_new)>1
        break
    elseif max(Sg_new)>1
        break
    end
    % if salinity has dropped below triple point conditions, remove any
gas
    for i=1:length(depth)
        if T(i)<T3P(i)
            Sh_new(i)=Sh_new(i)+((Sg(i)*rhog(i))/rhoh);
            Sg_new(i)=0;
        end
    end
    % compute new salinity
    for i=2:length(depth)-1
        ccl_new(i)= (((dt*qw(i)*0.001)/(2*dz*por(i)))*(ccl(i+1)-ccl(i-
1))) + (((Dc*dt*24*365*3600*(1-Sh(i)))/(dz*dz))*(ccl(i+1)+ccl(i-1)-
2*ccl(i))) + (((dt*Dc*24*365*3600)/(2*dz*por(i)))*(ccl(i+1)-ccl(i-
1))*((por(i+1)*(1-Sh(i+1)))-(por(i-1)*(1-Sh(i-1))))) + (((1-Sh(i))/(1-
Sh_new(i)))*ccl(i));
            if(ccl_new(i))<=chlorides
                ccl_new(i)=chlorides;
            else
                ccl_new(i)=ccl_new(i);
            end
    end
    ccl_new(1)=chlorides;
    ccl_new(length(depth))=chlorides;
    for i=2:length(depth)
        dccldz(i)=(ccl_new(i)-ccl_new(i-1))/dz;
    end
    dccldz(1)=0;
    if pw0>0
        cml_new(1)=cm_ext*max(cm_hyd);
    else
        cml_new(1)=0;
    end
    cml_new(length(depth))=0;
    Sh_new(length(depth))=0;
    Sg_new(length(depth))=0;
    % compute new relative permeabilities
    for i=1:length(depth)
        krelg(i) = (((1-((1-Sg_new(i)-0.1)/(1-0.12)))^2)*(1-(((1-
Sg_new(i)-0.1)/(1-0.12))^2)))+(0.001*(1-Sg_new(i)));
        krelw(i) = ((1-Sg_new(i)-0.1)/(1-0.12))^4;
    end
    % find the uppermost point where Sg>0
    for i=1:length(depth)
        if Sg_new(i)>0
            if Sg_new(i+1)==0
```

```matlab
                gas_front=i;
            end
        end
    end
    % compute pressures
    for i=1:length(depth)
        ob_inc(i)=(g*dz*((rhow*por(i)*(1-Sh_new(i)-
Sg_new(i)))+(rhos*(1-
por(i)))+(rhoh*por(i)*Sh_new(i))+(rhog(i)*por(i)*Sg_new(i))))-
(dz*rhow*g);
        %Pc(i) =   (0.1770406+(0.0070157*((1-Sg_new(i))^-
4)))*0.072*(por(i)^0.5)*((perm(i)*(1-Sh_new(i)))^-0.5);
        Pc(i) = (0.5722*((1-Sg_new(i))^-
0.9244))*0.072*(por(i)^0.5)*((perm(i)*(1-Sh_new(i)))^-0.5);
    end
    sigv_eff=fliplr(cumsum(fliplr(ob_inc)));
    pw=(rhow.*g.*depth)+((pw0/depth(1)).*depth);
    pg=pw+Pc;
    pw_star=pw-(rhow.*g.*depth);
    pg_static=cumsum(rhog.*g.*dz);
    for i=2:length(depth)
        if Sg_new(i-1)>0
            pg(i)=pg(i);
            Pc(i)=Pc(i);
            pg_star(i)=pg(i)-(rhow*g*depth(i));
            lambda_star(i)=Pc(i)/(sigv_eff(i));
        else
            pg(i)=0;
            Pc(i)=0;
            pg_star(i)=0;
            lambda_star(i)=pw_star(i)/(sigv_eff(i));
        end
    end
    if max(lambda_star(count:length(depth)))>=1
        break
    end
    % compute the new triple point curve
    a1 = 258.4719097;
    a2 = 16.54979759;
    a3 = -0.20037934;
    a4 = -2.51786785;
    a5 = -8.31210883e-2;
    a6 = 2.90289187e-2;
    a7 = 0.24786712;
    a8 = 5.07299816e-3;
    a9 = -1.17856658e-3;
    a10 = -8.27706806e-3;
    for i=1:length(depth)
        T3P(i) = a1 + (a2*log(P0+1e-2*depth(i))) + (100*a3*ccl_new(i))
+ (a4*(log(P0+1e-2*depth(i)))^2) + (a5*((100*ccl_new(i))^2)) +
(a6*(log(P0+1e-2*depth(i)))*100*ccl_new(i)) + (a7*(log(P0+1e-
2*depth(i)))^3) + (a8*(100*ccl_new(i))^3) + (a9*log(P0+1e-
2*depth(i))*(100*ccl_new(i))^2) + (a10*100*ccl_new(i)*(log(P0+1e-
2*depth(i)))^2);
    end
    % compute effective permeability at each depth
    for i=1:length(depth)
```

```matlab
            keffw_term(i)=dz/(perm(i)*krelw(i)*((1-Sh_new(i))^2));
        end
        keffw=(depth(1)+dz)/sum(keffw_term);
        % compute fluxes
        for i=1:length(depth)-1
            if i<=gas_front
                if Sg_new(i)>=Sgmin
                    qg(i)=(((pg(i)-pg_static(i)-Pc(i))-(pg(i+1)-
pg_static(i+1)-Pc(i+1)))/dz)*((perm(i)*krelg(i)*((1-
Sh_new(i))^2))/mug(i))*1000*3600*24*365;
                else
                    qg(i)=0;
                end
            else
                qg(i)=0;
            end
            qw(i)=(pw0/depth(1))*(keffw/muw)*1000*3600*24*365;
        end
        qg(length(depth))=0;
        qw(length(depth))=0;
        for i=1:length(depth)
            salt_rat(i)=1-
((0.001*dt*qw(i)*dccldz(i))/(por(i)*ccl_new(i)*((1-Sh_new(i))-(1-
Sh(i)))));
            if isnan(salt_rat(i))==1
                salt_rat(i)=0;
            end
            if isinf(salt_rat(i))==1
                salt_rat(i)=0;
            end
        end
        %output vectors every 1000 steps
        if iter>0
            if rem(iter,1000)==0
                salinity(:,iter*0.001)=ccl_new;
                lstar(:,iter*0.001)=lambda_star;
                salt_ratio(:,iter*0.001)=salt_rat;
                salt_diff(:,iter*0.001)=ccl_new./eq_salt';
                sh_evolution(:,iter*0.001)=Sh_new;
                qw_evolution(:,iter*0.001)=qw;
                qg_evolution(:,iter*0.001)=qg;
            end
        end
        ccl=ccl_new;
        cml=cml_new;
        cmg=cmg_new;
        Sh=Sh_new;
        Sg=Sg_new;
        iter=iter+1;
end
iter*dt
time=[1000*dt:1000*dt:iter*dt];
for i=1:length(depth)
        ob_init_inc(i)=(g*dz*((rhow*por(i)*(1))+(rhos*(1-por(i)))))-
(dz*rhow*g);
end
sigv_eff_init=fliplr(cumsum(fliplr(ob_init_inc)));
```

```
lambda_star_init=pw_star./sigv_eff_init;
dldsalt(:,1)=(lstar(:,1)-lambda_star_init')./(salinity(:,1)-
chlorides.*ones(length(depth),1));
for i=2:length(time)
    dldsalt(:,i)=(lstar(:,i)-lstar(:,i-1))./(salinity(:,i)-
salinity(:,i-1));
end
figure
subplot(1,5,1)
plot(Sh,depth,Sg,depth)
set(gca,'YDir','reverse','YLim',[0 Lt])
xlabel('Saturation')
ylabel('Depth (mbsf)')
legend('Hydrate','Gas')
subplot(1,5,2)
plot(ccl,depth)
set(gca,'YDir','reverse','YLim',[0 Lt])
xlabel('Chlorides (kg/kg)')
subplot(1,5,3)
plot(por,depth)
set(gca,'YDir','reverse','YLim',[0 Lt])
xlabel('Porosity')
subplot(1,5,4)
semilogx(perm,depth)
set(gca,'YDir','reverse','YLim',[0 Lt])
xlabel('Perm (m^2)')
subplot(1,5,5)
plot(lambda_star,depth)
set(gca,'YDir','reverse','YLim',[0 Lt])
xlabel('lambda star')
figure
contourf(time,depth,salinity)
set(gca,'YDir','reverse','YLim',[0 Lt])
xlabel('Time (years)')
ylabel('Depth (mbsf)')
title('Salinity evolution')
colorbar
v=[0:0.1:1.1];
figure
contourf(time,depth,salt_diff,v)
set(gca,'YDir','reverse','YLim',[0 Lt])
xlabel('Time (years)')
ylabel('Depth (mbsf)')
title('Salt ratio')
colorbar
w=[0:0.1:2];
figure
contour(time,depth,salt_ratio,w)
set(gca,'YDir','reverse','YLim',[0 Lt])
xlabel('Time (years)')
ylabel('Depth (mbsf)')
title('Salt advection ratio')
colorbar
figure
contourf(time,depth,sh_evolution)
set(gca,'YDir','reverse','YLim',[0 Lt])
xlabel('Time (years)')
```

```
ylabel('Depth (mbsf)')
title('Hydrate saturation')
colorbar
```

Appendix E: MATLAB code used for Chapter 6

This code is similar to the code used for Chapter 4 in that it utilizes a constant

flux basal boundary and solves for hydrate saturation using an explicit, forward in time,

centered in space (FTCS) scheme (Fletcher, 1997). Methane solubility is computed using

the same subroutines as in Appendix C. The three-phase equilibrium temperature is

updated for changes in pore radius due to hydrate formation using Equation 6.1. Two

versions of code are presented: the version used to model Hydrate Ridge, and the version

used to model Northern Cascadia.

```matlab
clear all
dz = 0.05;
dt = 0.01; %in years
maxiter = 1000000;
depth = [0:dz:4.95];
base = 100; %bottom of domain (mbsf)
T0 = 277; %seafloor temp (K)
d0 = 800; %seafloor depth (m)
G = 0.053; %geothermal gradient (K/m)
qf = 430; %flow rate (mm/yr)
mNa = 0.593; % inital salt concentration (molality)
silt_d50 = 3e-5;    %silt grain diameter (m)
clay_d50 = 5e-7;    %clay grain diameter (m)
silt_perm = 0.00068*(silt_d50^2); %silt permeability (m2)
clay_perm = 0.00068*(clay_d50^2);  %clay permeability (m2)
silt_por = 0.55; %silt porosity
clay_por = 0.52; %clay porosity
pr_silt = 0.4; % Poisson's ratio for silt
pr_clay = 0.4; % Poisson's ratio for clay
perm=zeros(1,length(depth));
por=zeros(1,length(depth));
perm(1:30)=clay_perm;
perm(31:35)=silt_perm;
perm(36:65)=clay_perm;
perm(66:70)=silt_perm;
perm(71:100)=clay_perm;
por(1:30)=clay_por;
por(31:35)=silt_por;
por(36:65)=clay_por;
por(66:70)=silt_por;
por(71:100)=clay_por;
frac_crit(1:30)=pr_clay/(1-pr_clay);
```

```
frac_crit(31:35)=pr_silt/(1-pr_silt);
frac_crit(36:65)=pr_clay/(1-pr_clay);
frac_crit(66:70)=pr_silt/(1-pr_silt);
frac_crit(71:100)=pr_clay/(1-pr_clay);
grain_rad(1:30)=clay_d50/2;
grain_rad(31:35)=silt_d50/2;
grain_rad(36:65)=clay_d50/2;
grain_rad(66:70)=silt_d50/2;
grain_rad(71:100)=clay_d50/2;
chlorides = (mNa*0.05844247)/(1+(mNa*0.05844247));
% global parameters
rhow = 1024;
rhos = 2700;
g = 9.80665;
muw = 0.000887;
rhoh = 930;
cmh = 0.134;
% make temperature and pressure vectors
T = T0 + ((base-depth).*G); %in K
for i=1:length(depth)
    p_star_inc(i)=((qf*muw*dz)/(perm(i)))*(0.001/(24*365*3600));
end
p_star=fliplr(cumsum(fliplr(p_star_inc)))+(((qf*muw*3.170979e-11)/1e-
14)*((base-max(depth))-dz));
P = (((base-depth)+d0).*rhow*g*1e-6)+(p_star.*1e-6); %in MPa
P0 = d0*rhow*g*1e-6;
% compute triple point curve and find solubility
T3P_inf = 1./(-3.6505e-6.*(log(P)).^3+3.704e-5.*(log(P)).^2 -
0.00021948.*log(P) + 0.0038494);
%T3P_cap = T3P_inf-(T3P_inf.*(0.0016+(2.3e-
10.*((por./(32.*perm)).^0.5))));
T3P_cap = T3P_inf+(T3P_inf.*((-
2.*0.027)./(grain_rad.*rhow.*54500.*0.414213562)));
T = T3P_inf;
liquid_vapor_solubility;
cm_eq_inf=sol.*exp((T-T3P_inf)./15.3);
clear T
T = T3P_cap;
liquid_vapor_solubility;
cm_eq_cap=sol.*exp((T-T3P_cap)./15.3);
clear T
T = T0 + ((base-depth).*G);
cml_base = cm_eq_cap(1)-(cm_eq_cap(30)-cm_eq_cap(31));
%cml_base = cm_eq_cap(1);
cml=zeros(1,length(depth));
cml_new=zeros(1,length(depth));
Sh=zeros(1,length(depth));
Sh_new=zeros(1,length(depth));
frac_flag=zeros(1,length(depth));
iter=0;
while iter<maxiter
    cml_new(1)=((1-
((qf*dt*0.001)/(dz*por(1))))*cml(1))+(cml_base*((qf*dt*0.001)/(dz*por(1
)))));
    for i=2:length(depth)
        cml_new(i)=((1-((qf*dt*0.001)/(dz*por(i))))*cml(i))+(cml(i-
1)*((qf*dt*0.001)/(dz*por(i)))));
```

```matlab
    end
    for i=1:length(depth)
        if cml_new(i)==cm_eq_cap(i)
            if i==1
                Sh_new(i)=Sh(i)+((dt/dz)*((qf*0.001*rhow*(cml_new(i)-
cml_base))/(por(i)*((rhoh*cmh)-(rhow*cml_new(i))))));
            else
                Sh_new(i)=Sh(i)+((dt/dz)*((qf*0.001*rhow*(cml_new(i)-
cml_new(i-1)))/(por(i)*((rhoh*cmh)-(rhow*cml_new(i))))));
            end
        elseif cml_new(i)>cm_eq_cap(i)
            Sh_new(i)=Sh(i)+((cml_new(i)-cm_eq_cap(i))*((rhow*(1-
Sh(i)))/((rhoh*cmh)-(rhow*cm_eq_cap(i)))));
            cml_new(i)=cm_eq_cap(i);
        else
            Sh_new(i)=Sh(i);
        end
    end
    for i=1:length(depth)
        if frac_flag(i)<1
            Sh_new(i)=Sh_new(i);
        else
            Sh_new(i)=Sh(i);
        end
    end
    for i=1:length(depth)
        sigv_eff_inc(i)=((rhos*(1-por(i)))+(rhow*((por(i)*(1-
Sh_new(i)))-1))+(rhoh*por(i)*Sh_new(i)))*g*dz;
        if frac_flag(i)<1
            p_star_inc(i)=((qf*muw*dz)/(perm(i)*((1-
Sh_new(i))^4)))*(0.001/(24*365*3600));
        else
            p_star_inc(i)=((qf*muw*dz)/(8.333e-11*((1-
(por(i)*Sh_new(i))/0.001)^3)))*(0.001/(24*365*3600));
        end
    end
    sigv_eff=(fliplr(cumsum(fliplr(sigv_eff_inc))))+(((base-
max(depth))-dz)*g*((0.4*rhos)-(0.4*rhow)));
    p_star=fliplr(cumsum(fliplr(p_star_inc)))+(((qf*muw*3.170979e-
11)/1e-14)*((base-max(depth))-dz));
    lambda_star=p_star./sigv_eff;
    for i=1:length(depth)
        if lambda_star(i)>=frac_crit(i)
            frac_flag(i)=1;
        end
    end
    %T3P_cap = T3P_inf-(T3P_inf.*(0.0016+(2.3e-
10.*((por./(32.*perm.*((1-Sh_new).^2)).^0.5)))));
    T3P_cap = T3P_inf+(T3P_inf.*((-2.*0.027)./(grain_rad.*((1-
Sh_new).^(1/3)).*rhow.*54500.*0.414213562)));
    clear T
    T = T3P_cap;
    P = (((base-depth)+d0).*rhow*g*1e-6)+(p_star.*1e-6);
    liquid_vapor_solubility;
    for i=1:length(depth)
        if frac_flag(i)>0
            cm_eq_cap(i)=cm_eq_inf(i);
```

```
            else
                cm_eq_cap(i)=sol(i)*exp((T(i)-T3P_cap(i))/15.3);
            end
        end
        clear T
        T = T0 + ((base-depth).*G);
        %if max(frac_flag)==1
        %    break
        %end
        if iter>0
            if rem(iter,1000)==0
                sh_evolution(:,iter*0.001)=Sh_new;
                cm_evolution(:,iter*0.001)=cm_eq_cap;
                l_star_evolution(:,iter*0.001)=lambda_star;
            end
        end
        Sh=Sh_new;
        cml=cml_new;
        iter=iter+1;
end
time=[1000*dt:1000*dt:(iter-1)*dt];
figure
subplot(1,3,1)
plot(Sh,depth)
xlabel('Sh')
ylabel('Depth (m)')
subplot(1,3,2)
plot(cm_eq_inf,depth,cm_eq_cap,depth)
xlabel('Concentration (kg/kg)')
legend('Bulk water','Pores')
subplot(1,3,3)
plot(lambda_star,depth,frac_crit,depth,frac_flag,depth)
xlabel('L*')
figure
contourf(time,depth,sh_evolution)
xlabel('Time (years)')
ylabel('Depth (mbsf)')
title('Hydrate saturation')
colorbar
figure
contourf(time,depth,cm_evolution)
xlabel('Time (years)')
ylabel('Depth (mbsf)')
title('Solubility')
colorbar




clear all
dz = 0.01;
dt = 0.1; %in years
maxiter = 2000000;
depth = [0:dz:7.59];
base = 200; %bottom of domain (mbsf)
T0 = 276; %seafloor temp (K)
```

```
d0 = 2185; %seafloor depth (m)
G = 0.06; %geothermal gradient (K/m)
qf = 1; %flow rate (mm/yr)
mNa = 0.593; % inital salt concentration (molality)
silt_d50 = 8e-5;      %silt grain diameter (m)
clay_d50 = 1.6e-5;      %clay grain diameter (m)
silt_perm = 0.00068*(silt_d50^2); %silt permeability (m2)
clay_perm = 0.00068*(clay_d50^2);  %clay permeability (m2)
silt_por = 0.35; %silt porosity
clay_por = 0.6; %clay porosity
pr_silt = 0.4; % Poisson's ratio for silt
pr_clay = 0.4; % Poisson's ratio for clay
perm=zeros(1,length(depth));
por=zeros(1,length(depth));
perm(1:250)=clay_perm;
perm(251:255)=silt_perm;
perm(256:505)=clay_perm;
perm(506:510)=silt_perm;
perm(511:760)=clay_perm;
por(1:250)=clay_por;
por(251:255)=silt_por;
por(256:505)=clay_por;
por(506:510)=silt_por;
por(511:760)=clay_por;
frac_crit(1:250)=pr_clay/(1-pr_clay);
frac_crit(251:255)=pr_silt/(1-pr_silt);
frac_crit(256:505)=pr_clay/(1-pr_clay);
frac_crit(506:510)=pr_silt/(1-pr_silt);
frac_crit(511:760)=pr_clay/(1-pr_clay);
grain_rad(1:250)=clay_d50/2;
grain_rad(251:255)=silt_d50/2;
grain_rad(256:505)=clay_d50/2;
grain_rad(506:510)=silt_d50/2;
grain_rad(511:760)=clay_d50/2;
chlorides = (mNa*0.05844247)/(1+(mNa*0.05844247));
% global parameters
rhow = 1024;
rhos = 2700;
g = 9.80665;
muw = 0.000887;
rhoh = 930;
cmh = 0.134;
% make temperature and pressure vectors
T = T0 + ((base-depth).*G); %in K
for i=1:length(depth)
    p_star_inc(i)=((qf*muw*dz)/(perm(i)))*(0.001/(24*365*3600));
end
p_star=fliplr(cumsum(fliplr(p_star_inc)))+(((qf*muw*3.170979e-11)/1e-
14)*((base-max(depth))-dz));
P = (((base-depth)+d0).*rhow*g*1e-6)+(p_star.*1e-6); %in MPa
P0 = d0*rhow*g*1e-6;
% compute triple point curve and find solubility
T3P_inf = 1./(-3.6505e-6.*(log(P)).^3+3.704e-5.*(log(P)).^2 -
0.00021948.*log(P) + 0.0038494);
%T3P_cap = T3P_inf-(T3P_inf.*(0.0016+(2.3e-
10.*((por./(32.*perm)).^0.5))));
```

```matlab
T3P_cap = T3P_inf+(T3P_inf.*((-
2.*0.027)./(grain_rad.*rhow.*54500.*0.414213562)));
T = T3P_inf;
liquid_vapor_solubility;
cm_eq_inf=sol.*exp((T-T3P_inf)./15.3);
clear T
T = T3P_cap;
liquid_vapor_solubility;
cm_eq_cap=sol.*exp((T-T3P_cap)./15.3);
clear T
T = T0 + ((base-depth).*G);
cml_base = cm_eq_cap(1)-(cm_eq_cap(250)-cm_eq_cap(251));
%cml_base = cm_eq_cap(1);
cml=zeros(1,length(depth));
cml_new=zeros(1,length(depth));
Sh=zeros(1,length(depth));
Sh_new=zeros(1,length(depth));
frac_flag=zeros(1,length(depth));
iter=0;
while iter<maxiter
    cml_new(1)=((1-
((qf*dt*0.001)/(dz*por(1))))*cml(1))+(cml_base*((qf*dt*0.001)/(dz*por(1
)))));
    for i=2:length(depth)
        cml_new(i)=((1-((qf*dt*0.001)/(dz*por(i))))*cml(i))+(cml(i-
1)*((qf*dt*0.001)/(dz*por(i)))));
    end
    for i=1:length(depth)
        if cml_new(i)==cm_eq_cap(i)
            if i==1
                Sh_new(i)=Sh(i)+((dt/dz)*((qf*0.001*rhow*(cml_new(i)-
cml_base))/(por(i)*((rhoh*cmh)-(rhow*cml_new(i))))));
            else
                Sh_new(i)=Sh(i)+((dt/dz)*((qf*0.001*rhow*(cml_new(i)-
cml_new(i-1)))/(por(i)*((rhoh*cmh)-(rhow*cml_new(i))))));
            end
        elseif cml_new(i)>cm_eq_cap(i)
            Sh_new(i)=Sh(i)+((cml_new(i)-cm_eq_cap(i))*((rhow*(1-
Sh(i)))/((rhoh*cmh)-(rhow*cm_eq_cap(i)))));
            cml_new(i)=cm_eq_cap(i);
        else
            Sh_new(i)=Sh(i);
        end
    end
    for i=1:length(depth)
        if frac_flag(i)<1
            Sh_new(i)=Sh_new(i);
        else
            Sh_new(i)=Sh(i);
        end
    end
    for i=1:length(depth)
        sigv_eff_inc(i)=((rhos*(1-por(i)))+(rhow*((por(i)*(1-
Sh_new(i)))-1))+(rhoh*por(i)*Sh_new(i)))*g*dz;
        if frac_flag(i)<1
            p_star_inc(i)=((qf*muw*dz)/(perm(i)*((1-
Sh_new(i))^4)))*(0.001/(24*365*3600));
```

```matlab
            else
                p_star_inc(i)=((qf*muw*dz)/(8.333e-11*((1-
(por(i)*Sh_new(i))/0.001)^3)))*(0.001/(24*365*3600));
            end
        end
        sigv_eff=(fliplr(cumsum(fliplr(sigv_eff_inc))))+(((base-
max(depth))-dz)*g*((0.4*rhos)-(0.4*rhow)));
        p_star=fliplr(cumsum(fliplr(p_star_inc)))+(((qf*muw*3.170979e-
11)/1e-14)*((base-max(depth))-dz));
        lambda_star=p_star./sigv_eff;
        for i=1:length(depth)
            if lambda_star(i)>=frac_crit(i)
                frac_flag(i)=1;
            end
        end
        %T3P_cap = T3P_inf-(T3P_inf.*(0.0016+(2.3e-
10.*((por./(32.*perm.*((1-Sh_new).^2)).^0.5)))));
        T3P_cap = T3P_inf+(T3P_inf.*((-2.*0.027)./(grain_rad.*((1-
Sh_new).^(1/3)).*rhow.*54500.*0.414213562)));
        clear T
        T = T3P_cap;
        P = (((base-depth)+d0).*rhow*g*1e-6)+(p_star.*1e-6);
        liquid_vapor_solubility;
        for i=1:length(depth)
            if frac_flag(i)>0
                cm_eq_cap(i)=cm_eq_inf(i);
            else
                cm_eq_cap(i)=sol(i)*exp((T(i)-T3P_cap(i))/15.3);
            end
        end
        clear T
        T = T0 + ((base-depth).*G);
        %if max(frac_flag)==1
        %    break
        %end
        if iter>0
            if rem(iter,1000)==0
                sh_evolution(:,iter*0.001)=Sh_new;
                cm_evolution(:,iter*0.001)=cm_eq_cap;
                l_star_evolution(:,iter*0.001)=lambda_star;
            end
        end
        Sh=Sh_new;
        cml=cml_new;
        iter=iter+1;
end
time=[1000*dt:1000*dt:(iter-1)*dt];
figure
subplot(1,3,1)
plot(Sh,depth)
xlabel('Sh')
ylabel('Depth (m)')
subplot(1,3,2)
plot(cm_eq_inf,depth,cm_eq_cap,depth)
xlabel('Concentration (kg/kg)')
legend('Bulk water','Pores')
subplot(1,3,3)
```

```
plot(lambda_star,depth,frac_crit,depth,frac_flag,depth)
xlabel('L*')
figure
contourf(time,depth,sh_evolution)
xlabel('Time (years)')
ylabel('Depth (mbsf)')
title('Hydrate saturation')
colorbar
figure
contourf(time,depth,cm_evolution)
xlabel('Time (years)')
ylabel('Depth (mbsf)')
title('Solubility')
colorbar
```

Appendix F: Derivation of criterion for cessation of hydrate formation

The time t_λ required to reach the critical overpressure ratio λ^*_c can be approximated as (see Appendix B)

$$t_\lambda = \frac{\lambda^*_c - \lambda^*_0}{\dfrac{\partial \lambda^*}{\partial t}},$$ (Equation F1)

where λ^*_0 is the initial overpressure ratio. Similarly, considering only advective transport of methane, the time t_s required to reach the critical solubility at which hydrate formation will cease is

$$t_s = \frac{x^l_{m,c} - x^l_{m,0}}{\dfrac{\partial x^l_m}{\partial t}},$$ (Equation F2)

where $x^l_{m,0}$ and $x^l_{m,c}$ are the initial solubility and critical solubility to stop hydrate formation (i.e., the dissolved methane concentration in the pore fluid). The ratio of t_λ and t_s is

$$\frac{t_\lambda}{t_s} = \frac{\left(\lambda_c^* - \lambda_0^*\right)\frac{\partial x_m^l}{\partial t}}{\left(x_{m,c}^l - x_{m,0}^l\right)\frac{\partial \lambda^*}{\partial t}} = \frac{\left(\lambda_c^* - \lambda_0^*\right)\frac{\partial x_m^l}{\partial S_h}\frac{\partial S_h}{\partial t}}{\left(x_{m,c}^l - x_{m,0}^l\right)\frac{\partial \lambda^*}{\partial S_h}\frac{\partial S_h}{\partial t}} = \frac{\left(\lambda_c^* - \lambda_0^*\right)\frac{\partial x_m^l}{\partial S_h}}{\left(x_{m,c}^l - x_{m,0}^l\right)\frac{\partial \lambda^*}{\partial S_h}},$$
(Equation F3)

and utilizing the relation $\partial\lambda^*/\partial S_h \approx 2\lambda^*$ (see Appendix B),

$$\frac{t_\lambda}{t_s} = \frac{\left(\lambda_c^* - \lambda_0^*\right)\frac{\partial x_m^l}{\partial S_h}}{2\lambda_0^*\left(x_{m,c}^l - x_{m,0}^l\right)}.$$
(Equation F4)

For fractures to form prior to cessation of hydrate formation, $t_\lambda/t_s < 1$, providing a condition on $\partial x_m^l/\partial S_h$:

$$\frac{\partial x_m^l}{\partial S_h} < \frac{2\lambda_0^*\left(x_{m,c}^l - x_{m,0}^l\right)}{\lambda_c^* - \lambda_0^*}.$$
(Equation F5)

The λ_0^* in Equation F5 can be eliminated by combining Equations 6.11 and 6.12 in the limit where $S_h = 0$ (i.e. the initial conditions for hydrate systems):

$$\frac{\partial x_m^l}{\partial S_h} < \frac{2\left|\vec{q}_f\right|\mu_w\left(\frac{1}{k_s} + \frac{1}{k_c}\right)\left(x_{m,c}^l - x_{m,0}^l\right)}{\lambda_c^*\left(g\left(\rho_g + \rho_w\right)\right) - \left|\vec{q}_f\right|\mu_w\left(\frac{1}{k_s} + \frac{1}{k_c}\right)}.$$
(Equation F6)

Rearranging Equation F6 results in Equation 6.15.